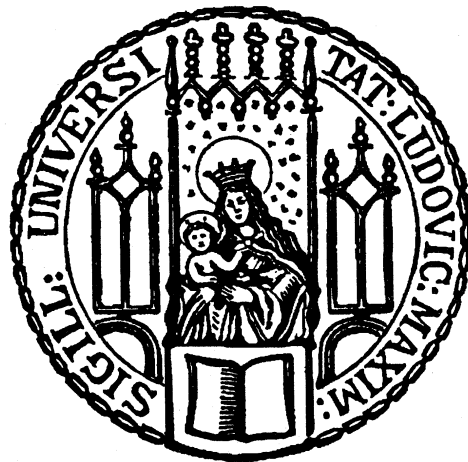# Quantum Gas Microscopy of Fermi-Hubbard Ladders

Sarah Hirthe

München 2022

Quantum Gas Microscopy of Fermi-Hubbard Ladders

Dissertation
an der Fakultät für Physik
der Ludwig-Maximilians-Universität
München

vorgelegt von

Sarah Hirthe

aus Biberach a. d. Riß

München, den 19.12.2022

Erstgutachter:
Prof. Immanuel Bloch

Zweitgutachter:
Prof. Christian Groß

Tag der mündlichen Prüfung:
10. Februar 2023

Zusammenfassung

Stark wechselwirkende Systeme sind eine der Hauptherausforderungen der modernen Physik. Ihre intrinsische Komplexität verhindert eine effiziente Simulation mit klassischen Computern. Ein Beispiel für solche Systeme sind antiferromagnetische Mottisolatoren, in denen ein Wettstreit zwischen Spin- und Ladungsfreiheitsgraden zu exotischen Phänomenen wie Ladungsträgerpaarung und Supraleitung führt. Das Fermi-Hubbard-Modell, welches das Verhalten stark wechselwirkender Fermionen auf einer Gitterstruktur beschreibt, ist ein Minimalmodell welches die Physik dieser stark korrelierten Materialien wiedergibt.

In dieser Doktorarbeit benutzen wir einen Quantensimulator basierend auf ultrakalten Atomen in optischen Gittern, um Simulationen des Fermi-Hubbard-Modells durchzuführen. Wir realisieren den stark wechselwirkenden Bereich dieses Modells in einer Leitergeometrie bestehend aus zwei gekoppelten Ketten. Wir messen lokale und nichtlokale Spin- und Ladungskorrelationen indem wir die Spin und Dichteauflösung einzelner Gitterplätze unseres Quantengasmikroskops nutzen. Wir untersuchen das System bei Temperaturen auf der Größenordnung der Spinaustauschwechselwirkung, welche aufgrund des Zusammenspiels von magnetischer und kinetischer Energie das Einsetzen exotischer Quantenvielteilchenphänomene markiert.

In dotierten Leitersystemen beobachten wir direkt die Paarung von Dotanden, ein Prozess der der Hochtemperatursupraleitung zu Grunde liegt. Wir stellen fest, dass die Paarung stark gesteigert wird, wenn die Bewegungsfreiheit der Dotanden in eine Richtung unterdrückt wird, während Spinaustausch in alle Richtungen stattfindet. Mit einer solchen Geometrie erreichen wir Bindungsenergien die vergleichbar mit der Spinaustauschwechselwirkung sind. Im Gegensatz dazu ist Pauliabstossung dominant gegenüber der Paarbindung, wenn Bewegung in alle Richtungen ermöglicht wird. Wir untersuchen außerdem die Auswirkung der Paare auf den Magnetismus im System und bestätigen deren Zusammenhang. Bei höherer Dotierung stellen wir eine Korrelation zwischen verschiedenen Paaren fest, welche konsistent ist mit Ladungsdichteordnung.

Ein weiteres Ergebnis dieser Arbeit ist die Realisierung einer Variante der symmetriegeschützten topologischen Haldane Phase bei endlicher Systemgrösse und endlicher Temperatur. Wir beobachten die Signaturen dieser paradigmatischen Quantenphase, indem wir das experimentelle Leitersystem auf eine antiferromagnetische Spin-1 Kette abbilden. Wir nutzen die einzigartigen Möglichkeiten unseres Experiments um nichtlokale Stringordnungsparameter zu messen, welche uns die Unterscheidung zwischen topologischer und trivialer Phase ermöglichen. Wir untersuchen außerdem die Robustheit der Phase bezüglich verschiedener Kopplungsparameter und Systemgrößen. Schließlich charakterisieren wir die Randmoden des Systems.

Abstract

Understanding the behavior of strongly interacting quantum systems remains a central challenge in modern physics. The intrinsic complexity of these correlated systems has prevented efficient simulation on classical computers. Antiferromagnetic Mott insulators are an example in which competing processes of the spin and charge degrees of freedom lead to exotic phenomena like charge carrier pairing and superconductivity. The Fermi-Hubbard model, which describes the behavior of interacting fermions on a lattice, is a minimal model that captures the essential physics of strongly correlated materials.

In this thesis, we use a quantum simulator based on ultracold atoms in optical lattices to perform simulations of the Fermi-Hubbard model. We realize the strongly interacting regime of this model in a ladder geometry consisting of two coupled chains. Harnessing the single-site spin and density resolution of our quantum gas microscope, we measure local and nonlocal spin and density correlations. We probe the system at temperatures around the spin-exchange energy, which marks the onset of exotic quantum many-body phenomena due to the interplay of magnetic and kinetic energy.

In doped ladder systems, we directly observe the pairing of dopants, a process that is at the heart of high-temperature superconductivity. We find that pairing is strongly enhanced by suppressing one direction of dopant motion, while spin exchange persists in all directions. With such a geometry, we reach binding energies on the order of the spin-exchange energy. In contrast, if dopant movement is enabled in all directions, Pauli repulsion becomes dominant over binding. We furthermore investigate the effect of the pairs on magnetism and confirm their strong connection. At higher doping, we find correlations between pairs of dopants that are consistent with charge density order.

Another result of this thesis is the realization of a finite-size and finite-temperature version of the symmetry-protected topological Haldane phase. We observe the signatures of this paradigmatic quantum phase of matter by mapping the experimental ladder system onto an antiferromagnetic spin-1 chain. We use the unique ability of our experiment to measure non-local string order parameters which allow us to distinguish between the topological and the trivial phase. We furthermore investigate the robustness of the phase for different parameter regimes and system sizes. Finally, we characterize the edge modes of the system.

Contents

Introduction

The emergence of material properties from their microscopic constituents still poses many questions despite decades of research. While the equations governing single quantum particles are well understood and can often be solved exactly, such solutions remain elusive for most quantum many-body systems [1, 2]. Furthermore, the presence of strong interactions between particles complicates numerical computation. The exorbitant size of the Hilbert space, exponential in the number of particles, lies beyond the capabilities of any classical computer.

Nevertheless, effective models and the development of numerical tools [3–5], as well as a constant experimental progress [6], contribute to an ever-increasing knowledge regarding strongly correlated electronic systems, topological quantum matter, atomic and molecular physics, and many others.

In order to simulate such quantum many-body systems, Richard Feynman famously proposed the use of a 'quantum simulator' [7], a machine whose constituents are based on quantum mechanics, thereby imitating the very physics it simulates. In the last 20 years quantum simulation has indeed emerged as a promising tool to tackle a wide range of quantum many-body problems [8, 9]. In contrast to universal quantum computers, whose application is still out-of-reach for most tasks, particular quantum systems are carefully engineered to imitate the behavior of the target system. Prominent platforms to perform such simulations are for example trapped ions [10–12], ultracold atoms [13], quantum dots [14, 15] and superconducting circuits [16, 17].

Ultracold atoms in particular have shown to be a versatile tool for quantum simulation [18, 19]. They are capable of tackling a large area of quantum problems for both bosonic and fermionic systems, that range from continuous systems in one [20], two [21, 22] and three dimensions [23] to lattice models [19]. The simulated systems can have sizes from few particle physics [24] to ensembles of many millions [25] and can often be tuned from the non-interacting regime all the way to unitary gases [26, 27].

The field of ultracold atoms was enabled by technological advances in laser cooling and trapping [28] and evaporative cooling techniques [29–31]. These developments lead to the breakthroughs of observing Bose-Einstein condensation (BEC) [29, 30] and the BEC-to-BCS crossover in fermionic superfluids [32].

The implementation of optical lattices [33], i.e. periodic dipole traps of interfering laser beams, has allowed for the realization of lattice models like the Bose- and Fermi-Hubbard model [34, 35]. These models play an instrumental role in condensed matter physics. Optical lattices have allowed for the observation of the superfluid-to-Mott-insulator transition [36, 37], many-body localization [38] and the realization of

topological models like the Haldane model [39] and the Hofstadter Hamiltonian [40]. Further technological advancements like the implementation of high-resolution objectives and improved cooling schemes have allowed for the development of quantum gas microscopy using fluorescence imaging of bosons in optical lattices [41, 42] and fermions in optical lattices [43–46]. With their single-site resolution, these microscopes have enabled access to a multitude of so-far-inaccessible microscopic observables like local spin- and density correlations [47–50]. The approach is closely related to single atoms in optical tweezers [51–53], a platform currently en route to fully programmable quantum computation [54].

By now there exist a multitude of both bosonic and fermionic microscopes, some of which have developed further techniques like spin resolution [47], or bilayer imaging techniques [55–57] and site-resolved addressing and potential shaping schemes [58, 59]. In this thesis, a fermionic quantum gas microscope is used to explore different aspects of the Fermi-Hubbard model. In particular ladder-shaped system geometries, that is lattices consisting of two rungs and L legs, are employed to study charge-carrier pairing, an intensely researched phenomenon of strongly correlated electronic systems, as well as the Haldane phase, a paradigmatic symmetry-protected topological phase.

The origin of unconventional superconductivity

An outstanding quantum many-body problem is the origin of unconventional superconductivity [60, 61]. Superconductors are materials that transmit current without any resistivity below a certain critical temperature. In particular high-temperature (high-T_C) superconductivity can persist up to $133\,\mathrm{K}$ [62, 63]. In order for a material to become superconducting, the fermionic charge carriers need to form pairs. These bound objects follow bosonic statistics and can condense into a superfluid, a (quantum) state of matter that flows without viscosity. While for conventional superconductors the phonon-mediated pairing process is explained by the BCS theory [64], the origin of charge carrier pairing in unconventional superconductors is still a matter of debate. One prominent view is to attribute the pairing mechanism to magnetic fluctuations [65, 66]. This idea of magnetically mediated pairing is supported by the phase diagrams of unconventional superconductors, as they tend to feature magnetically ordered phases in the vicinity of the superconducting phase. Examples include heavy fermion systems [67], iron pnictides [68], layered organic materials of the BEDT family [69], cuprate superconductors [70–72], and twisted bilayer graphene [73, 74]. The last three classes of materials are particularly striking since they exhibit superconductivity emerging upon doping antiferromagnetic Mott insulators. To simulate the physics of doped antiferromagnets, cold atom systems can realize the Fermi-Hubbard model, which is considered to be a minimal model for the cuprate high-T_C superconductors [75]. However, due to its complexity and challenges like the Fermi sign problem in numerical investigations [76], the existence of pairing and superconductivity in the Hubbard model is still a topic of debate [77–80]. In order to shed light on pairing in Fermi-Hubbard systems, several theoretical studies considered doped Hubbard ladders and $t - J$ ladders [81–85]. Ladder systems consist of two coupled

chains and are thus less complex than two-dimensional systems. An important consequence is, that accurate numerical solutions can be obtained using the density matrix renormalization group (DMRG) algorithm [86]. Ladder materials are also known to display superconductivity from several solid-state experiments [87–89]. Ladders thus pose an ideal model to experimentally demonstrate pairing in a well-understood setting and experimentally confirm the possibility of a magnetically mediated pairing process. The observations presented in this thesis constitute the first microscopic observation of pairing in a quantum simulator.

Simulating symmetry-protected topological phases

Apart from superconductivity, Hubbard ladders host a myriad of other phenomena that arise from the antiferromagnetic Mott insulating regime. Symmetry-protected topological phases are one of them and their appearance in form of the Haldane phase has been studied in the course of this thesis. Since the description of topological phase transitions by J. Michael Kosterlitz and David J. Thouless 50 years ago [90], topology has fundamentally changed our understanding of quantum phases of matter. The Landau theory [91] distinguishes different phases based on symmetry breaking and corresponding local order parameters. Topological phase transitions, however, are not captured by this approach, but can instead be characterized through topological properties and non-local topological order parameters [92, 93]. Topological invariants serve to distinguish different quantum phases of matter. A prominent example is the Chern number [94], capturing the winding of eigenstates. While so-called topological phases display long-range entangled topological order, another class called symmetry-protected topological (SPT) phases are short-range entangled [95, 96]. Examples of topological phases include quantum Hall systems [97] and the Kitaev honeycomb model [98], while the archetype of SPT phases is the Haldane phase [99, 100]. This strongly interacting model describes the ground state of an antiferromagnetic spin-1 chain. A hallmark feature of such topologically nontrivial systems is the bulk-edge correspondence [93, 95], describing the relationship between the degenerate edge states and the bulk properties protecting them. In the Haldane phase, the bulk is characterized by a non-local order parameter, while the edge hosts fourfold degenerate edge states due to fractional spin degrees of freedom. In this thesis, an effective spin-1 chain is built up of spin-1/2 particles in Hubbard ladders in order to realize the Haldane phase. Even though the spin-1/2 system does not map on a short-range system, it can be shown that the two systems are adiabatically connected and thus exhibit the same phase [101].

Outline of the thesis

In this thesis, Fermi-Hubbard ladders are engineered using a Fermi-gas microscope with single-site potential shaping. The tunability of interactions, lattice potential, and atom number allows for the realization of the strongly interacting Heisenberg regime, as well as doped t-J ladders. Harnessing the full spin and density resolution of our system, we can extract local and non-local correlations within and between the spin

and charge sectors of the system. This enables us to observe hole pairing mediated by magnetic correlations, a process that is thought to be behind the charge-carrier pairing in unconventional superconductors. In a second project, we study the physics of the symmetry-protected topological Haldane phase using ladders with a special edge termination. We observe the characteristic non-local string order and corresponding edge states and compare them to a similar system in the topologically trivial phase.

- In Ch. 2 the Fermi-Hubbard model is introduced as an important theoretical model to study condensed matter physics and the key aspects of simulating this model in a cold atom quantum simulator are laid out. Fermi-Hubbard ladders are introduced as a useful minimal system to study the behavior of the doped Fermi-Hubbard model, and as a system that can realize the Haldane phase.

- In the following, in Ch. 3, the experimental apparatus is introduced. A special focus lies on the imaging and potential shaping of the system and on recent technical improvements.

- Ch. 4 presents the main results of this thesis. Dopant pairing, mediated by the magnetic correlations in the system, is observed in ladder systems through the evaluation of two-point density correlations. To achieve this, dopant repulsion is switched off between the legs of the ladder using an especially tailored potential offset.

- In Ch. 5 we present a finite-size and finite-temperature version of the Haldane phase. In an undoped ladder with a special tilted edge termination, we define diagonal unit cells and show that the system of these unit cells displays the characteristic signatures of the Haldane phase.

Publications

The following papers were published in the course of this PhD thesis.

- Magnetically mediated hole pairing in fermionic ladders of ultracold atoms
  S. Hirthe, T. Chalopin, D. Bourgund, P. Bojović, A. Bohrdt, E. Demler, F. Grusdt,
  I. Bloch and T. A. Hilker.
  Nature 613, 463–467 (2023).

- Realizing the symmetry-protected Haldane phase in Fermi–Hubbard ladders.
  P. Sompet*, S. Hirthe*, D. Bourgund*, T. Chalopin, J. Bibo, J. Koepsell, P. Bojović,
  R. Verresen, F. Pollmann, G. Salomon, C. Gross, T. A. Hilker and I. Bloch.
  Nature 606, 484–488 (2022).
  Equal contributions

- Microscopic evolution of doped Mott insulators from polaronic metal to Fermi
  liquid.
  J. Koepsell, D. Bourgund, P. Sompet, S. Hirthe, A. Bohrdt, Y. Wang, F. Grusdt, E.
  Demler, G. Salomon, C. Gross and I. Bloch.
  Science 374, 6563 (2021).

- Robust bilayer charge pumping for spin- and density-resolved quantum gas microscopy.
  J. Koepsell, S. Hirthe, D. Bourgund, P. Sompet, J. Vijayan, G. Salomon, C. Gross
  and I. Bloch.
  Physical Review Letters 125, 010403 (2020).

- Time-resolved observation of spin-charge deconfinement in fermionic Hubbard
  chains.
  J. Vijayan*, P. Sompet*, G. Salomon, J. Koepsell, S.Hirthe, A. Bohrdt, F. Grusdt,
  I. Bloch and C. Gross.
  Science 367, 6474 (2020).
  Equal contributions

The Fermi-Hubbard model - theory and quantum simulation

This chapter discusses the Fermi-Hubbard model and its simulation using cold atoms in optical lattices. Different aspects and phases of the Fermi-Hubbard model are explained alongside experimental realizations. A special focus lies on the effects of doping. Furthermore, this chapter introduces the specific properties of Fermi-Hubbard ladders and gives the theoretical background for dopant pairing in these ladders. Finally, symmetry-protected topological phases and the appearance of the Haldane phase in ladder systems are introduced.

2.1   A model to study strongly correlated electrons

Electronic systems are one of the cornerstones of our technological age, but the underlying quantum many-body processes are often subject to intense research with many open questions remaining. One of the main models to describe strongly correlated electrons in condensed matter physics is the Fermi-Hubbard model, consisting of repulsively interacting spin-1/2 particles living on a periodic lattice structure [102, 103]. This model displays a wide range of phenomena observed in materials with strong electron correlations and is thought to be a minimal model that captures the essential physics of high-T_C superconductivity. Despite the relatively simple structure of the model, its simulation on classical computers poses a major challenge. Even with considerable theoretical effort, no consensus about the very existence of superconductivity in this model has been reached [77, 104, 105]. Efficient exact diagonalization codes on modern supercomputers can handle about 16 sites for the full Fermi-Hubbard model [106], while DMRG [86] works reliably for cylinders of few legs and considerable length, e.g. 24x4 in [77]. Other theoretical methods include auxiliary-field quantum Monte Carlo [77], worm-algorithm Monte Carlo [107], approached based on the self-consistent Born approximation [108], and many others. Further descriptions to capture superconducting materials in different regimes include the RVB approach [75], nearly antiferromagnetic Fermi liquid theory [109], DMFT and its extensions [110], while other effective models more directly target the Fermi-Hubbard model, like strings [111, 112].
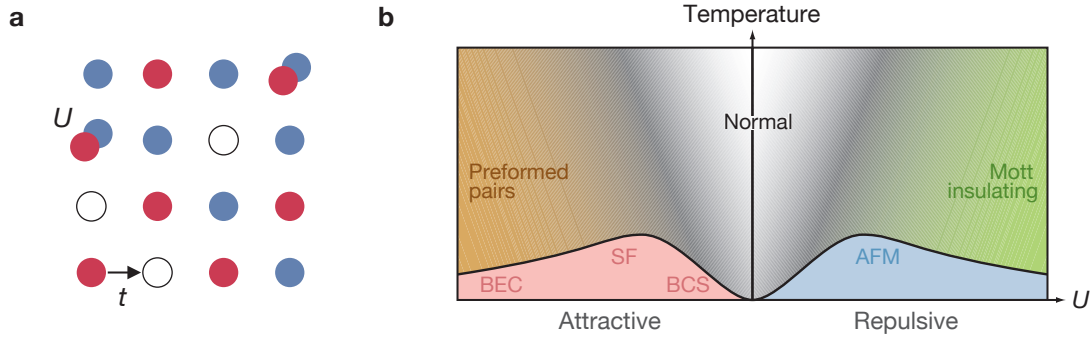
Figure 2.1: Illustration of a Fermi-Hubbard system.a, A two-dimensional Fermi-Hubbard system on a square lattice. The two spin states are represented by two different colors. Particles can hop onto neighboring sites with tunneling amplitude t, and interact with interaction energy U if they inhabit the same lattice site. The depicted state is typical for repulsive interactions $U > t$ with spin ordering and few holes and doubly occupied sites (termed doublons), while singly occupied sites dominate. **b**, Schematic phase diagram of the Fermi-Hubbard model in a cubic lattice at half filling. BEC stands for Bose-Einstein condensate, SF for superfluid, BCS for Bardeen–Cooper–Schrieffer and AFM for antiferromagnet. The phase diagram is adapted from [113].

2.2 Basics

The Fermi-Hubbard model consists of interacting spin-1/2 particles in a single band of a lattice. The particles can hop on nearest-neighbor lattice sites with tunneling amplitude t, and interact with interaction energy U, if two particles of opposite spin inhabit the same lattice site. The Hamiltonian is given by

$$\hat{\mathcal{H}}_{\mathrm{FH}} = -t \sum_{\langle i,j \rangle, \sigma=\uparrow,\downarrow} (\hat{c}_{i,\sigma}^{\dagger} \hat{c}_{j,\sigma} + \mathrm{h.c.}) + U \sum_i \hat{n}_{i,\uparrow} \hat{n}_{i,\downarrow}, \tag{2.1}$$

where $c_{i,\sigma}^{\dagger}$ $(c_{i,\sigma})$ is the creation (annihilation) operator for a fermion of spin σ on site i, $\hat{n}_{i,\sigma}$ is the density operator for a particle of spin σ on site i, and $\langle i,j \rangle$ denotes nearest-neighbor sites. Fig. 2.1a illustrates a Fermi-Hubbard system with its two spin states on a square lattice. The depicted spin ordering is characteristic of low temperatures and repulsive interaction $U > 0$.

Fig. 2.1b shows the phase diagram of the three-dimensional Fermi-Hubbard model depending on interaction strength U/t and temperature for the non-magnetized half-filled case. For low interactions, the hopping term t, which tends to delocalize particles, dominates the physics, while interaction plays a minor role. The system shows a metallic phase with strong density fluctuations.

For higher interactions, the hopping term starts to compete with the interaction U, which tends to localize particles. On the attractive side $U < 0$, particles of opposite spin attract each other and it is energetically favorable to form bound pairs. This parameter regime is of great importance for the study of conventional superconduc-

tivity [114]. At low temperatures, the system enters an *s*-wave superfluid phase of pairs, with BCS character at low interactions and a BEC of tightly bound pairs for strong interactions. In the BEC regime $|U| \gg t$ the pairs can be regarded as hardcore bosons. These repel each other and form a charge-density wave with reduced occupation on every other lattice site while forming a superfluid. In the BCS limit of weak interactions Cooper pairs form and the critical temperature decreases with decreasing U. The studies conducted within this thesis only concern the repulsive side of the Fermi-Hubbard model.

For repulsive interactions, the system shows a crossover from a metallic to an insulating state as interactions dominate over temperature $U \gg k_B T$, with k_B being the Boltzmann constant. The Mott insulator is an incompressible state characterized by localized particles and suppression of double occupancies. For temperatures as low as the spin-exchange energy $J = 4t^2/U$, the spins order within the Mott insulator and form an antiferromagnet (AFM). This phase displays a long-ranged spin correlations reminiscent of a checkerboard pattern. The repulsive side of the Hubbard model can be mapped onto the attractive side through a particle-hole transformation, which maps the spin sector on the density sector [115]. The mapping still holds away from half filling, where doping maps onto magnetization.

Even in the Mott-insulating state, the occupation variance per site is not zero. The remaining variance is caused by doublon-hole fluctuations, i.e. short-lived quantum fluctuations, in which a particle hops onto another particle for a finite amount of time. These fluctuations are suppressed with increasing U/t. In the large U regime, the fluctuations are strongly suppressed and the half-filled Fermi-Hubbard model can be approximated by the antiferromagnetic Heisenberg model

$$\mathcal{H}_{\mathrm{H}} = J \sum_{\langle i,j \rangle} \hat{\boldsymbol{S}}_i \cdot \hat{\boldsymbol{S}}_j \,, \tag{2.2}$$

with spin-exchange coupling $J = 4t^2/U$ and $\hat{\boldsymbol{S}}_i$ being the spin operator at site i. In this limit, each lattice site is occupied by exactly one particle and neither interaction nor tunneling processes can happen directly. The only allowed process is the second order process where two neighboring spins of opposite directions exchange their position via a virtual doublon. The spin-exchange parameter is an instructive quantity even away from the Heisenberg limit. For large but finite U/t the Heisenberg model still poses a valid approximation for Fermi-Hubbard systems, a fact that will be exploited within this thesis.

The correlations in the spin sector between two points can be quantified using the density-normalized connected spin correlator

$$C_{\mathrm{d}}(\boldsymbol{i}, \boldsymbol{j}) = \frac{\langle \hat{S}_i^z \hat{S}_j^z \rangle - \langle \hat{S}_i^z \rangle \langle \hat{S}_j^z \rangle}{\sigma(\hat{S}_i^z)\sigma(\hat{S}_j^z)} \,,$$

where $\sigma(\hat{O})$ is the standard deviation for an Operator $\hat{O}$. For simplicity, we evaluate spin correlations on singly occupied sites, where $\sigma(\hat{S}_i^z)\sigma(\hat{S}_j^z) = 1/4$, the same as in the Heisenberg limit. Furthermore, we usually average over all points with mutual

distance r, such that the correlator becomes

$$C(r) = \frac{1}{\mathcal{N}_r} \sum_{i-j=r} 4 \left(\langle \hat{S}_i^z \hat{S}_j^z \rangle_s - \langle \hat{S}_i^z \rangle_s \langle \hat{S}_j^z \rangle_s \right) , \qquad (2.3)$$

with normalization $\mathcal{N}_r$ equal to the number of positions i, j at distance r and where $\langle \rangle_s$ denotes the expectation value for singly occupied sites. In three-dimensional systems, a phase transition to a long-range spin-ordered state $C(r \gg 1) > 0$ is reached at a finite transition temperature T_N. A maximum of $T_N = 0.3\,t$ is reached at $U/t = 8$ [116]. In two dimensions, in accordance with the Mermin-Wagner theorem [117], there is no spin-ordered state at $T > 0$. However, as temperature decreases, the spin correlation length ξ keeps growing. Spin correlations can thus be used as a thermometer in the low-temperature regime of a 2d Fermi-Hubbard system. In one-dimensional systems, there is no long-range spin order. For finite temperature $T > 0$ such a system displays exponentially decaying spin correlations while having algebraic order at zero temperature [85].

2.3 Simulating the Fermi-Hubbard model using ultracold atoms

The field of cold atoms has been continuously expanding its capabilities of trapping and manipulating atomic particles in a highly controlled environment. Fermionic particles have cooled to quantum degeneracy [23] more than two decades ago, with currently reachable minimum temperatures of $T/T_F \sim 0.05$ [118], where T_F is the Fermi temperature. Nowadays cold atoms are a successful platform for quantum simulation and a promising candidate for programmable quantum computing [8, 119].

2.3.1 Optical lattices

Optical lattices are one of the most powerful tools in quantum simulation [113, 120]. They established themselves as a powerful tool to simulate strongly correlated electrons, by creating an analogy between ultracold atoms in optical lattices and electrons in a solid. The analogy is illustrated in Fig. 2.2. The optical lattice is a periodic grid, created by interfering laser light, which traps atoms in their optical potential. The potential landscape seen by the atoms simulates the ionic lattice structure of condensed matter systems. The atoms represent the electrons in such a system and are thus often referred to as charge, while their hyperfine states represent the electronic spin. The Coulomb interaction between electrons is simulated by the contact interaction between fermions in different hyperfine states [18, 118]. While the distance between atoms in a solid is shorter than 1 nm, the lattice spacing in optical lattices typically ranges from half a micrometer to more than 1 μm. The large spacings enable detailed observations in real space, but also affect the energy scales of the system, which are many orders of magnitude lower. The electrons in a solid at room temperature are thus simulated by atoms in an optical lattice at temperatures of a few nano Kelvin.
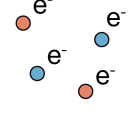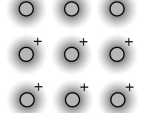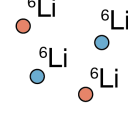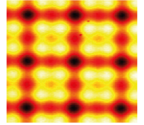
Condensed matter $(T_F \sim 5000$ K$)$	electrons	ionic lattice	$t/h \sim$ THz	Coulomb
Fermi-Hubbard	fermions spin 1/2	2d lattice structure	hopping t	interaction U
Cold atoms $(T_F \sim 300$ nK$)$	neutral atoms	optical lattice (tunable)	$t/h \sim 0.1$-1 kHz (tunable)	on-site collisions (tunable)

Figure 2.2: Analogy between electronic systems and cold atoms. Quantum simulation of electronic systems uses neutral atoms (here ^{6}Li) to simulate the behavior of electrons in solids. Both systems can be approximated by the Fermi-Hubbard model, even though solids can have additional terms [61]. The energy and temperature scales differ by many orders of magnitude but can be scaled to one another. Illustration is taken from [121].

Generation of optical lattices

In an optical lattice, the nodes and antinodes of the standing wave of interfering laser beams form a regular grid. The light frequency is typically far detuned from atomic resonance, creating an optical trap while actual excitation is suppressed. The light field induces an atomic dipole moment, which oscillates at frequency ω given by the laser light. The interaction between driving field and dipole moment leads to an energy shift of the atomic state. Since the light intensity varies spatially, the optical potential created by the varying energy shift forms an optical dipole trap [122]

$$V(\boldsymbol{r}) = \frac{3\pi c^2}{2\omega^3} \frac{\Gamma}{\Delta} I(\boldsymbol{r})\,, \tag{2.4}$$

where c is the speed of light, Γ the linewidth of the optical transition and Δ the detuning from resonance. Red detuned ($\Delta < 0$) optical lattices trap atoms in the antinodes of the standing wave (maximal intensity), while blue detuned ($\Delta > 0$) lattices trap in the nodes (minimal intensity). The lattice depth is often expressed in terms of the recoil energy that an atom of mass m acquires when scattering a photon. It is given by

$$E_R = \frac{h^2}{8ma_{\text{lat}}^2}\,, \tag{2.5}$$
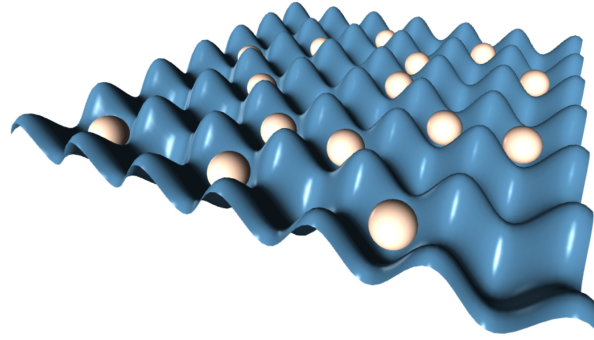
Figure 2.3: Illustration of an optical lattice. It shows a single plane of an optical lattice. The optical potential only allows for atoms to sit in the minima.

with the lattice spacing $a_{\text{lat}} = \lambda/(2\sin(\alpha/2))$, where α is the angle between the two interfering laser beams and λ is the wavelength. The off-resonant scattering rate Γ_{SC} for far-detuned light

$$\Gamma_{\text{SC}} = \frac{3\pi c^2}{2\hbar\omega^3}\left(\frac{\Gamma}{\Delta}\right)^2 I(\boldsymbol{r}) \tag{2.6}$$

decreases with the square of the detuning and thus faster than the trapping potential $V(r) \propto 1/\Delta$ of Eq. (2.4). Heating from off-resonant scattering can be effectively suppressed by choosing laser sources with very large detunings, typically hundreds of nanometers.

Figure 2.3 illustrates ultracold atoms trapped in a two-dimensional plane of an optical lattice potential. For sufficiently deep lattice potentials $V \gtrsim 5E_{\text{R}}$, the system is in the tight-binding limit and can be expressed in terms of Wannier functions [123] which are localized states on individual lattice sites. The overlap between states on neighboring sites depends on the depth of the lattice and gives rise to the tunneling amplitude of particles hopping from one site to the other. In our experiment, we work in a regime where only the lowest band is populated. This system can be well approximated by the Hubbard model.

One of the main challenges for fermions in optical lattices is to reach sufficiently low temperatures. While the metal-to-Mott-insulating crossover is governed by the energy scales given by U, spin correlations only build up when reaching the lower temperatures on the order of the superexchange energy J. In order to realize a long-range antiferromagnet, temperatures considerably below J are thus needed. Consequently, phenomena that arise due to a competition of magnetic and kinetic degrees of freedom like hole pairing and superconductivity (see section below), require even lower temperatures. Cold atom based Fermi-Hubbard simulators have reported temperatures as cold as $T/t = 0.25$ [124]. This is considerably above most temperature estimations for superconductivity and related collective phases [125, 126].

2.3.2   Quantum gas microscopy

Ultracold atoms in optical lattices enable the simulation of condensed matter systems, but their full potential lies in the access to microscopic real-space observables, which
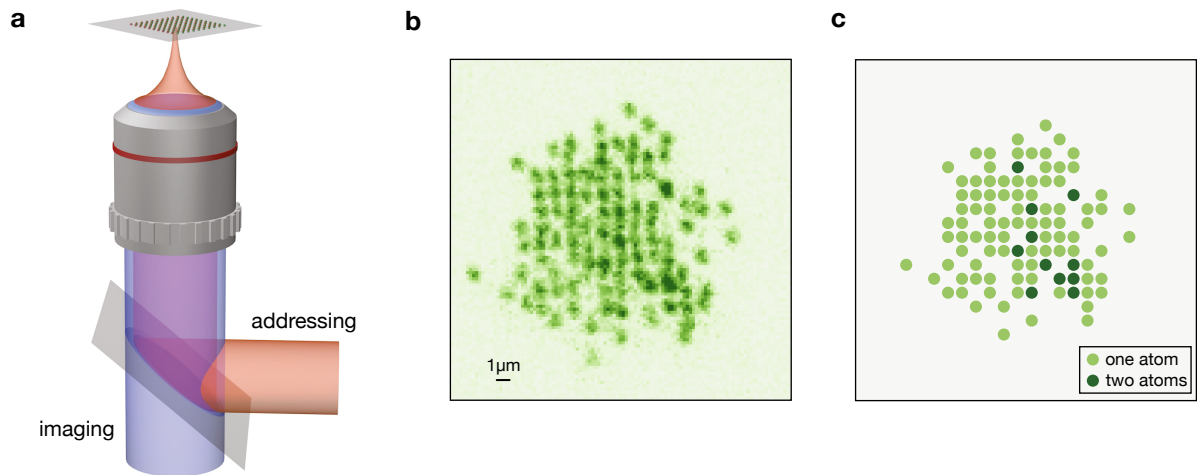
Figure 2.4: Quantum gas microscopy.a, A high-resolution objective as used in quantum gas microscopy. The two-dimensional layer of atoms (top) is imaged through the objective, while an addressing beam can be used to manipulate the atomic system with single-site precision. **b**, Example shot from a quantum gas microscope. Each of the green particles, which are distinguishable in the picture by eye, is the fluorescence by one or two single atoms in the optical lattice. Doubly occupied sites show twice the intensity. **c**, Reconstructed occupation for the fluorescence image. Light green markers represent single atoms, while dark green indicates doubly occupied sites.

are hidden to solid state experiments. Using high-NA objectives in the experimental setup allows for single-site resolved images of the atomic system. In these so-called quantum gas microscopes, an optical resolution of below 1 µm can be achieved using visible light. The access to the full density information allows to measure local and non-local correlation functions in real space. Fig. 2.4 illustrates the single site resolution for a typical quantum gas microscope. The objective is used both to image the atoms in a two-dimensional atomic plane, as well as to address and manipulate selected sites or regions of the system. The images (example snapshot shown in Fig. 2.4b) produced by such a setup show the single atoms as they occupy the lattice grid. Different reconstruction algorithms such as deconvolution with a point-spread function [127] or more advanced methods like machine-learning techniques [128] are used to translate the images to occupation numbers for each lattice site, which can then be further analyzed.

Following the realization of bosonic quantum gas microscopes [41, 129], the first Fermi microscopes [43–46], i.e. quantum gas microscope for fermions in optical lattices, followed half a decade later. They were able to provide in situ observations of antiferromagnetic correlations [47, 50, 130], both in one and two dimensions. Potential shaping in order to reduce the confining potential from the lattice beams has led to the realization of antiferromagnetic correlations, ranging as far as the system size [124]. Spin resolution is often achieved by applying a pushout beam to one of the spin species [50]. This technique has the disadvantage that holes cannot be distinguished from the pushed-out spin species, while doublons cannot be distinguished

from the remaining spin species. The pushout method is thus not suited to investigate the interplay of spin and charge away from half filling, or in systems that are not in the Mott insulating regime. Our method, which allows for full resolution of spin and charge, is to apply a Stern-Gerlach separation to the spin states. The two spin states can be spatially separated either in plane [47] or in the vertical direction [56, 57].

A quantum gas microscope can, however, only access a projected part of the wavefunction in Fock space. The process of imaging the atoms leads to a collapse of the wavefunction. Thus thousands of repetitions are necessary to extract the occupation distribution of the full quantum state. The time it takes to produce a cloud of cold atoms and take a single snapshot lies at $\sim 20\,$s for most quantum gas microscopes, including the one used in this thesis. However, research groups around the world are making progress in the quest for faster cycle times, with some experiments having reported the production of a degenerate Fermi gas within $4\,$s [131].

2.4   The doped Fermi-Hubbard model

Doping the Fermi-Hubbard model means changing the ratio of particles to lattice sites. The system is called hole doped below half filling, and doublon doped above half filling. This is analogous to doping in real materials, where a small amount of foreign atoms is introduced in order to create either an excess or a deficiency of electrons. The Fermi-Hubbard model is particle-hole symmetric [132], meaning doublon doping can be mapped on hole doping and vice versa.

The doped Fermi-Hubbard model is extensively studied both theoretically and experimentally due to its close relation with high-temperature superconductors. Fig. 2.5 shows the (conjectured) phase diagram of the doped Fermi-Hubbard model in the strongly interacting regime $U \gg t$. It is largely inspired by the high-temperature superconducting cuprates [61]. The antiferromagnetic Mott insulator at half filling transitions into a pseudogap phase [133] upon doping. At higher temperatures and intermediate doping, a strange metallic phase appears, which shows anomalous properties such as a resistivity scaling linearly with temperature [134]. At low temperatures and intermediate doping, a d-wave superconducting phase is observed in the cuprates [70] and conjectured to appear in the Fermi-Hubbard model. However, due to a lack of experimental evidence and established theoretical methods, the Fermi-Hubbard phase diagram remains controversial, especially about the existence of a superconducting phase [77, 104, 135, 136]. Despite this uncertainty, the Fermi Hubbard model displays many of the typical phenomena of the cuprates, like antiferromagnetism, pairs and stripes, and pseudogap physics [61, 66, 137]. One can thus gain insight into the intricate mechanisms and competitions at play in the cuprates by studying the Fermi-Hubbard model. In the following, we will discuss some of the key features of the doped Fermi-Hubbard model that have been studied within this thesis.
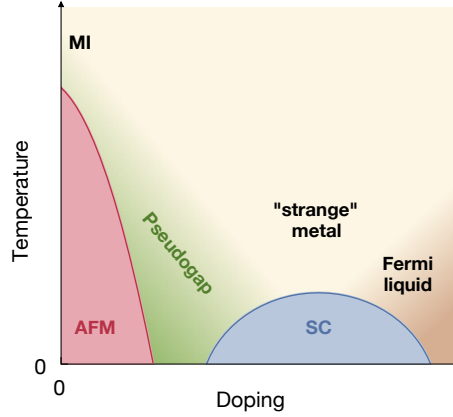
Figure 2.5: Phase diagram of the Fermi-Hubbard model and the cuprates. Conjectured phase diagram of the two-dimensional Fermi-Hubbard model. The antiferromagnet (AFM) transitions into a pseudogap phase and a strange metallic phase upon doping. At low temperatures, a superconducting (SC) phase is conjectured, but other collective effects like stripes are also in discussion.

2.4.1 The $t - J$ model

We consider only the strongly interacting regime $U \gg t$, as it is the relevant regime for the cuprate materials. In this regime, doublons are strongly suppressed, similar to the Heisenberg regime discussed earlier. However, dopants can still move through the system with hopping amplitude t. The doped Hubbard model with strong interactions can thus be approximated by an expansion to leading order in t/U [102], leading to a simplified effective model. The elimination of doublons considerably reduces the Hilbert space, thus enhancing the possibility for numerical simulations. The $t - J$ model typically refers to the Hamiltonian

$$
\hat{\mathcal{H}}_{tJ} = - \sum_{\langle i,j \rangle, \sigma} \hat{\mathcal{P}} \left(t \, \hat{c}_{i,\sigma}^\dagger \hat{c}_{j,\sigma} + \text{h.c.} \right) \hat{\mathcal{P}} +
$$
$$
+ \sum_{\langle i,j \rangle} J \left(\hat{\mathbf{S}}_i \cdot \hat{\mathbf{S}}_j - \frac{\hat{n}_i \hat{n}_j}{4} \right),
\tag{2.7}
$$

where $\hat{\mathcal{P}}$ projects to the subspace without doublons. The model consists of a hopping term describing nearest-neighbor tunneling of dopants and a spin-exchange term describing spin-spin interaction.

The expansion to leading order in t/U, however, yields another term, which is usually omitted in the $t - J$ model. That term is also of order t^2/U and describes next-nearest-neighbor tunneling of dopants [102]. In this process a hole (or doublon) switches position with a spin two sites away, via a virtual doublon, similar to the spin-exchange process. While the term is considerably smaller than the nearest neighbor hopping term, it allows for hole movement without moving spins from one sublattice to another.
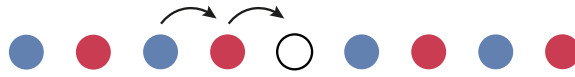
Figure 2.6: Hole motion in a Fermi-Hubbard chain. A hole can move through a one-dimensional Fermi-Hubbard chain without magnetic energy cost. Antiferromagnetic spin correlations get stretched by one site around the hole.

2.4.2   Spin-charge separation

Before investigating the physics in the two-dimensional model, we will take a look at the physics in one-dimensional Fermi-Hubbard chains. One-dimensional systems are characterized by decoupled spin and charge excitations that can propagate independently [85, 138]. Fig. 2.6 illustrates how holes move in a doped chain without disturbing the spin ordering of the system.

The low-energy regime of Fermi-Hubbard chains is treated as a Luttinger liquid [139, 140], possessing collective wave excitations with linear dispersion and long wavelengths. Spin-charge separation in equilibrium has been observed experimentally in a quantum gas microscope by revealing the antiferromagnetic spin correlations across a hole [141]. Incommensurate spin correlations, as predicted by the Luttinger liquid description, have been observed microscopically at higher doping [142].

In the course of this thesis, spin-charge separation has been observed beyond the Luttinger liquid regime, by creating a highly energetic excitation in the spin and charge sector through a local quench. The spin and charge excitations are created together, by removing one fermion from the chain. Subsequently, we observed how the excitations dynamically separate. They propagate through the system at different velocities and independently from each other. The results are discussed in detail in [143].

2.4.3   Competition of kinetic and magnetic energy

In two-dimensional AFM systems, spin and charge excitations do not decouple. Instead, magnetic and kinetic degrees of freedom compete with each other. A hole in a doped system strives to minimize its kinetic energy by delocalizing. However, a delocalized hole frustrates the antiferromagnetic spin order and is thus unfavorable in magnetic energy [111]. This competition of the tunneling energy t and spin exchange J can be understood on the level of an illustration, as in Fig. 2.7. The hole motion locally creates ferromagnetic spin bonds with high magnetic energy cost. This limits the range over which the hole can move in the system, as long as the spin configuration is frozen.

Instead of delocalizing in the system, the hole is confined to a small area, in which it is dressed with a magnetic cloud of reduced antiferromagnetic spin correlations. The compound object of hole and dressing cloud forms a magnetic polaron, with an altered effective mass and reduced motion governed by the spin-exchange rate J. Polarons have been observed in cuprates indirectly, through the suppression of the single particle bandwidth [144, 145]. In a cold atom quantum simulator, polarons have been observed in equilibrium [146], and their dynamical formation has been
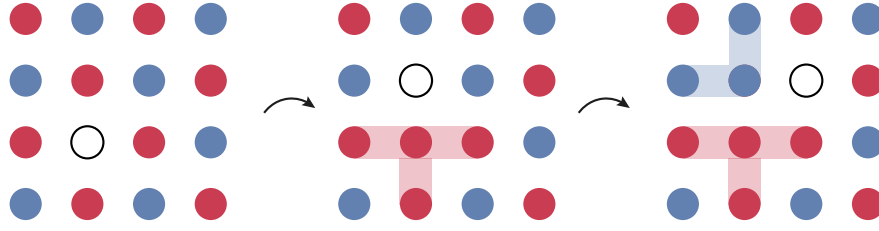
Figure 2.7: Competition of kinetic and magnetic energy. A hole moving through a two-dimensional Fermi-Hubbard system disturbs the spin order in the system and thus costs magnetic energy. For each site it hops further, the spin order is reduced, as illustrated by the colored bonds. As a result, the hole cannot be delocalized over large distances but stays confined to a small region. Within this area, it disrupts the spin correlations.

studied after releasing a pinned hole [147].

In the course of this PhD thesis, we have observed the evolution of polaron effects from the lightly doped regime into the strong doping regime. We find that the polaron picture holds for low doping below $\approx 20\%$ but breaks down at higher doping when the system goes through a crossover into the Fermi liquid regime. In Fig. 2.8 the observed spin correlations around a hole are shown for different doping levels. For low doping, the correlations correspond to a magnetic polaron, with antiferromagnetic character for diagonal spin correlations around the hole. Nearest neighbor spins are more ferromagnetic in the vicinity of a hole than they are in the antiferromagnetic background. At higher doping, however, this picture breaks down and we find that nearest-neighbor bonds become more antiferromagnetic in the presence of holes than in the absence of holes. At this point, the system crosses over to the Fermi-liquid phase, which does not host polarons. A detailed discussion of the results of this project can be found in [121].
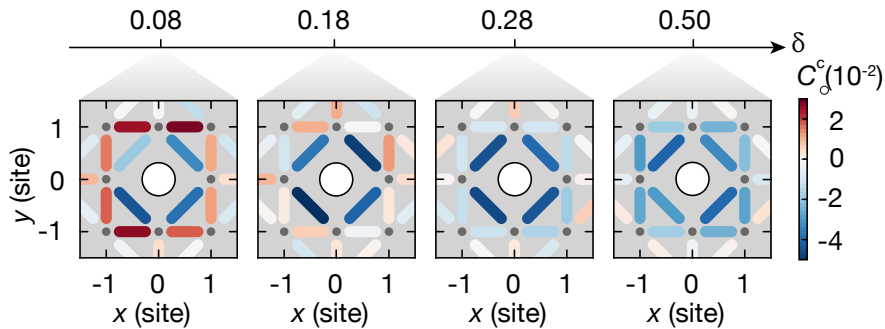
Figure 2.8: Polaron evolution upon doping. We measured the magnetic bonds around holes for different levels of doping δ. $C_\circ^c$ is a connected three-point correlator where the spin background in the absence of a hole is subtracted. It highlights the difference between the magnetic environment with and without a hole. At low doping, the correlations are compatible with magnetic polaron, while at high doping the signature of a polaron vanishes. Further analysis can be found in [121].
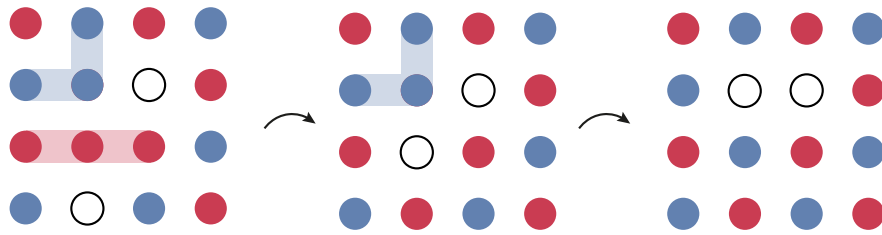
Figure 2.9: Pairing mechanism in doped antiferromagnets. The starting point of this illustration is the frustrated antiferromagnet of Fig. 2.7, which has been disturbed by a single moving hole. If now a second hole follows along the path of the first hole, it can reshuffle the spin order, thereby undoing the magnetic energy cost of the first hole. This way the two holes can move together through the system without a major impact on the spin sector.

2.4.4 Pairing and superconductivity

The competition of spin and charge degrees of freedom is at the heart of many intriguing phenomena of the cuprate materials and the Fermi-Hubbard model. Amongst the most famous ones is the emergence of superconductivity. A complete understanding of the mechanisms underlying superconductivity, as well as its relation to related phenomena like stripes [148, 149], remains elusive to this day. For superconductivity to emerge, charge carriers, i.e. doped holes or doublons, need to form pairs. At suitable density and mobility, these bosonic pairs can condense into a superfluid state - the superconducting phase - in which the resistivity vanishes. A common assumption is that the magnetic fluctuations in the antiferromagnetic background mediate the pairing process [150].

To understand the proposed binding mechanism, we observe that the frustration created by a single hole in an antiferromagnetic spin environment can be lifted when two holes move together. This process is illustrated in Fig. 2.9. A single hole moving through an antiferromagnet locally destroys the spin correlations in the system. If a second hole follows the path of the first hole, it can restore the magnetic order in the system. Two holes together can thus move together while keeping the spin sector largely undisturbed - a process that allows for efficient hole delocalization. The effective attraction between holes in doped antiferromagnets is thus based on the lowering of magnetic exchange interaction.

However, the binding of holes into pairs constrains their motion because the two holes mutually block each other's spatial fluctuations. The reduced short-range mobility results in an increase in kinetic energies. Thus the pairing process competes with individual hole motion. The effective attraction of holes, due to enhanced delocalization over the full system, competes with a short-scale repulsion caused by Pauli blocking of holes. Binding can thus only happen as a compromise between pairing and mutual distance, balancing the magnetic energy advantage and repulsion. The effect is a comparably low binding energy, typically much lower than the spin-exchange energy. Accurate theoretical analysis of this problem remains a key problem in quantum many-body physics [151–153].

2.5 Fermi-Hubbard Ladders

The two-dimensional Fermi-Hubbard model poses many challenges to our understanding. While the one-dimensional Hubbard model can be more easily tackled theoretically, it does not display the same phenomena as the two-dimensional model. In particular, it does not share the phase diagram of the high-temperature superconducting cuprates. Fermi-Hubbard two-leg ladder systems with two coupled legs of length L are more complicated than single chains, but easier to simulate on classical computers than two-dimensional systems. They are thus comparably well understood theoretically while displaying many of the relevant features of the cuprates like the characteristic competition between spin and charge degrees of freedom.

More generally, an n-leg ladder system consists of n coupled legs. For large n it thus approaches a two-dimensional system, whereas $n = 1$ corresponds to a one-dimensional chain. Intermediate n constitute a crossover from one to two dimensions. This crossover is however not smooth but displays different properties depending on the parity of n [154] (see also below at 2.5.2).

Unless otherwise specified, we use the term *ladder* within this thesis to refer to two-leg ladders. A ladder system of $L \times 2$ coupled sites is illustrated in Fig. 2.10a. The particles can tunnel along the rungs (legs) of the system with tunneling amplitude $t_\perp$ ($t_\parallel$). Ladder systems can be simulated theoretically, e.g. using DMRG and have been investigated intensively, see e.g. [85]. They have played an instrumental role in the elucidation of a magnetic pairing mechanism [84, 155], but have also been used as a simple model to investigate symmetry-protected-topological phases [101, 156], artificial gauge fields [157–160], Josephson junctions [161–164] and many other phenomena.

2.5.1 Single-particle band structure

Fermi-Hubbard ladders are described by the Hamiltonian

$$
\hat{\mathcal{H}}_{\mathrm{FHL}} = - \left(t_\parallel \sum_{x,y\,\sigma} \hat{c}^\dagger_{x,y,\sigma} \hat{c}_{x+1,y,\sigma} + t_\perp \sum_{x\,\sigma} \hat{c}^\dagger_{x,0,\sigma} \hat{c}_{x,1,\sigma} + \mathrm{h.c.} \right) + U \sum_i \hat{n}_{i,\uparrow} \hat{n}_{i,\downarrow} , \quad (2.8)
$$

with tunneling amplitude $t_\perp$ ($t_\parallel$) along the rungs (legs) of the system. In order to find the band structure for single particles, following e.g. [159, 160], we first consider only a single leg without interactions. The momentum state operators are

$$
\hat{d}_{k,\sigma} = \frac{1}{\sqrt{L}} \sum_j \hat{c}_{j,\sigma} e^{ikr_j} ,
$$

where r_j is the location of site j. The Hamiltonian can be formulated using the momentum eigenstates with eigenenergies that depend on the cosine of the quasimomentum

$$
\hat{\mathcal{H}} = \sum_{k,\sigma} \epsilon(k) \hat{d}^\dagger_{k,\sigma} \hat{d}_{k,\sigma} , \qquad \epsilon(k) = -2t_\parallel \cos(ka) .
$$

a

b
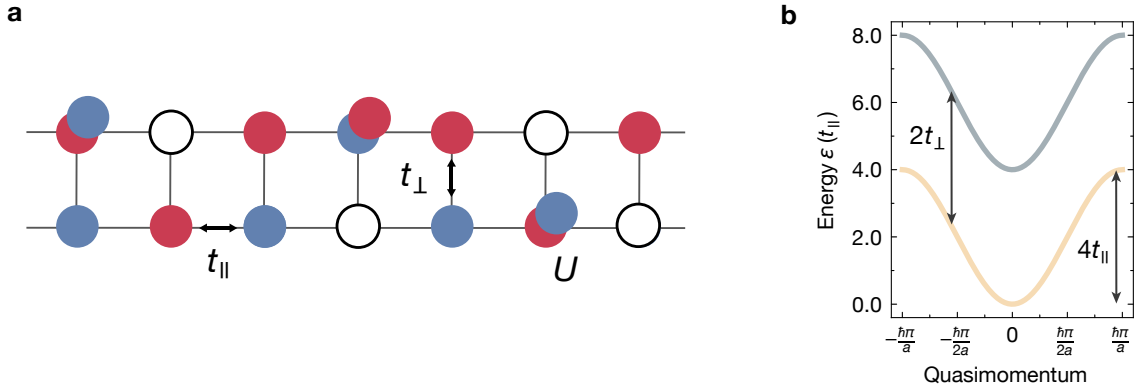
Figure 2.10: Fermi-Hubbard ladders and their band structure. **a**, Holes in a ladder system can move with tunneling amplitude $t_\perp$ ($t_\parallel$) along the rungs (legs). Two particles of opposite spin that occupy the same lattice site interact with interaction energy U. **b**, Single-particle band structure of tight-binding ladders depending on quasimomentum k along the leg. The two disconnected bands, each of width $4\,t_\parallel$, result from the symmetric and antisymmetric states along the rung and are shifted with respect to each other by an energy of $2\,t_\perp$. The exemplary plotted band structure corresponds to a parameter setting of $t_\perp = 2\,t_\parallel$.

If we consider a single rung of the ladder, we find a double well with eigenstates

$$|\Psi^\pm\rangle = \frac{1}{\sqrt{2}}(|\mathrm{R}\rangle \pm |\mathrm{L}\rangle)\,, \qquad \epsilon^\pm = \pm t_\perp\,.$$

Since the two directions are separable, the band structure of the ladder system follows as the sum of the leg and rung eigenenergies, as shown in Fig. 2.10b. Two bands of width $4t_\parallel$, corresponding to the bands of a single chain, are shifted with respect to each other by $2t_\perp$. The shift corresponds to the energy splitting between the symmetric and antisymmetric states along the rung.

2.5.2   Interacting ladders

For a half-filled ladder system of two interacting spin states, the band structure derived above suggests insulating behavior starting around $U \geq 4t_\parallel + 2t_\perp$, that is, when the interaction energy for a double occupancy exceeds the energy cost of populating the band of the antisymmetric rung states. In the regime of very large interactions $U \gg t_\perp, t_\parallel$, doublon-hole fluctuations are strongly suppressed and the system approximates the Heisenberg limit of Eq. (2.2).

Antiferromagnetic Heisenberg ladders

In the Heisenberg regime with spin exchange $J = 4t^2/U > 0$, the properties of an n-leg ladder system depend on the number of legs n [154]. While antiferromagnetic

correlations appear for all numbers of legs, they show different distance dependencies whether the number of legs is even, or odd. Ladders with an odd number of legs display magnetic order with a power-law decay of spin correlations versus distance. Furthermore, odd n systems do not display a spin excitation gap. Even-leg ladders, on the other hand, have a disordered ground state with purely short-ranged spin correlations which decay exponentially. They display an energy gap associated with the cost of a spin excitation. This arises from a tendency of the spins in even-leg ladders to form singlet bonds, which has a strong conceptual connection to the resonating valence bond (RVB) state [75]. Following this, the two-leg ladder system has a spin gap due to its dominant singlet character along the rungs with short-ranged spin correlations along the leg. The antiferromagnetic two-leg ladder is depicted in Fig. 2.11, illustrating its coupling parameters and singlet character along the rungs which underlies the spin gap.

Ferromagnetic rung coupling

If the exchange coupling J in the Heisenberg model becomes negative, the ground state has ferromagnetic spin order. Even though the Fermi-Hubbard model of Eq. (2.1) cannot have a negative exchange coupling in any parameter limit, the scenario can be reached for example through a potential offset $\Delta > U$ between neighboring lattice sites (for details see section 4.3.1). Here we discuss the Heisenberg model for antiferromagnetic leg coupling $J_\parallel > 0$ and ferromagnetic rung coupling $J_\perp < 0$. Similar to the antiferromagnetic case, this configuration shows a strong dependence on the number of legs n [85]. For even leg ladders with large negative $J_\perp$, the ferromagnetic rungs add up to integer spin values $S = n/2$. For the resulting antiferromagnetic spin-S chain the Haldane conjecture [165] applies, according to which integer spin chains are gapped, while half-integer spin chains are gapless. In particular, this means that the two-leg ladder with ferromagnetic rung coupling can be treated as a gapped integer-spin chain. This system realizes the Haldane phase of spin-1 chains, a paradigmatic topological phase that will be introduced in detail later in this chapter.

2.5.3 Doped $t - J$ ladders

Doped ladder systems [166, 167] have served as an instructive model for theoretical investigation of doping in the Hubbard model [81–84]. Similar to the cuprates, doped ladders can display a superconducting phase, as well as strange metallic behavior and pseudogap characteristics [89].

Fig. 2.11 depicts a lightly doped ladder system in the $t - J$ regime of strong interactions. Holes tunnel with tunneling amplitude $t_\perp (t_\parallel)$ along the rungs (legs), while spin exchange takes place with exchange coupling $J_\perp (J_\parallel)$. With these parameters the
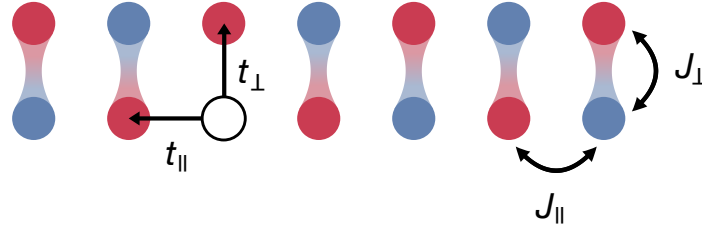
Figure 2.11: $t - J$ **ladders.** A ladder with strong singlet bonds along the rungs is displayed. Holes in this system can move with tunneling amplitude $t_\perp$ ($t_\parallel$) along the rungs (legs), while spin exchange takes place with exchange coupling $J_\perp$ ($J_\parallel$). In the regime of strong rung coupling $J_\perp \gg J_\parallel$, singlets form along the rungs, leading to a spin gap on the order of $J_\perp$. With increasing leg coupling the rungs are not inhabited by pure singlets anymore, but instead, spin correlations also build up along the legs. The strength of spin correlations along the rung vs. the leg depends on the coupling parameters, but a spin gap persists for all $J_\perp / J_\parallel > 0$.

$t - J$ ladder Hamiltonian is

$$\hat{\mathcal{H}}_{tJ\mathrm{L}} = \sum_{\langle i,j \rangle, \sigma} \hat{\mathcal{P}} \left(-t_{ij}\, \hat{c}^\dagger_{i,\sigma} \hat{c}_{j,\sigma} + \mathrm{h.c.} \right) \hat{\mathcal{P}} +$$
$$+ \sum_{\langle i,j \rangle} J_{ij} \left(\hat{\mathbf{S}}_i \cdot \hat{\mathbf{S}}_j - \frac{\hat{n}_i \hat{n}_j}{4} \right), \tag{2.9}$$

where the hopping energy is $t_{ij} = t_\parallel$ ($t_\perp$) and the superexchange energy is $J_{ij} = J_\parallel$ ($J_\perp$) for nearest-neighbour sites i, j on the same leg (rung).

Theoretical studies of one and two holes in ladder systems have found an interplay of spin- and charge degree of freedom similar to two-dimensional systems and pairing of holes at suitable parameters [166, 168–170]. A paradigmatic case for theoretical investigation is the regime where the inter-chain spin exchange is larger than single-particle interchain hopping, i.e. $J_\perp > t_\perp$ [155]. This regime exhibits large binding energies and serves as a toy model to elucidate the pairing mechanism without further complication from competing processes like hole repulsion. Fig. 2.12 illustrates the pairing mechanism in this parameter regime. As in the 2D case, it is favorable for holes to be delocalized in the system in order to reduce kinetic energy. For a single hole, delocalization however competes with the magnetic order along the rungs of the system. A hole that moves through the system, shifts the singlet bonds along the rungs. If a second hole moves along with the first one, it restores the singlets. Two holes together can thus delocalize along the ladder and minimize their kinetic energy, while causing only minimal magnetic energy cost. This energy advantage leads to the binding of holes. This picture however only holds in the regime $J_\perp \gg t_\perp$, where the tunneling along the rungs is negligible compared to the spin exchange. Unfortunately, these parameters are unphysical within the framework of the pure Fermi-Hubbard model. A realization of this toy system had thus been lacking until now (see Ch. 4 for
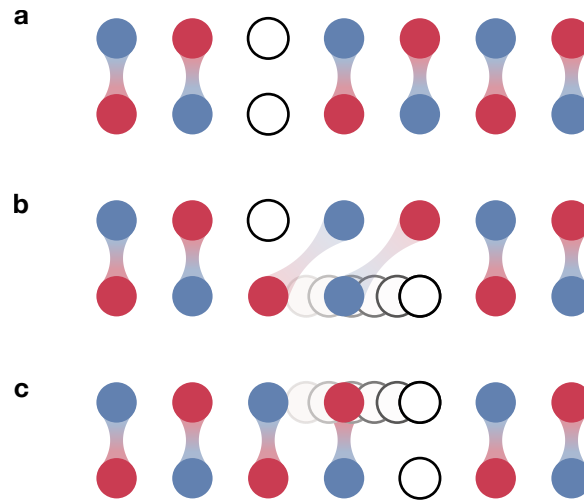
Figure 2.12: Pairing mechanism in ladder systems. The figure illustrates the pairing mechanism in ladder systems, where spin exchange dominates over the tunneling amplitude along the rungs. **a**, A doped ladder system with singlet bonds along the rungs and two holes. **b**, If one hole moves through the system, it breaks the singlet bonds on its way, thus increasing the magnetic energy of the system. **c**, If a second hole moves along with the first hole, it restores the singlet bonds. Thus two holes together can move through the system with minimal magnetic energy cost.

further explanation and realization of this system).

Physical realizations of ladders

Ladder systems have been realized in solid state materials, for example the series $Sr_{n-1}Cu_{n+1}O_{2n}$ [171, 172], with compounds possessing antiferromagnetic spin exchange and a spin gap [173]. Similar materials, like $Sr_{14-x}Ca_xCu_{24}O_{41}$, are ladder compounds that have been shown to display superconductivity upon doping [87–89, 174]. These realizations of ladder materials, and especially the observation of a superconducting phase, inspired further interest in the investigation of ladder materials. Quantum simulation offers a complementary path to solid state experiments, allowing to extract microscopic observables and shed new light on the intriguing properties of these systems. In the last 10 years, bosonic ladder systems have been realized in cold atom experiments [158, 175] and enabled the observation of chiral currents and the Meissner effect [176] relevant for superconductors exposed to magnetic fields. To the best of our knowledge, the experiments carried out within this PhD thesis present the first realization of fermionic ladders using cold atoms.

2.6 Symmetry-protected topological phases

Another intriguing topic of modern quantum physics is symmetry-protected topological (SPT) phases. This phenomenon can also be studied in ladder systems. Undoped

Fermi-Hubbard ladders realize one of the most iconic topological phases, the so-called Haldane phase [100, 101, 165]. In the following, we will introduce SPT phases as a special class of topological phases and provide details about the Haldane phase and its realization in spin-1/2 ladder systems.

The discovery of topological phases [90, 177] has led to a new understanding of phase transitions. Instead of relying on symmetry-breaking and local order parameters, as in the Landau-theory [91], these phases are distinct due to their topological properties. While two topologically different phases might not be distinguishable locally, they have distinct global topological properties, like a cylinder and a Möbius strip, which locally look identical. The topological order parameters that identify the phases are called topological invariants. Two states are in the same phase if they can be continuously transformed into one another without changing the topological invariant. A common example of a topological invariant is the number of holes in a geometric object. A donut cannot be transformed into a pretzel, without punching additional holes, i.e. changing the topological invariant, while a donut can be transformed into a cup while leaving the topology intact.

Topological quantum matter is intriguing, not only due to the rich topological properties, but also because it can display various exotic phenomena like quantized transport [178], or excitations with fractional charge [179] that can be exploited for technological applications. The robustness of topological phases with respect to local perturbations makes them prime candidates for application in quantum computation and quantum memory [180–182]. Information encoded in a topological invariant is relatively stable regarding system imperfections, which is highly relevant for reliable information storage.

Topological phases can be classified into long-range entangled states, which are said to have topological order, and short-range entangled states, which, if the Hamiltonian possesses a global symmetry, are said to have SPT order [183]. Quantum Hall states [184] are an example of topological order, while topological insulators of non-interacting fermions [185] and the spin-1 Haldane phase are examples of SPT-ordered phases.

SPT phases are short-range entangled states that are characterized by a non-local order parameter. They have an excitation gap in the bulk with a unique ground state and robust degenerate edge states at the boundaries of the system. This is known as bulk-edge-correspondence of topological phases [93, 95]. Two SPT states belong to the same phase if they can be transformed into each other with a symmetry-preserving deformation.

2.6.1 The Haldane phase

The Haldane phase is one of the most paradigmatic cases of a symmetry-protected topological phase [96, 186, 187]. It appears in the ground state of antiferromagnetic spin-1 Heisenberg chains and is named after Duncan Haldane, who received the Nobel Prize 2016 (together with M. Kosterlitz and D. Thouless), for his work using topological concepts to describe spin chains (see e.g. [165]). A central aspect of that work is the Haldane conjecture, stating that half-integer spin chains, such as spin-1/2 or spin-
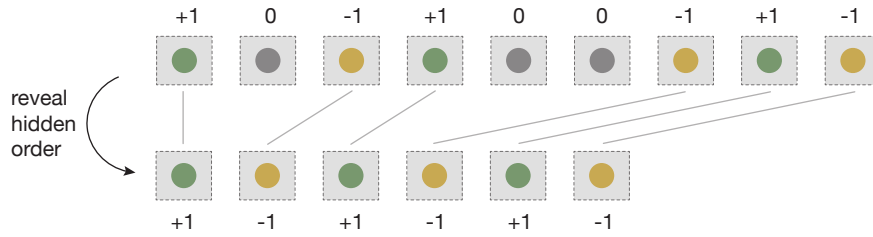
Figure 2.13: Hidden afm order in the Haldane phase. The figure illustrates the hidden spin order in antiferromagnetic spin-1 chains. Green balls represent spin state $S^z = 1$, grey balls $S^z = 0$ and yellow balls $S^z = -1$. The spin-spin correlations in the chain (upper row) decay quickly, due to the varying appearance of spin states -1, 0 and 1. However, if the spin $S^z = 0$ states are removed from the chain, also called "squeezed space"[188], an antiferromagnetic ordering of the spins is revealed.

3/2 chains, are gapless with a power-law decay of spin correlations, while integer spin chains are gapped and show exponentially decaying spin correlations [99, 102, 165]. The parity dependence of antiferromagnetic n-leg ladders discussed above is closely related to this conjecture. A consequence of the Haldane conjecture is that only integer spin chains have SPT order.

The Haldane phase of antiferromagnetic spin-1 chains is protected by an $SO(3)$ symmetry (or its $\mathbb{Z}_2 \times \mathbb{Z}_2$ subgroup), as well as by time-reversal symmetry. The ground state of such a chain has no spontaneous symmetry breaking. Instead, it is a disordered state with short-range magnetic correlations. However, a hidden, long-range antiferromagnetic order can be revealed by employing a non-local string correlator. This string correlator correlates two sites by taking into account all spins in between them, thus connecting the sites with a *string*, instead of considering them separately, i.e. only locally. The principle of this hidden correlation can be seen in Fig. 2.13. The spin-1 chain displays no long-range spin order $C(d)$. However, if the position of the $S^z = 0$ states is taken into account, the hidden order of alternating spin $S^z = 1$ and $S^z = -1$ becomes visible.

The Haldane chain furthermore displays a spin-excitation gap in the bulk and fourfold degenerate edge states at the ends of the chain. These edge states carry spin-1/2 excitations, where the bulk $SO(3)$ symmetry fractionalizes into a $SU(2)$ symmetry [96, 187]. They are robust against perturbations that commute with the protecting SO(3) spin rotation symmetry. The edge states furthermore have a finite localization length ξ, meaning the spin-1/2 excitation is not fully localized on the edge site but can penetrate into the bulk with exponentially decaying amplitude.

The AKLT model

To gain a better understanding of the Haldane phase, it is instructive to consider the AKLT model, introduced by Affleck, Kennedy, Lieb, and Tasaki [189, 190]. The AKLT model was designed to satisfy the requirements of the Haldane phase. It demonstrates the mechanisms leading to the typical signatures of the Haldane phase, such
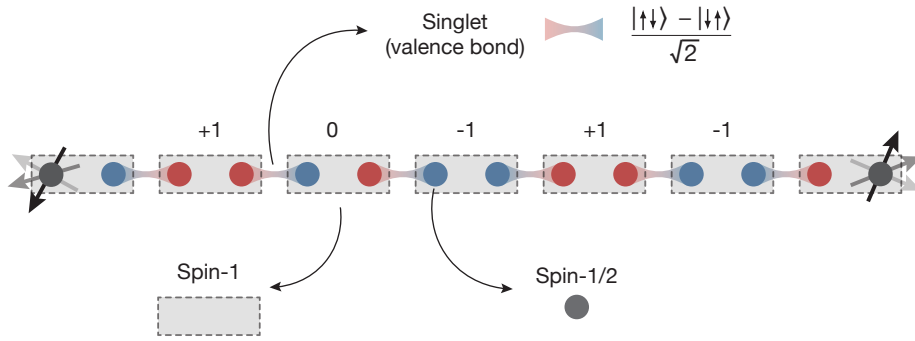
Figure 2.14: Illustration of the AKLT model. Spin-1 objects (grey boxes) are composed of two spin-1/2 objects (red and blue balls). The spin-1/2 objects form singlet bonds (shaded bonds) with neighboring particles across two neighboring spin-1 objects. At the boundaries of the chain, there are spin-1/2 particles that are not bound into singlets. These are free to point in any direction, i.e. to assume any linear combination of spin up and down. This degeneracy is indicated by the fading arrows.

as the fractional edge states and the hidden antiferromagnetic order. In this model, a spin-1 particle is formed out of two spin-1/2 particles in a triplet state. Between the spin-1 objects sit valence bonds, each connecting two spin-1/2 located in neighboring spin-1. The idea is illustrated in Fig. 2.14. The valence bonds (singlets) fully define a unique state in the bulk. However, the edges of the chain feature 'free' spin-1/2 particles, that cannot form singlets due to a missing neighbor. The edges thus support four degenerate states $|\uparrow_l \downarrow_r\rangle$, $|\downarrow_l \uparrow_r\rangle$, $|\uparrow_l \uparrow_r\rangle$ and $|\downarrow_l \downarrow_r\rangle$. Due to the spin-1/2 degree of freedom within this spin-1 chain, the edge states are said to be fractional.

The Hamiltonian describing this spin-1 chain connected by valence bonds is given by

$$\hat{\mathcal{H}}_{\mathrm{AKLT}} = \sum_j P_2(\hat{\mathbf{S}}^1{}_j + \hat{\mathbf{S}}^1{}_{j+1})$$

$$= \sum_j \left[\frac{1}{2}\hat{\mathbf{S}}^1{}_j\hat{\mathbf{S}}^1{}_{j+1} + \frac{1}{6}(\hat{\mathbf{S}}^1{}_j\hat{\mathbf{S}}^1{}_{j+1})^2 + 1/3 \right]$$

where $\hat{\mathbf{S}}^1{}_i$ is the spin-1 spin operator on site i, and $P_2(\hat{\mathbf{S}}_j + \hat{\mathbf{S}}_{j+1})$ is a projector acting on neighboring spin-1 objects, blocking them from forming a total spin-2 state. This restriction produces the valence bonds. The model is related to the antiferromagnetic spin-1 Heisenberg by being a spin-1 chain with antiferromagnetic interactions, but with extra terms such that the AKLT state is the exact ground state. The advantage of this model is the existence of an exact solution, which was provided with its proposal. It thus offers crucial insight into the physics of spin-1 chains. Furthermore, it displays the characteristics of the Haldane phase and illustrates the origin of these properties. We have already seen how the fractional edge modes emerge from the spin-1/2 description of the AKLT chain. The hidden antiferromagnetic order arises similarly from the spin-1/2 picture. Projecting the singlet states on spin-up and spin-downs leads to perfectly alternating order of $S^z = 1$ and $S^z = -1$, with randomly placed $S^z = 0$ objects between them. The perfect anticorrelation of spins within a singlet ensures
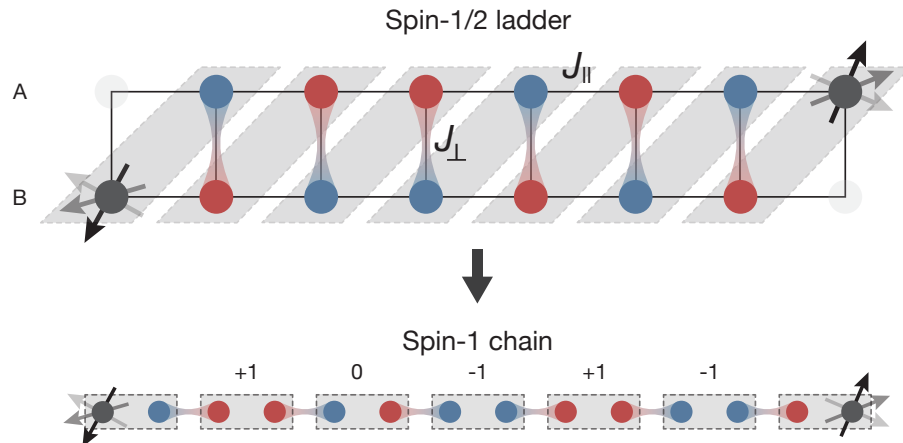
Figure 2.15: Mapping a ladder on a spin-1 chain. The illustration shows how an antiferromagnetic spin-1/2 ladder with legs A and B can be mapped onto an AKLT-like spin-1 chain. In the strong rung coupling regime $J_\perp \gg J_\parallel$, the spins form singlets along the rungs on the ladder, which are translated to the valence bonds between spin-1 objects of the AKLT model. By defining the spin-1 objects in diagonal unit cells (grey diagonal boxes), each of them contains the endpoints of two different such bonds. The endpoints of the ladder systems are rungs that are cut in half, only allowing particles on one side. We note that the mapping to the spin-1 chain is not exact, but both systems are adiabatically connected.

that a spin $S^z = -1$ can not be followed by another $S^z = -1$, without a $S^z = +1$ between them. The AKLT model also gives a visual idea of the short-range entanglement involved in the Haldane phase and other SPT phases. It directly follows from the construction and reaches only over two spin-1s. Strictly speaking, the Haldane phase only exists at zero temperature in the thermodynamic limit. This can also be understood from the AKLT model: At finite temperature, each of the singlets has a finite probability for a triplet excitation. Since there are infinitely many singlets in a chain at the thermodynamic limit, any finite temperature suffices to break at least one singlet in the chain. This triplet destroys the hidden antiferromagnetic order, the order parameter for the Haldane phase (see Eq. (2.14) below for details).

2.6.2   In Fermi-Hubbard ladders

The AKLT model illustrates how the Haldane phase can be understood from spin-1/2 fermions. In our platform, we construct the Haldane phase using Fermi-Hubbard ladders in the Heisenberg regime of strong interactions. A natural implementation involves ladders with antiferromagnetic leg coupling $J_\parallel$ and ferromagnetic rung coupling $J_\perp$, thus forming spin-1 objects on the rungs of the ladder, which are connected to a chain. Another possibility, which is conceptually closer to the singlet bonds of the AKLT model, is antiferromagnetic ladders. In the strong rung coupling regime, these form strong singlet bonds on the rungs, which correspond to the singlet bonds

of the AKLT model. The spin-1 objects consequently have to be formed diagonally, containing fermions of different rungs. The idea is illustrated in Fig. 2.15. We note that the ladder system does not exactly map onto a spin-1 chain, since not all unit cells have a combined spin of one, but a finite fraction contains spin-0. However, the two systems can be adiabatically connected by including an additional diagonal coupling term [101, 156]. This adiabatic connection starts from a system dominated by a strong ferromagnetic diagonal coupling which is equivalent to the spin-1 chain. Including a finite $J_\perp$ and reducing the diagonal coupling to zero constitutes a symmetry-preserving transformation that does not close the gap [101]. Therefore, not only the spin-1 chain but also the spin-1/2 two leg ladder with diagonal unit cell realizes the Haldane phase for all finite couplings $J_\perp / J_\parallel$. The two systems thus share the same universal SPT features, despite the finite singlet fraction in the unit cell for the ladder system.

The Hamiltonian of the spin-1/2 ladder in the undoped Heisenberg regime is

$$\hat{\mathcal{H}} = J_\parallel \sum_{\substack{x \\ y=A,B}} \hat{\mathbf{S}}_{x,y} \cdot \hat{\mathbf{S}}_{x+1,y} + J_\perp \sum_x \hat{\mathbf{S}}_{x,A} \cdot \hat{\mathbf{S}}_{x,B} \qquad (2.10)$$

with positive leg and rung couplings, $J_{\parallel,\perp}$ and the spin-1/2 operators $\hat{\mathbf{S}}_{x,y}$ at site (x,y) with A,B denoting the two legs of the ladder. This Hamiltonian has a spin gap in the bulk of the system, which, in the strong rung coupling limit $J_\perp \gg J_\parallel$, corresponds to the energy cost $J_\perp$ of exciting a singlet along the rung to a triplet state. However, a finite spin gap persists for all finite couplings $J_\perp$, even in the strong leg coupling regime. We define a unit cell k as containing site $(k+1, A)$ and site (k, B). The spin in the kth unit cell follows as

$$\hat{\mathbf{S}}_k = \hat{\mathbf{S}}_{k+1,A} + \hat{\mathbf{S}}_{k,B}, \qquad (2.11)$$

where the indices (A,B) indicate the two spin-1/2s in the same unit cell k. $\hat{\mathbf{S}}_k$ is thus an integer spin.

We note that the definition of the diagonal unit cell is crucial for the system to connect to a spin-1 chain because the phase is dependent on the objects considered. The system consisting of our diagonal unit cells realizes the Haldane phase. Furthermore, the edge termination of the system only features fractional edge modes, if the system is terminated in accordance with the unit cell definition. If a unit cell is cut in half at the boundary, no edge states appear. This holds for the ladder system as well as for the AKLT system. In comparison, Fig. 2.16 shows a spin-1/2 ladder with vertical unit cells, each containing a full rung bond. Despite the very similar construction of the system, the vertical unit cell system is not in an SPT phase, but in a trivial phase, i.e. there is no symmetry-preserving transformation[1] between this ladder, and the one in Fig. 2.15 [192, 193]. The trivial ladder also does not show any edge states, when the boundaries are chosen in accordance with the unit cell.

The differences between the trivial and the SPT system are also visible in their spectrum. Fig. 2.17 shows the energy levels of both systems. Depending on the total

---

[1]At least within the Heisenberg model, where charge fluctuations are forbidden [191]
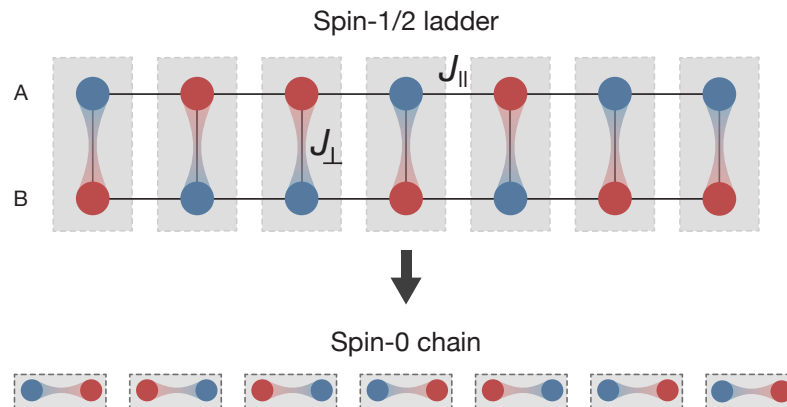
Figure 2.16: Mapping a ladder on a spin-0 chain. A ladder system can be mapped on a spin-0 chain by choosing vertical unit cells. This approach is complementary to the diagonal unit cells discussed earlier. We note that for finite $J_\parallel$, the mapping is not exact, because the unit cells contain a finite fraction of triplets. The systems are only adiabatically connected, as it is symbolized by the arrow.
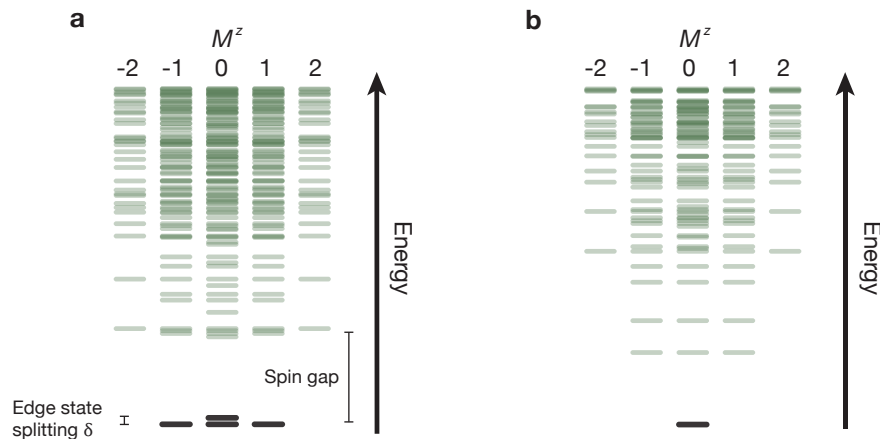
Figure 2.17: Spectrum of ladders with different edge termination. The figure shows the energy levels of the ladder system with diagonal unit cells (**a**) and vertical unit cells (**b**) for a system length of $L = 7$ unit cells. **a,** The four ground states of the Haldane chain. The small energy splitting between them is a finite size effect, deriving from the finite overlap of the edge modes due to the finite localization length. The lowest states correspond to three triplets and the slightly higher state to the singlet state of the two edge spins. The spectrum in **b** shows one single ground state, which is the state containing only rung singlets.

magnetization

$$M^z = \sum_{x,y} S^z_{x,y} \, , \tag{2.12}$$

where $S^z_{x,y}$ is the spin in z-direction on site (x, y). While both systems show the spin gap of the bulk, the SPT system shows four ground states and the trivial system shows only one ground state. The four ground states of the SPT system show a slight energy splitting, which arises from the overlap of the two edge modes in the bulk. It thus depends on the localization length ξ of the edge states and the system size L as

$$|\delta| \propto e^{-L/\xi} \, , \tag{2.13}$$

meaning the edge state splitting disappears in the thermodynamic limit. It can be seen from the spectrum that the ground states either have total magnetization $|M^z| = 1$ or $M^z = 0$. They correspond to three triplet states and one singlet state of the edge modes.

2.6.3   Non-local string operators

The Haldane phase can be identified by detecting the already mentioned symmetry fractionalization from $SO(3)$ to $SU(2)$ symmetry. This can be detected not only at the edge of the system, but also within the bulk using string order parameters [194, 195]

$$g_{\mathcal{O},U}(d) = \left\langle \hat{\mathcal{O}}_k \left(\prod_{l=k+1}^{k+d-1} \hat{U}_l \right) \hat{\mathcal{O}}_{k+d} \right\rangle_k \tag{2.14}$$

with an on-site symmetry $\hat{U}_l$, where l denotes the unit cell, and endpoint operator $\hat{\mathcal{O}}_k$. $\langle \rangle_k$ denotes the expectation value averaged over all unit cell positions k and d denotes the string distance. This correlator probes the transformation behavior of the bulk under a symmetry $\hat{U}_l$. An example, and in fact the symmetry that we will be probing, is the π spin rotation around the z-axis

$$\hat{R}^z_l \equiv \exp\left(i\pi\hat{S}^z_l\right) \tag{2.15}$$

The string-order correlator with $\hat{U}_l = R^z_l$ can only be non-zero if the phase is symmetric under R^z_l. A finite string order is however not able to distinguish different symmetric phases. The more surprising property is thus a vanishing string-order correlator a symmetry under $\hat{U}_l$ [2]. For the correlator to vanish the endpoint operator $\hat{\mathcal{O}}_k$ is relevant, whose symmetry acts as a selection rule for string order.

For the Haldane phase, the string operator for $\hat{U}_l = R^z_l$ has long-range order, if the endpoint operator $\hat{\mathcal{O}}_k$ is odd under spin flips R^x around the x-axis. This is the case for the string order parameter $g_{S^z,R^z}(d)$ with endpoint operator $\hat{\mathcal{O}}_k = \hat{S}^z_k$ [194]. The string operator vanishes if the endpoint operator is even under R^x, because U^z_l is odd under

---

[2]Note, however, that the string order can effectively vanish at certain points by coincidence. One string order is thus not sufficient, to distinguish different phases. It needs two correlators with different endpoint operators to reliably distinguish two phases [195]

R^x. This condition can be satisfied $g_{\mathbb{1},R^z}(d)$, where $\hat{\mathcal{O}}_k = \mathbb{1}$. This operator reveals the symmetry fractionalization in the Haldane phase. The opposite behavior is found in the topologically trivial phase, where $g_{S^z,R^z}(d)$ vanishes and $g_{\mathbb{1},R^z}(d)$ is non-zero even for $d \gg 1$. One can thus identify the Haldane phase, and distinguish it from the trivial phase, by comparing both string correlators. (for details and the derivation of the string order parameters, see [195]).

We can interpret the long-range order in $g_{S^z,R^z}(d)$ as the hidden antiferromagnetic order discussed earlier, which appears when the unit cells containing spin $m_k = 0$ are removed from the chain. The operator R_l^z equals one, if it is applied to such a unit cell containing $\hat{S}_k^z = 0$, which is equal to removing it from the product $\left(\prod_{l=k+1}^{k+d-1} \hat{R}_l^z \right)$.

Thus only unit cells containing $\hat{S}_k^z = \pm 1$ contribute to the bulk of the string operator. Due to $R_l^z = -1$ for $\hat{S}_k^z = \pm 1$, the string switches sign at every unit cell containing $\hat{S}_k^z = \pm 1$. For a hidden AFM ordered chain it thus holds that $g_{S^z,R^z}(d) < 0$ for all distances $d > 0$. Note that the string operator is zero if the endpoints contain a unit cell with spin $m_k = 0$.

The Experimental Setup

In this chapter the experimental apparatus is introduced. We will discuss the preparation routine with which we generate cold atomic clouds and how we employ optical lattices to simulate the Fermi-Hubbard model. We describe the optical potential shaping using a digital micromirror device (DMD), which has been implemented into the apparatus within the course of this PhD thesis. Furthermore, the protocol for spin resolution and simultaneous readout of two atomic planes is introduced. Finally, the automated evaluation and feedback algorithms are presented, which allow running the apparatus in a less supervised mode of operation.

3.1 Preparation of a cold atomic sample

Our experimental sequence takes about 20 s to produce a single experimental snapshot. About 80% of this time is dedicated to the production of a cold cloud of lithium atoms, a step which has to be repeated for every snapshot. The main technological tools in this step are laser trapping and cooling, as well as evaporative cooling. The main experimental apparatus has been built by a previous generation of PhD students [127, 196, 197].

Lithium

The experimental setup uses Lithium-6, a fermionic alkali metal isotope. Lithium is suitable and commonly used for cold atom experiments [45, 198–201] because it can be laser cooled at a commercially available wavelength and with its single valence electron has a relatively simple level structure. With reachable temperatures of $T/T_F = 0.05$ in bulk systems [202], lithium can currently reach colder samples than other fermionic species and is thus especially attractive for quantum simulation.
The level structure of ^{6}Li is shown in Fig. 3.1a. The splitting between the $F = 1/2$ and $F = 3/2$ states of the ground state $2S_{1/2}$ is about 228 MHz, small enough to be bridged using acousto-optic modulators (AOMs). The D_1 and D_2 transitions have a wavelength of about 671 nm, with a fine-structure splitting of about 10 GHz. The corresponding excited states $2P_{1/2}$ and $2P_{3/2}$ have a natural linewidth of $\Gamma = 2\pi \cdot 5.87$ MHz [203]. The next higher transition, reaching the $3P_{1/2}$ and $3P_{3/2}$ states, is already in the ultraviolet (UV) regime with 323 nm. The transition has a width of $\Gamma = 2\pi \cdot 159$ kHz, while the natural linewidth of the 3P states is broadened to $\Gamma = 2\pi \cdot 754$ kHz, due to an additional decay channel [204].
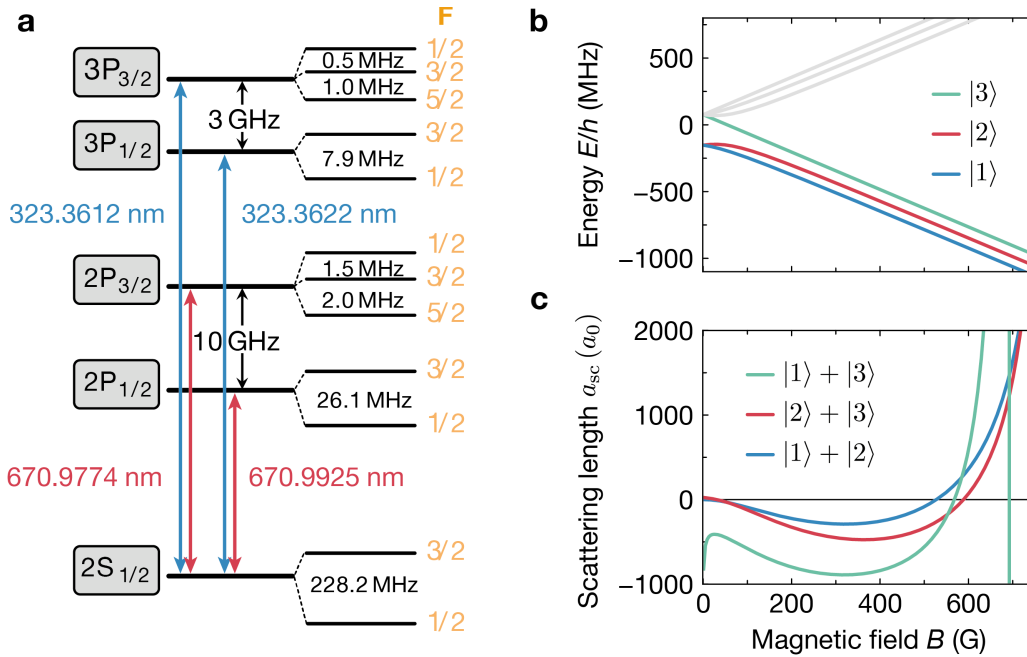
Figure 3.1: Properties of Lithium. a, The level structure of ^{6}Li is illustrated. The D_1 and D_2 transitions have a wavelength of about 671 nm, while the next higher transition has a wavelength of 323 nm. **b**, Hyperfine splitting of the ground state $2S_{1/2}$ of ^{6}Li in a magnetic field. The three lowest states $|1\rangle$, $|2\rangle$, and $|3\rangle$, which can form collisionally stable mixtures, are marked in color. **c**, Scattering lengths A_{SC} between the three lowest hyperfine states versus magnetic field, given in units of the Bohr radius a_B. All three combinations of states possess a broad Feshbach resonance. The figure is adopted from [121].

Under the influence of a magnetic field, the hyperfine levels of lithium split due to the Zeeman effect (see Fig. 3.1b). In the experiment, we work with the lowest two hyperfine states $F = 1/2, m_F = \pm 1/2$, here labeled as states $|1\rangle$ and $|2\rangle$. At low fields these two states experience an opposite splitting, meaning that a field gradient can exert a force in opposite directions. We make use of this force for spin resolution (see below). At few tens of Gauss, ^{6}Li enters the Paschen-Back regime, where the nuclear spin decouples from the electronic angular momentum. In this regime the two lowest hyperfine states are shifted in the same direction, such that magnetic field gradients affect both states equally, which we use for our magnetic evaporation.

At temperatures below quantum degeneracy, the collisions of different hyperfine states are dominated by s-wave scattering, while same-spin fermions do not interact. The strength of these contact interactions can effectively be described by the scattering length a_{SC}. In lithium, the interactions can be tuned using a broad Feshbach resonance [202, 205], which is shown in Fig. 3.1c. By changing the magnetic field, the scattering length between the spin states $|1\rangle$ and $|2\rangle$ can be tuned from negative to strongly positive. The scattering length diverges at around 830 G. At zero field the scattering length vanishes.

Trapping and laser cooling of lithium atoms

In our setup, lithium is heated and effuses out of a steel chamber, which serves as an atomic source. Inside an ultra-high vacuum setup, the fast lithium atoms are slowed down in a Zeeman slower and subsequently captured in a magneto-optical trap (MOT) on the D2 transition, which achieves temperatures of a few hundreds of µK. In a second laser cooling step, the atomic sample is cooled to $\sim 60\,\mu$K in a UV MOT using the narrow $2S_{1/2}$ to $3P_{3/2}$ transition. For details on the MOT and UV laser setup see [196]. Repumping after the UV MOT ensures a balanced mixture of the states $|1\rangle$ and $|2\rangle$.

The atoms are transferred from the UV MOT into a 100 W dipole trap originating from a 1070 nm laser, a 'magic' wavelength with respect to the UV transition. This means the states $2S_{1/2}$ and $3P_{3/2}$ have equal polarizability at this wavelength [206]. The cooling on the UV transition is thus not affected by the presence of the optical trap. After the UV light is shut off, the atoms are transferred into a less deep but more tightly focused dipole trap via optical evaporation. In the next step, the atomic cloud needs to be moved into a glass cell. To achieve this transport, the focus of the dipole trap is moved by about 30 cm by moving an air-bearing linear translation stage on which the optics are mounted. The atoms follow the focus of the trap. The full assembly of the vacuum setup can be found in [196].

In the glass cell

The main physics takes place in a glass cell, which offers increased optical access compared to a metal chamber. When the atoms arrive in the horizontally transported dipole trap, they are slowly loaded into a vertically crossed dipole trap via optical evaporation. In the next step, we want to load a single plane of a vertical lattice. Single plane loading is a challenge, as optical dipole traps have typical sizes much bigger than the lattice spacing. In our experiment the vertical lattice spacing is comparably large at 6 µm. To transfer the atoms into one vertical plane, we shape a strongly elliptic trap that acts as a light sheet. The light sheet is projected from the side of the glass cell through a high-NA lens of focal length $f = 40$ mm. We use laser light at a wavelength of $\lambda = 780$ nm and achieve a gaussian waist of 1.7 µm in the vertical direction, which strongly confines the atoms. From this trap we can transfer the atoms into a single plane of our lattice.

Vertical superlattice

In the vertical direction, the apparatus is equipped with a lattice of $a_z^s = 3\,\mu$m spacing and a superlattice of $a_z^l = 6\,\mu$m spacing. The bichromatic superlattice setup can be seen in Fig. 3.2. Two laser beams with commensurate wavelengths (532 nm and 1064 nm) are overlapped and sent into a temperature-stabilized low vacuum box, where the path is split into two arms. The two arms recombine under an angle $\alpha = 10°$ at the position of the atoms. The path length of the two arms is however not equal. Instead, one arm is equipped with a delay line of $\Delta L = 56$ cm, which enables adjusting the relative phase between the two lattices by shifting one of the two colors

a

low vacuum box

z

glass
cell

mirror

outcoupling

delay
line

dichroic

50:50 BS

b

OD
(arb)

$6\,\mu$m

$3\,\mu$m

z

y
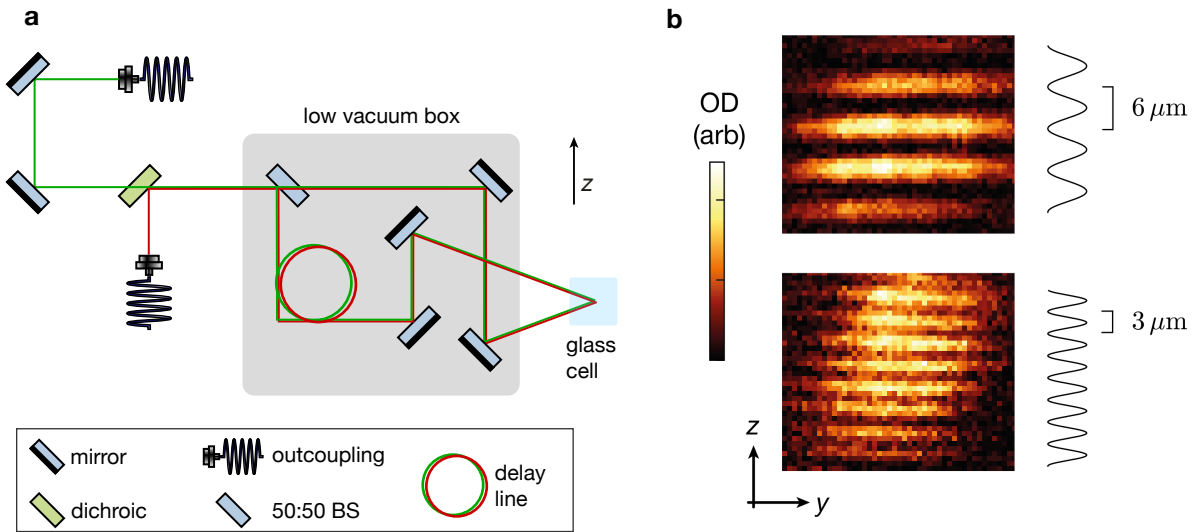
Figure 3.2: Bichromatic vertical superlattice. a, Setup of the bichromatic vertical
superlattice. Light of $\lambda = 532$ nm and light of $\lambda = 1064$ nm are overlapped and sent to
an aluminum box of low vacuum, where they are split at a 50:50 beamsplitter (BS). The
two arms interfere in the glass cell, creating a lattice and superlattice. **b**, Absorption
images of the atoms in the superlattice (upper image) with a spacing of 6 μm between
neighboring planes and of the atoms in the short lattice (lower image) with a spacing
of 3 μm. In these images, the lattices are loaded directly from the crossed dipole trap,
without the confining light sheet. Thus several planes are populated. OD optical
density. **b** is taken from [121].

in frequency. This bichromatic setup allows for high relative phase stability. The
vacuum box further stabilizes the optical path length, by minimizing pressure and
humidity fluctuations. Mutual phase stability of the two light sources is ensured by
using a common laser source. A 1064 nm Mephisto MOPA provides laser light for the
superlattice, while also providing seed light for a 1064 nm fiber amplifier (Azurlight
Systems), which is subsequently frequency doubled and thus provides the light for
the short lattice. Detailed descriptions of the setup and stability estimations can be
found in [121, 207].

Magnetic evaporation

We load the atoms into a single plane of the superlattice with a depth of $100\,E_{\mathrm{R}}^{\mathrm{l}}$. Once
a single plane is populated, we adiabatically turn on the short lattice to $50\,E_{\mathrm{R}}^{\mathrm{s}}$. We set
the relative phase of the lattice such that we transfer all atoms into one lattice plane.
We then use magnetic evaporation to further cool down the atoms [208]. Using a
magnetic field offset of about 600 G, we tune the scattering length to $350\,a_{\mathrm{B}}$, with a_{B}
being the Bohr radius. At this field we find the atoms in the Paschen-Back regime.
Over a time span of 5 s we ramp up a magnetic field gradient along the y-direction,
which effectively lowers the potential barrier of the trap and equally spills both spin
species. It thus preserves the balance of the spin mixture. Our evaporation reaches

temperatures of about $T/T_\mathrm{F} \approx 0.1$ [121].

3.2 Shaping and imaging a Fermi-Hubbard system

To simulate the Fermi-Hubbard model, we use a square optical lattice of spacings $a_\mathrm{x} = 1.18\,\mu\mathrm{m}$ and $a_\mathrm{y} = 1.15\,\mu\mathrm{m}$. The optical lattices are generated by two parallel pairs of 1064 nm laser beams, which are focused through our high-NA objective and form a standing wave in the focus, as it is described e.g. in [197]. After the magnetic evaporation, the xy-lattice is ramped up within 100 ms to typical depths between $5\,E_\mathrm{R}$ and $12\,E_\mathrm{R}$. Simultaneously, the scattering length is tuned to its final value, typically between $500\,a_\mathrm{B}$ and $1500\,a_\mathrm{B}$. We usually work in the regime of $8 \le U/t \le 15$.

3.2.1 Site-resolved potential shaping

The optical lattice generates a square lattice potential with harmonic confinement and local potential inhomogeneities due to fringes in the laser beams. The fringes largely derive from the lattice setup which passes through the objective. This images small defects like dust and scratches on mirrors onto the atomic plane. We use a programmable light pattern to add a site-resolved repulsive potential on top of the lattice grid. This allows us to compensate for the harmonic potential and fringes and create a comparably flat system. We furthermore use this arbitrary potential to shape ladder systems.

To generate the programmable optical potential we use a digital micromirror device (DMD), similar as in [209]. A DMD is a two-dimensional array of small mirrors that can be flipped individually to reflect an incoming beam. In our setup, we use a DMD from Vialux (DLP V-7000 VIS) with specifications given in Table 3.1.

DMD parameters	
DMD resolution	1024 x 768
Pixel pitch	13.6 μm
Pixel per lattice site	$\sim$ 16 x 16
Wavelength used	650 nm
Refresh rate	disabled

Table 3.1: Specifications of the DMD setup. This includes parameters specific to the DMD, as well as parameters given by our optical setup. Pixel pitch is the distance between the centers of neighboring pixels. Refresh rate is the regular refreshing of a static image, which can be disabled in the software.

We illuminate this mirror array with incoherent light at a center wavelength of 650 nm, which is blue detuned from the lithium transitions at 671 nm and thus creates a repulsive potential. The light source is a superluminescent diode (SLED) from Exalos (EXS0650-006-10-0B00030) with a linewidth of 6 nm and up to 10 mW output power. We amplify the light using TA chips (EYP-TPA-0650-00250). Since TA chips at such
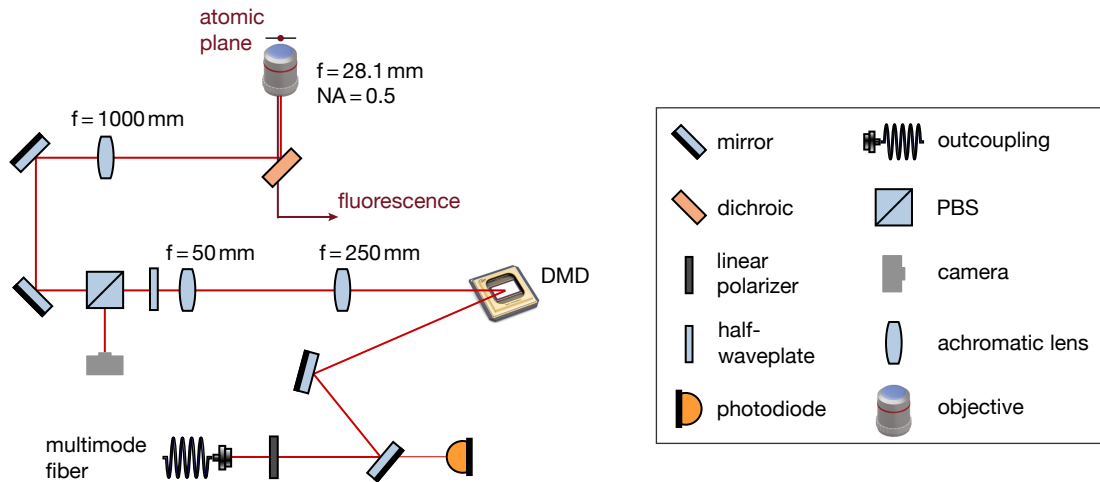
Figure 3.3: DMD setup. Incoherent laser light at 650nm, which is coupled out of a multimode fiber, illuminates the DMD pattern. The reflected pattern passes several lenses for beam shaping. Close to the image plane after the first pair of lenses, a beam profiling camera monitors the diffracted pattern using a small fraction of the total intensity reflected at a polarizing beamsplitter cube (PBS). The beam is overlapped with the fluorescence imaging path and is imaged onto the atomic plane. The light intensity is stabilized by sending a small fraction to a photodiode.

short wavelengths decrease in output power within few weeks, and the initial power from the diode is below the optimal seed power, we require three TA amplification stages in row to achieve a stable power level. We then filter the amplified spontaneous emission, which can cause heating in the atomic system when it is close to the atomic transition of 671 nm. The temporally incoherent light is then coupled into a multimode fiber, where mode scrambling generates spatial incoherence out of the temporally incoherent light [210]. Having both spatially and temporally incoherent light greatly reduces the amount of light speckles when projecting the DMD pattern onto the atomic system.

A sketch of the optical setup which illuminates the DMD and images the pattern onto the atoms is shown in Fig. 3.3. We monitor the projected light pattern using a beam profiling camera in an imaging plane which lies between the DMD surface and the imaging plane on the atoms. The DMD beam path is overlapped on a dichroic (SEM-FF662-FDi002-t3-50.8-D) with the fluorescence path that we use to image the occupation in the optical lattice. The dichroic has a high surface flatness with a reflected wavefront error of $\lambda/5$. This minimizes the astigmatism introduced to the beam focus. Note that the objective has a chromatic shift for 650 nm, as compared to the focus position for the 671 nm light of the fluorescence signal. We compensate for this by adjusting the position of the $f = 1000$ mm lens correspondingly.

For a given total laser intensity, each pixel of the DMD only allows for binary amplitude control by flipping the mirror position. This means a single pixel does not allow for a continuous grayscale. However, diffraction-limited imaging leads to coarse graining of the pattern. The images of several pixels overlap on the same lattice site.
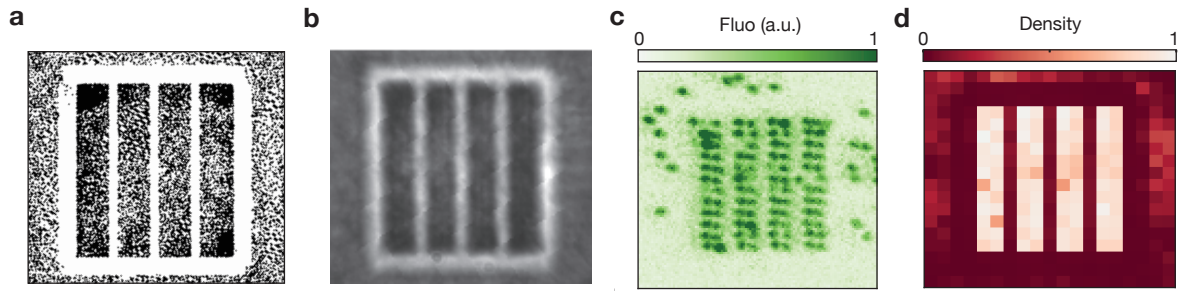
Figure 3.4: DMD pattern and projected potential. a, Programmed micromirror pattern using error diffusion to reach an effective grayscale. **b**, Light pattern reflected from the DMD, which was programmed with the pattern of **a**. **c**, Snapshot of the atoms in the optical lattice with the additional potential created by the light pattern. **d**, Average density calculated from 450 shots.

Each lattice site is thus addressed by about 250 individual pixels whose point-spread functions partially overlap. A given amplitude on a lattice site is translated to a distribution of switched mirrors using error diffusion [211], as it is explained for example in [212].

Fig. 3.4a shows such a programmed DMD pattern, while Fig. 3.4b shows the light pattern that is projected. Fig. 3.4c and d show an example shot and the corresponding average density for this pattern. The pattern creates four independent ladder systems that are separated by walls. A broad Gaussian-shaped pattern is added on top of the ladders to compensate for the harmonic confinement of the optical lattice. The average density hence does not show the Gaussian confinement. The low density on the barriers indicate a clean separation between the ladders. No density feedback (see below in section 3.3) was applied to the pattern to flatten the potential.

3.2.2 Spin resolution

The physics of the Fermi-Hubbard model, which we want to study with our machine, is marked by a competition between spin and charge degrees of freedom. To extract information about this competition, it is advantageous to have a detection that allows to read out the full information of spin and charge for every snapshot. For undoped systems in the Mott insulating regime, this can be done by a charge-only detection, if one of the two spin states is removed by a state dependent pushout before detection [213]. An empty site in the detection can then be assigned the removed spin state with high probability. At finite doping however, other detection schemes are needed as it becomes impossible to distinguish dopants (holes) from the removed spin species. In the course of this PhD thesis, our machine was changed from an in-plane spin resolution [47], to an out-of-plane spin resolution using the vertical superlattice introduced in Fig. 3.2.

After preparing the desired quantum state in the optical lattice we freeze the occupation distribution by ramping the physics lattices to $43\,E_{\mathrm{R}}^{xy}$. We then transfer the atoms from a single plane of the z-lattice to a single plane of the z-superlattice. Then, a Stern-
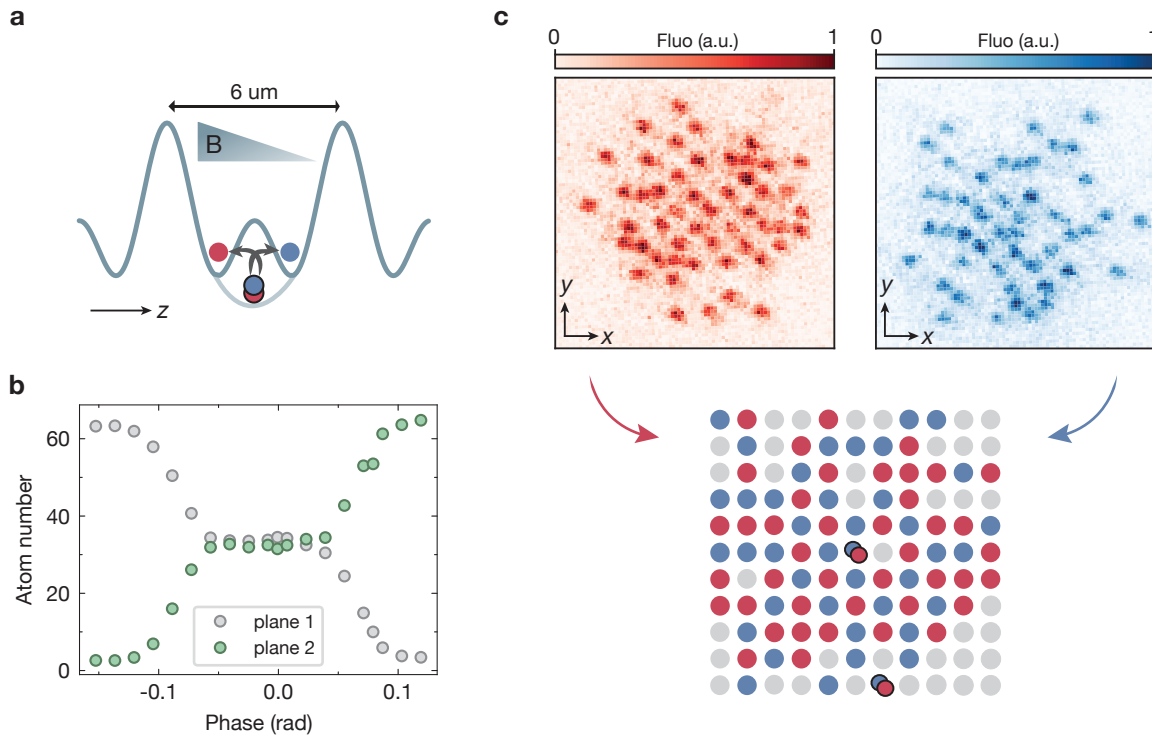
Figure 3.5: Spin splitting. a, Illustration of the Stern-Gerlach splitting in $z-$direction. The magnetic field gradient leads to different potentials for the two spin species. While for one species the ground state is localized in the left well, it is in the right well for the other spin. They are thus adiabatically transferred into opposite wells. **b**, Population of the two wells (planes) depending on the relative phase between lattice and superlattice. Phase zero denotes the symmetric configuration. The central plateau shows the region where the gradient is larger than the phase offset. Here, the occupation is splitted according to their spin. **c**, Example shots of the two spin species and reconstructed spin- and charge-resolved occupation of the original atomic plane. The imaging technique is described in the following part.

Gerlach separation displaces the two spin states vertically, by ramping up a magnetic field gradient in z-direction. For this, we stay in the regime of low magnetic field of few G, for which the two spin states experience an opposite force. Additional to the z-superlattice, we adiabatically turn back on the z-lattice in a symmetric double-well configuration, such that the two spin states are transferred into opposite wells (see Fig. 3.5a). To measure the sensitivity on the symmetric phase, we perform this spin splitting sequence at different relative phases between the lattice and superlattice. If the potential shift given by the gradient is stronger than the potential offset caused by the phase, the spin species are transferred into opposite wells. However, if the phase offset becomes too large, all atoms, independent of their spin, are transferred into the same well. The plateau in Fig. 3.5b shows that for asymmetric phases less than 0.5 rad from the symmetric phase, our splitting procedure reliably splits the cloud according to the spin. The measurement is taken by imaging and reconstructing the occupation in the two planes independently (see below for details on the site-resolved imaging).
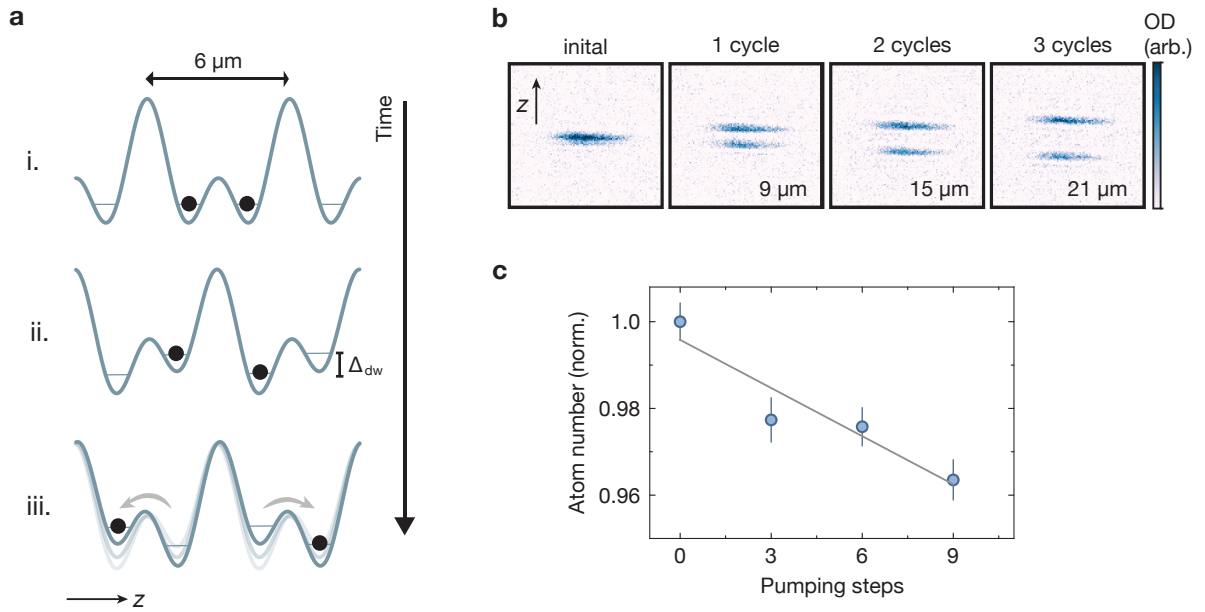
Figure 3.6: Geometric pumping scheme. **a**, Time-modulation of our superlattice phase and corresponding transport of the atoms. i. Two atoms initially inhabit opposite wells of the same double well but are moved into different double wells (ii.) by shifting the superlattice phase at deep z-lattice potential. iii. An adiabatic phase sweep transfers the atoms to the opposite well within their respective double well, which leaves the atoms 6 µm further separated than the initial position. **b**, Absorption images of the pumped planes taken from a side view. The first image shows two planes in a double well configuration, the following images show the plane distance after each pumping step. **c**, Pumping fidelity. The atom number of a single pumped plane is plotted versus pumping steps. To increase the amount of pumping steps, we reverse the pumping direction after three steps. The atom number is evaluated from fluorescence images. A linear fit suggests a pumping fidelity of 98.9% for every three pumping steps.

Fig. 3.5c shows an example image of a spin-splitted cloud and the reconstructed spin-resolved occupation of the two-dimensional atomic system.

In order to image the two planes, they first need to be further separated in the vertical direction. For this, we apply a charge pumping sequence similar to a topological Thouless pump [178, 214, 215], by modulating our superlattice phase and amplitudes in time. A single pumping step of our scheme is illustrated in Fig. 3.6a. The spin splitting leaves us with a symmetric double well configuration and a finite population in both wells (step i. in the figure). We shift the lattice phase, while z-lattice and z-superlattice are at their maximum depth. When we subsequently reduce the z-lattice depth to $11\,E_R$, we initialize the atoms in two distinct bands of distinct double wells with a tilt Δ_{dw} (step ii.). One population is initialized in the ground band of a double well, while the other population inhabits the excited band of the neighboring double well. These two bands have opposite Chern numbers [178, 214]. In the next step, we adiabatically sweep the double well tilt from Δ_{dw} to $-\Delta_{dw}$ (step iii.). The different

Chern numbers of the bands lead to transport in opposite directions upon this phase sweep. We then increase the z-lattice again to maximum depth. We repeat this geometric pumping sequence to increase the distance between the two spin layers far beyond the depth of focus of our imaging system. A single pumping cycle separates the atoms by $a_z^l = 6\,\mu m$, giving a total of 21 μm after 3 steps together with the initial Stern-Gerlach separation of 3 μm.

Our pumping sequence is not identical to a topological Thouless pump. The difference lies in the repetition of the initial non-adiabatic phase ramp. Since our setup only allows for a phase range of less than 4π, we can not continuously, adiabatically move the atoms while keeping them in the same band. Instead, we have to repeatedly reset the tilted double well configuration and do not complete a closed circle in phase space. Nevertheless, we can continuously separate the two planes. This is demonstrated in Fig. 3.6b, which shows absorption images of the populated planes in side view.

We measure the pumping fidelity by preparing a single layer of atoms and pumping it with our sequence. After three steps, we take fluorescence images and compare the number of atoms to the atom number in the original plane. To increase the sensitivity of our method, we repeat the measurement with six and nine pumping steps. In order to not leave the central area of our lattice beams, we reverse the pumping direction once after three steps. We achieve a pumping fidelity of 99.6% per pumping step, or 98.9% for three pumping steps (see Fig. 3.6c).

3.2.3 Bilayer imaging

In order to take spin-resolved snapshots, we need to take fluorescence pictures of both spin species, which occupy planes of our lattice in a distance of 21 μm. Previously, we achieved this by taking two subsequent fluorescence images and moving the high-NA objective by the required distance between the two images. However, this approach not only cost us 1 s per experimental cycle to move the objective, but it also caused random shifts between the two planes on camera due to unpredictable movements of the objective in xy-direction at every focus shift. As a result, the two planes had to be matched separately in every shot. The matching algorithm was based on the assumption that the original plane displays a Mott insulator with low doublon number (for details see [216]). This method however fails for high doping or small systems.

To avoid these problems, we have introduced simultaneous imaging of both planes (see Fig. 3.7a). The fluorescence light captured through the objective is split into two paths, with one of the paths containing an additional telescope. the paths are then recombined and sent onto the same EMCCD camera with a small offset in position, such that they illuminate different areas of the camera chip. The additional telescope has one lens on a motorized stage (Newport MFA-CC), which allows to adjust the focus position from within the experimental sequence. This way the two spots on the camera correspond to different foci in the atomic system. They are set to be 21 μm apart from each other by adjusting the motorized telescope. The focal plane of the objective is estimated to sit between the imaged planes, close to the original atomic plane.
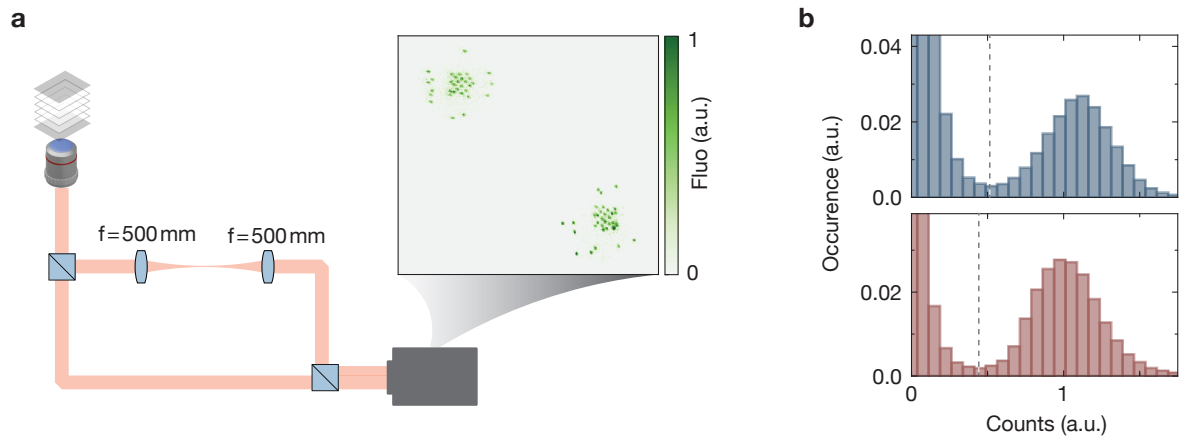
Figure 3.7: Bilayer imaging. a, Bilayer imaging scheme. The unpolarized fluorescence signal collected from the high-NA objective is split at a polarizing beamsplitter cube. One path passes through an additional telescope consisting of achromatic lenses, one of them mounted on a motorized translation stage. The paths are recombined with a small offset and captured on different areas on the camera chip, as seen in the example snapshot. The snapshot shows a spin-split cloud with one spin species on the upper left part of the snapshot and the other species on the lower right part. The surrounding area of the camera field of view was cut out. **b**, shows the histograms of counts per reconstructed lattice site for a data set of 1300 spin-split images. Both the first imaging path (blue) and the second imaging path (red), which contains the telescope, allow for a clear identification of atoms.

The example shot in Fig. 3.7a shows a spin-resolved box potential with few atoms outside of the box potential. The antiferromagnetic correlations are visible from the checkerboard pattern inside the box area. Fig. 3.7b shows the reconstruction histograms for both paths. The pixel counts are summed up in each lattice site and an occupation is assigned to the site. The histograms show a clear distinction between occupied and non-occupied sites. Due to the spin splitting, doublons are separated into different planes. In reconstructing the occupation from the fluorescence signal, we thus only need to distinguish zero from one atom. The similarity of the histograms shows that the additional telescope does not significantly influence the imaging quality.We find a PSF with 2d profiles of size $\sigma_1^s = 315\,\text{nm}$ and $\sigma_1^l = 432\,\text{nm}$ for the first path, and $\sigma_2^s = 347\,\text{nm}$ and $\sigma_2^l = 415\,nm$ for the second path, where superscripts s (l) denote the short (long) axis of the PSF.

3.3 Automatic evaluation and feedback procedure

Quantum gas microscopes require a lot of maintenance time and in operation the machines are often not stable enough for unsupervised data taking. In our lab, we have introduced several improvements like automatization, monitoring and feedback procedures to increase the efficiency and stability of the lab. In the following, I will mention a few key improvements.

Running motorized mounts from the sequence control

Motorized mirror mounts allow for precise beam alignment without physically touching the experiment. This makes alignment procedures more efficient and avoids thermal drifts from removing the protective doors around the optical table. Motorized flip mounts can be used to insert optical elements into the beam path, which we use for example to switch between fluorescence imaging and vertical absorption imaging. We have recently implemented the addressing of these mounts into the experimental control system. They can now be operated and scanned from the experimental sequence. This allows for remote alignment scans of most of our setups, for example for the optical lattices. This upgrade paves the way towards automatic self-alignment of the apparatus.

Z-lattice absolute phase feedback

Drifts of the z-superlattice absolute phase are detrimental to single-plane loading and the imaging focus. Without active feedback, we observe phase shifts on the order of π on timescales of 20 to 30 minutes. The largest contribution to phase instabilities comes from thermal expansions of the aluminum plate on which the optics of the lattice setup are mounted. We note that this does not significantly affect the relative phase stability. To counteract these drifts, we stabilize the absolute plane position. Every one out of seven experimental runs, we take an absorption image of the z-lattice from the side, similar to Fig. 3.6b. A continuously running script awaits these pictures, fits the plane position, and compares it to a fixed reference position. The error is converted to an analog voltage output (using an Adafruit Feather M0), which is used to control the temperature and thus wavelength of our 1064 nm laser seed (Mephisto MOPA). The absolute phase stabilization relies on the phase difference accumulated in the delay line and causes a commensurate shift for the lattice and the superlattice.

Occupation reconstruction

The occupation of the two imaged planes is continuously evaluated. This enables monitoring of the total atom number as well as of the lattice phase. Monitoring these quantities allows us to spot and solve instabilities as they occur. Due to our spin-splitting technique, we also need to ensure the correct matching of the two imaged planes. Continuous drifts can eventually lead to a wrong combination of the two spin planes. A wrong match manifests itself in a sudden jump of the center pixel in one of the planes. We continuously run a matching algorithm to detect such jumps and shift the matching parameters accordingly. This procedure assures the correct spin reconstruction for continuous data sets. The experimentalist operating the machine only needs to verify the correct matching of the first snapshot.

DMD shift

To shape ladder systems with our DMD, we need to align the DMD potential to the lattice grid with high precision. To keep the ladder positions aligned with the correct

lattice sites, we need to compensate for (a) drifts in the lattice position and (b) drifts in the DMD potential position. We compensate for (a) using the lattice phase monitoring mentioned above. The lattice phase is translated to an absolute shift of the pattern on the DMD chip. The compensation of (b) requires another observable: a feedback script evaluates the ladder occupation and calculates the imbalance between the two legs. A drift in the DMD pattern can be detected as an occupation imbalance, because parts of the potential barrier will affect one side of the ladder. If the average imbalance of the last 20 shots exceeds 5%, a shift is applied to the DMD pattern. The averaging of 20 shots is done to reduce the influence of shot-to-shot fluctuations, but the optimal number of shots depends on the system stability and can be adjusted manually in the script.

Monitoring

We use the open-source monitoring system Grafana [217] to keep track of quantities like the lab temperature and magnetic field, but also observables of our experimental system like the total atom number and lattice phase. This system allows us to detect and counteract problems before losing valuable measurement time. Atom number drifts, for example, can trigger warning messages that reach us immediately. Time traces of these observables helped us for example find the correlation between lab temperature and z-superlattice phase. The improvements mentioned in this section together have led to a more efficient operation of the experiment that requires less active attention.

Magnetically Mediated Hole Pairing

In this chapter, we present the main result of the thesis, which is the microscopic observation of hole pairing. The binding of such charge carriers is a key process in the emergence of superconductivity, and a complete understanding of its origins in unconventional superconductors is still lacking. Here, hole pairing is achieved experimentally by realizing mixed-dimensional ladder systems, which we introduce in the first part of the chapter. We then present its experimental implementation using our Fermi-gas microscope. We discuss the hole correlation, which reveals the existence of a bound state and contrast it to the repulsion of holes in the standard (not mixed-dimensional) ladder configuration. Furthermore, the magnetic environment that leads to the hole binding is characterized. Finally, we show that the presence of several pairs leads to repulsive interaction of pairs. The numerical results presented in this chapter were calculated by Annabelle Bohrdt.

4.1 Magnetic correlations in unconventional superconductors

While the origin of pairing in unconventional superconductors is still a topic of debate, these strongly correlated materials have some ubiquitous features in common, which might hint at the underlying physical processes at stake. Their phase diagrams, as exemplified in Figure 4.1, display superconductivity emerging in the vicinity of magnetic phases like ferro- and antiferromagnets. Some of these materials, like the cuprates [61], layered organic [69] or graphene [73] based ones, exhibit superconducitivty emerging upon doping antiferromagnetic Mott insulators. These discoveries motivated considerable work aimed at understanding superconductivity mediated by magnetic fluctuations [65].

The Fermi-Hubbard model captures many aspects of the high-T_C superconducting cuprates, including an antiferromagnetic Mott insulating state at half filling and a competition between magnetic and kinetic energy upon doping. It thus has the potential to shed light onto the mechanisms of high-T_C superconductivity. The investigation of magnetically mediated pairing in this model can furthermore affirm the relevance of this process for unconventional superconductors in general. As discussed in chapter 2, doped Fermi-Hubbard ladders allow accurate numerical solutions using DMRG and are thus suitable for developing insight into the problem of pairing in doped Mott insulators.
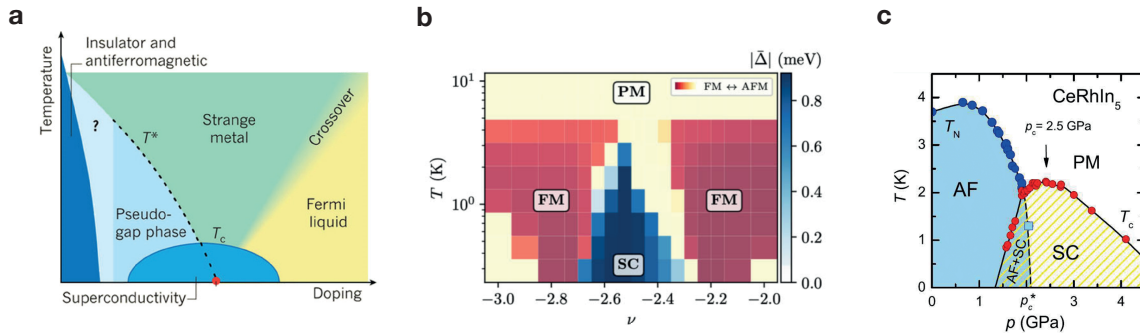
Figure 4.1: Magnetically ordered phases in unconventional superconductors. The exemplary phase diagrams show magnetic phases in the vicinity of the superconducting phase. **a**, Phase diagram of a cuprate superconductor versus temperature (y-axis) and doping (x-axis). It shows an antiferromagnetic phase at low doping and a superconducting phase upon increased doping. Diagram adapted from [218] **b**, Phase diagram of magic-angle twisted trilayer graphene versus doping ν (x-axis) and temperature (y-axis). The superconducting phase appears close to large ferromagnetic areas. Diagram adapted from [219]. **c**, Phase diagram of a cerium-based heavy fermion superconductor versus pressure (x-axis) and temperature (y-axis). Upon increasing the pressure, the material transitions from an antiferromagnet to a superconductor. Diagram adapted from [220]. SC stands for superconductivity, PM for paramagnet, FM ferromagnet, AF antiferromagnet.

A paradigmatic case for theoretical investigation, that has been studied early on and exhibits large binding, is the regime where inter-chain magnetic exchange is larger than single-particle interchain hopping [155]. These parameters could, however, not be justified microscopically for condensed matter systems and are unphysical within the framework of a pure Fermi-Hubbard system. The key motivation for our work was to provide an experimental realization of this system that has originally been considered a theoretical abstraction. We achieve this by extending Fermi-Hubbard ladders at large interactions with a potential offset, which suppresses inter-chain hopping while enhancing spin exchange, effectively realizing a mixed-dimensional (mixD) system [221].

4.2 Pauli repulsion of holes

Pairing of holes has so far not been observed in cold atom systems. The main reason for this is the typically extremely low binding energy much below the spin-exchange energy J. Binding is thus not reachable for state-of-the-art quantum simulators, which can reach temperatures of 0.5 to 0.7 J [56, 124], because they are not able to resolve the energy gap between the bound and unbound state. Here, we apply a novel approach by suppressing charge motion along one direction, which increases the binding energy to the order of the spin-exchange energy. This allows for the realization of bound hole pairs in a quantum simulator and also delineates a strategy to increase the critical
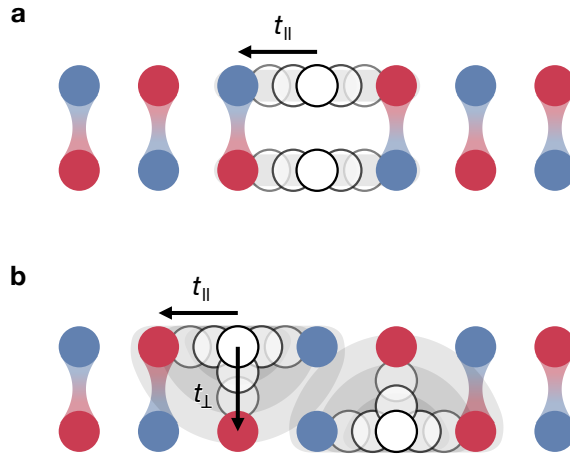
Figure 4.2: Pauli repulsion of holes in ladders. a, Illustration of a ladder system with vanishing rung tunneling $t_\perp = 0$, but finite spin exchange $J_\perp > 0$. Together the two holes can move through the whole system without breaking the spin singlets. Since particles only move along the legs, they are not immediately affected in their kinetic energy by the presence of another hole on the same rung. **b,** Illustration of a ladder system with finite rung tunneling $t_\perp > J_\perp > 0$. Two holes experience a strong mutual repulsion caused by the Pauli principle, which is depicted by the grey shaded area that surrounds each hole. The kinetic energy cost of occupying the same rung is on the order of $t_\perp$. This is why it is energetically more favorable for holes to stay at a certain distance from each other.

temperature for superconductivity.

The typically small binding energy far below J is caused by a competition of hole binding and Pauli repulsion. To understand this, we first recall the origin of pairing as illustrated in Ch. 2, Fig. 2.12. There we have discussed how binding is caused by the interplay of magnetic energy and kinetic energy. While delocalization of a single hole lowers kinetic energy, but increases magnetic energy, a bound pair can delocalize and thus lower their kinetic energy without major disturbance of the magnetic order. In particular, the shorter the average distance between the two holes, the smaller the increase of magnetic energy. Given this picture, the pair size should ideally be small. Since it originates from restoring the spin order, which is governed by the spin exchange energy, the binding energy one would expect a binding energy on the order of J. However, this picture actually only holds when the rung tunneling $t_\perp$ is small compared to the rung spin exchange $J_\perp$, as depicted in Fig. 4.2a. In the standard Fermi-Hubbard model, where the spin exchange is derived as $J_\perp = 4t_\perp^2/U$ for $U \gg t$, the rung tunneling $t_\perp$ is always the dominating energy scale over the spin exchange $J_\perp$. In this case, it is energetically unfavorable for two holes to be at a close distance. The reason is the Pauli repulsion between two holes, as it is shown in Fig. 4.2b. If they occupy neighboring sites, that site is blocked for the other hole, thus restricting the hole from fluctuating on that site. This costs kinetic energy on the order of $t_\perp$. Since $t_\perp > J_\perp$, the energy cost is larger than the energy advantage of forming a strongly

bound hole pair at a short distance.

This does not mean, that pairing is not possible in Fermi-Hubbard systems. But it means that pairs form at a certain distance, which maximizes the advantage of delocalizing through the full system in pairs while keeping the disadvantage from repulsion at a minimum. The size of the hole pair thus depends on the ratio between tunneling and spin exchange. A finite magnetic energy cost is caused by the disturbed magnetic order between the two holes. This competition between hole attraction and hole repulsion effectively lowers the binding energy to values far below the spin exchange energy. In order to reduce the complexity of the pairing problem, early theoretical works considered the parameter regime where $t_\perp$ is small. In this case, only hole attraction contributes to the problem [155], as it is depicted in Fig. 4.2a.

4.3   The mixed-dimensional strategy

In order to realize a system where the rung spin exchange exceeds the tunneling, we engineer a system where rung tunneling is strongly suppressed and becomes negligibly small, while spin exchange along the rungs remains strong. Tunneling and spin exchange in leg direction are not affected by the suppression of rung tunneling. Such a system, which possesses spin exchange in all (both) directions, but in which tunneling is restricted to lower (one) dimension, is in the following called a *mixed-dimensional* or *mixD* system. It is described by the $t - J$ ladder Hamiltonian of Eq. (2.7) with $t_\perp = 0$. The system without suppression of tunneling, which corresponds to the $t - J$-limit of a Fermi-Hubbard system with $t_\perp > J_\perp > 0$, we call the *standard* ladder.

4.3.1   Engineering an effective mixD model in a Fermi-Hubbard type system

A mixD ladder system can be realized as an effective description of Fermi-Hubbard ladders by adding a spin-independent potential offset between the two legs [221]. This can be understood from a single double well with a potential offset Δ between the two sites (see Fig. 4.3). For large enough $\Delta \gg t$, a particle cannot tunnel from one site of the double well to the other. Hopping is suppressed because the two corresponding states $|L\rangle$, the state localized on the left well, and $|R\rangle$, the state localized on the right well, are far detuned from each other.

However, if the other site of the double well is not empty, but occupied by a particle of opposite spin, the two particles can switch positions via a virtual double occupancy. Spin exchange is not suppressed, because the final state and the initial state have the same energy. Thus a potential offset Δ suppresses the tunneling between two sites, but not the spin exchange [222].

The full Hamiltonian of the Fermi-Hubbard ladder system with potential offset is given by

$$\hat{\mathcal{H}} = - \sum_{\langle i,j \rangle, \sigma} -\tilde{t}_{ij} \left(\hat{c}_{i,\sigma}^\dagger \hat{c}_{j,\sigma} + \text{h.c.} \right) + U \sum_i \hat{n}_{i,\uparrow} \hat{n}_{i,\downarrow} + \Delta \sum_{i \in (x,y=1)} \hat{n}_i,$$
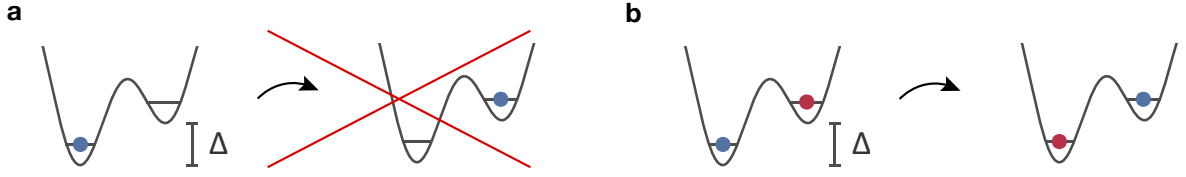
Figure 4.3: Suppression of tunneling using a potential offset. a, A potential offset Δ between two sites of a double well suppresses tunneling. The state shown on the left, before the tunneling event, is far detuned from the state on the right, after the tunneling event. **b**, Spin exchange is not suppressed by the potential offset Δ, because both states, before and after the spin exchange, have the same energy.

where we use the notation $U, \tilde{t}_\parallel, \tilde{t}_\perp > 0$ to refer to the bare Hubbard parameters and distinguish them from the effective parameters $t_\perp, t_\parallel, J_\perp, J_\parallel$, which depend on Δ. For $\Delta \gg 0$, the Hubbard tunneling $\tilde{t}_\perp \neq t_\perp$ is eliminated from the Hamiltonian by working in a time-dependent basis. The resulting $t - J$ Hamiltonian reads

$$\hat{\mathcal{H}}_{tJL} = \sum_{x,y,\sigma} \hat{\mathcal{P}} \left(-t_\parallel \, \hat{c}^\dagger_{x,y,\sigma} \hat{c}_{x+1,y,\sigma} + \text{h.c.} \right) \hat{\mathcal{P}} +$$

$$+ \sum_{x,y} J_\parallel \left(\hat{\mathbf{S}}_{x,y} \cdot \hat{\mathbf{S}}_{x+1,y} - \frac{\hat{n}_{x,y}\hat{n}_{x+1,y}}{4} \right) + \sum_{x} J_\perp \left(\hat{\mathbf{S}}_{x,0} \cdot \hat{\mathbf{S}}_{x,1} - \frac{\hat{n}_{x,0}\hat{n}_{x,1}}{4} \right),$$

where the spin exchange $J_\perp$ gets increased by the potential offset due to a modified energy level for double occupancies. The spin exchange in the presence of a potential offset is given by [223, 224]

$$J_\perp = \frac{2\tilde{t}_\perp^2}{U + \Delta} + \frac{2\tilde{t}_\perp^2}{U - \Delta}, \tag{4.1}$$

which means that it is enhanced for $0 \ll \Delta \ll U$ and switches sign from antiferromagnetic to ferromagnetic spin coupling for $0 < U \ll \Delta$. The formula does not hold for the case of $\Delta = U$, where the double occupancy is resonant with the state of one particle per site and double occupancies are not suppressed anymore.

We note that this effective model does not capture the full physics, but only holds for intermediate timescales where the system is in a metastable state. For small tilts $|\Delta| \ll |\tilde{t}_\perp|$ no such metastability exists but instead the system directly equilibrates to a state where more holes are in the upper leg. Such a system is not described by an effective Hamiltonian with mixed dimensionality, but by the full Hubbard model with Δ and $\tilde{t}_\perp$ terms. In particular this means that tunneling cannot be suppressed gradually by applying small potential offsets. If the potential offset is small, it leads to a faster tunneling rate with a lower amplitude, meaning that the oscillation between the wells becomes faster but only a fraction of the charge actually tunnels, similar to detuned Rabi oscillations (see e.g. [225]).
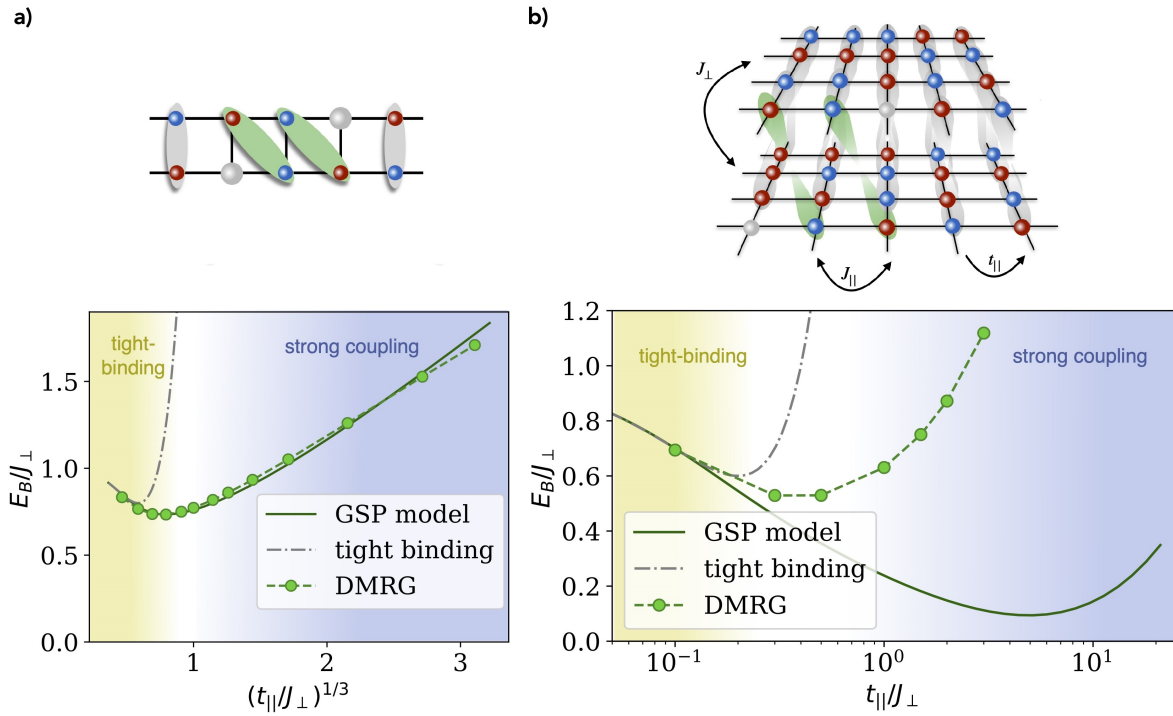
Figure 4.4: Pairing in mixD ladders and bilayers. The binding energies E_B for mixD ladder (**a**) and mixD bilayer (**b**) systems. The sketches illustrate the two systems and their binding mechanisms, with holes colored in white and displaced singlet bonds highlighted in green. The mixD ladder can be understood as a special case of the mixD bilayer system. The figure is adapted from [221], where the curves are obtained by comparing the ground state energy of a single hole to the energy of a hole in a bound pair.

4.3.2 Strong binding in mixed-dimensional systems

Mixed-dimensional ladder systems show strong pairing with binding energies on the order of the spin-exchange energy $J_\perp$. The binding energies expected for different ratios of leg tunneling and rung spin exchange $t_\parallel/J_\perp$ are calculated in [221]. In the following, the theoretical findings of that work are summarized because they lay the foundation for the experimental work presented within this chapter. The authors find two different regimes, the strong coupling regime $t_\parallel \gg J_\perp$, where hole pairs are highly mobile along the leg, and the tight-binding regime $t_\parallel \ll J_\perp$, which consists of weakly coupled rungs. Note that for both regimes the spin exchange is assumed to be dominant along the rung, i.e. $J_\perp \gg J_\parallel$.

Fig. 4.4a shows the binding energy of a mixD ladder system doped with two holes. In the tight-binding regime, the binding energy approaches $J_\perp$ in the limit of uncoupled double wells on the rungs. The binding can be explained as the advantage of forming the highest possible amount of singlets when the two holes occupy the same rung. If $t_\parallel > 0$ the hole pair can move along the ladder, but remains heavy as long as the tunneling is low. In the strong coupling limit the hole pairs are highly mobile and the binding energy exceeds $J_\perp$. The strong binding is caused because a single pair pre-

vents several singlet bonds from being displaced by unbound holes. While the pairs are still tightly bound, the strong leg coupling leads to fluctuations in the position of the constituents of the pair. This fluctuation leads to a pair extension over several sites. The light effective mass of pairs furthermore leads to high condensation temperatures T_C. Hence the mixD approach can potentially boost the critical temperature for the superconducting phase.

In this thesis we realize an experimental system in between the tight-binding and strong coupling regime with $t_{\parallel} = 0.7 J_{\perp}$. In this parameter regime, spin coupling along the rung and dopant motion along the leg compete on similar energy scales. Even though this regime has comparably low binding energy for a mixD system, it still boost the binding energy by an order of magnitude compared to a standard system. Therefore it allows the microscopic observation of the pairing mechanism and investigation of its origin in the competition of hole motion and magnetic correlations. We choose this parameter regime, and not larger leg couplings, due to experimental limitations. In particular the small size of the system requires a separation of scales between the pair size and the system length in order to distinguish pairs from unbound free holes.

4.4 System preparation: a ladder system with potential offset

In order to probe the physics in mixD ladders, and compare them to standard ladders with tunneling $t_{\perp} > J_{\perp}$, we prepare both configurations in our Fermi-gas microscope with the same sequence. The only difference between the preparation sequences is the potential offset, which is either $\Delta > t_{\perp}$ or $\Delta = 0$. To create mixD ladders, we prepare a cold atomic cloud in a single layer of a vertical optical lattice with a balanced mixture of the lowest two hyperfine states of lithium. We then adiabatically load the atoms into the optical lattice in the xy-plane, while simultaneously applying a spin independent light sift using our DMD. The resulting repulsive potential compensates

a Uncoupled 1D chains
$t_{\perp} \ll t_{\parallel}$ and $J_{\perp} \ll J_{\parallel}$

b Apply offset
$t_{\perp} \rightarrow 0$ and $J_{\perp}$ enhanced

c Final parameters
$t_{\parallel}/J_{\perp} \approx 0.7$
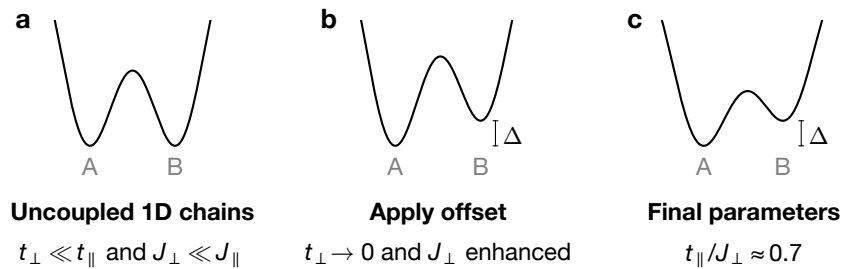
Figure 4.5: Preparation sequence for mixD systems. a, We start by preparing nearly uncoupled 1d chains (the legs of the ladder) with very high mobility along the chain. **b**, We apply the potential offset Δ to one leg of the legs while they are still uncoupled. **c**, We slowly ramp the lattice depth to the final configuration: a mixD system with $J_{\perp} \gg J_{\parallel}$. The potential offset prevents the particles from tunneling between the leg during this preparation step.
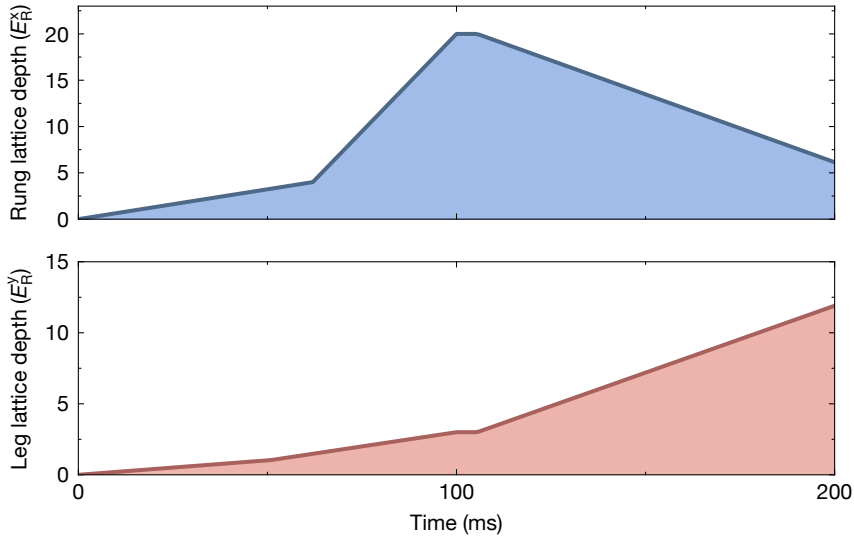
Figure 4.6: Sequence for the lattice ramps. The plots show the lattice depths in the rung and leg direction of the ladders, as they are changed in time during the preparation sequence. They are ramped up in two steps to a regime of nearly decoupled legs. There they are held for 5 ms, during which the DMD pattern is switched. Then they are slowly ramped to the final system parameters.

for the harmonic confinement of the optical lattice beams and shapes the system into the geometry of four two-leg ladders of length $L = 7$. A potential offset Δ is then added on top of the ladder configuration using the same DMD.

The full loading sequence takes part in three steps (a), (b) and (c) (see Fig. 4.5). (a) The initial lattice ramp has two steps, in order to improve adiabaticity when turning on the lattice. The first, slow ramp, slowly turns the rung lattice to $V_r = 4\,E_R$ and the leg lattice to $V_l = 1\,E_R$ within 62 ms, and then the faster ramp increases the depth to $V_r = 20\,E_R$ and $V_l = 3\,E_R$ within 38 ms. The DMD potential is ramped linearly within the same time of 100 ms. The result is a system of two decoupled tubes, which will later form the legs of the ladders.

(b) The optical potential offset Δ is applied to one leg of each ladder. The DMD pattern, which at this point is compensating the harmonic confinement and shaping the ladders, is instantaneously switched, keeping the previous pattern but adding an additional offset to one leg per ladder. Since the legs of the ladder are decoupled by a $20\,E_R$ deep lattice, this quench of the potential does not induce considerable short-term out-of-equilibrium time evolution. We hold in this configuration for 5 ms.

(c) The lattice potential is now slowly ramped to its final parameters of $V_r = 6\,E_R$ and $V_l = 12\,E_R$ within 95 ms. The potential offset prevents the atoms from tunneling between the legs during the full ramp. The details of the lattice ramps and their timing can be seen in Fig. 4.6.

The main purpose of the three-part system preparation is to create a meta-stable state with homogeneous distribution of doping over both legs, instead of the mass imbalanced distribution which corresponds to the ground state of the system. The final parameters give a repulsive on-site interaction of $U = h \times 4.29(10)\,\text{kHz}$ (with
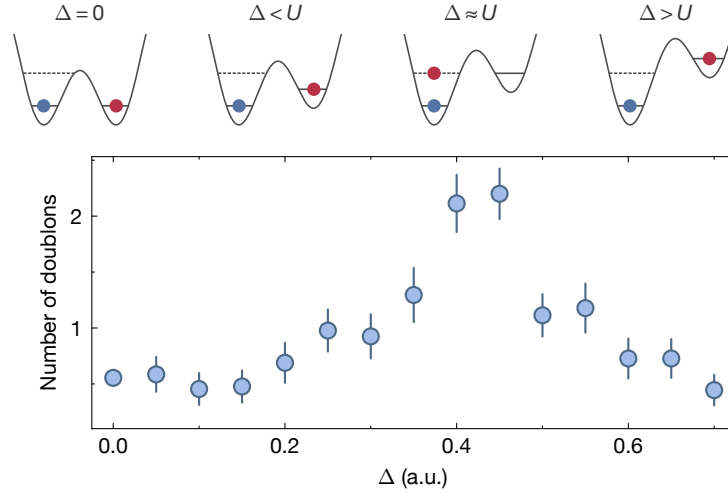
Figure 4.7: Potential offset calibration scan. A scan of the light intensity (x-axis) of the potential offset between the two legs of the ladder. The peak in the doublon number (y-axis) identifies the resonance condition $\Delta = U$.

a scattering length of $a_\mathrm{s} = 1310 \, a_\mathrm{B}$), Hubbard tunneling $\tilde{t}_\parallel = h \times 78(10) \, \mathrm{Hz}$ and $\tilde{t}_\perp = h \times 303(23) \, \mathrm{Hz}$ and the offset $\Delta \approx 0.5 \, U$ or $\Delta = 0$ depending on the configuration (mixD or standard). Note that the notation $\tilde{t}_\parallel$ and $\tilde{t}_\perp$ is used to describe the bare Hubbard parameters, which are distinct from the effective mixD description using $t_\parallel$ and $t_\perp$. Since $U/\tilde{t}_\perp, U/\tilde{t}_\parallel \geq 14$, the system can be effectively described by the $t - J$ model. Along the legs, the $t - J$ tunnel coupling is independent of Δ and is $t_\parallel = \tilde{t}_\parallel = h \times 78(10) \, \mathrm{Hz}$, yielding a spin exchange of $J_\parallel = h \times 5.7(1.5) \, \mathrm{Hz}$. Along the rungs, the mixD system ($\Delta/U \approx 0.5$) yields $t_\perp = 0$ and an enhanced spin exchange $J_\perp = h \times 114(42) \, \mathrm{Hz}$. Without the potential offset, i.e. in the standard system ($\Delta = 0$), tunneling is unaffected, leading to $t_\perp = \tilde{t}_\perp = h \times 303(23) \, \mathrm{Hz}$ and $J_\perp = h \times 86(13) \, \mathrm{Hz}$.

Potential offset calibration

The potential offset Δ is crucial for the suppression of tunneling in the mixD system. Its amplitude is directly proportional to the light intensity, which is controlled by the DMD pattern. The calibration of Δ is performed by varying the light intensity between different experimental realizations and evaluating the number of doubly occupied sites (doublons) in the system. The result of such a scan can be seen in Fig. 4.7. When the potential offset equals the interaction energy U, the doublon number in the system increases, because the lowest band in the upper leg becomes resonant with the interaction band of the lower leg. For a half-filled system of length $L = 7$, one expects on average 3.5 doublons for this resonant condition. We however work with a doped system, such that not each double well is filled with two particles that can create doublons. Furthermore, our system is not perfectly homogeneous, despite a feedback procedure to flatten the potential. This leads to a broadening of the U-resonance peak and a further reduction of the height of the peak. Together these two factors lead to a maximum number of slightly above 2 doublons in the offset scan.
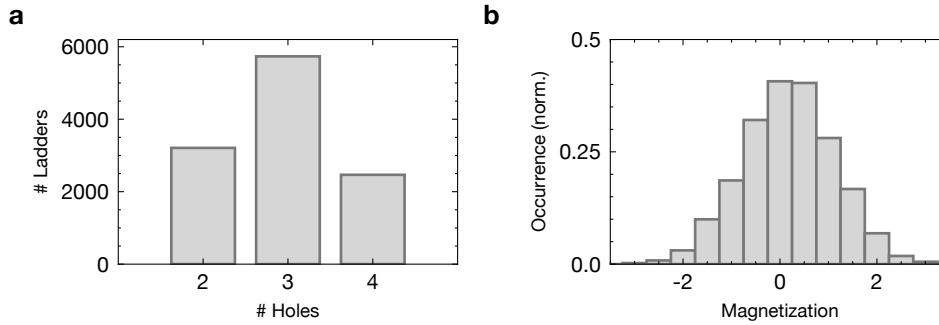
Figure 4.8: Doping and magnetization statistics of the data set. a, Experimental distribution of holes per ladder. The doping of the system lies at around 20% with a maximum in the distribution for three holes. **b**, Histogram of the magnetization per ladder. The most likely magnetization is $M^z = 0$ and $M^z = 0.5$, while the majority of snapshots show a magnetization below two.

We repeat many such scans throughout the data taking, in order to take into account drifts of the system. These drifts are mostly caused by changes in the beam profile of the DMD setup. We observe typical shifts of the doublon peak of $\sim 10\%$. These time-dependent drifts of the doublon peak and the uncertainty of determining U from each single scan, yield an estimated uncertainty on Δ of about $\pm 15\%$. This uncertainty is however not critical for the realization of a mixD setting, since any $t_\perp \ll \Delta \ll U$ is sufficient to suppress tunneling. The height of the offset value influences the precise value of $J_\perp$ and thus contributes to its uncertainty.

4.5   System characterization

Our data collection consists of two types of measurements, one part charge-resolved and another part spin-charge-resolved snapshots. In total we have taken 19 000 experimental shots, iterating between the mixD ($\Delta \approx U/2$) and standard ($\Delta = 0$) configuration. Of these snapshots, 61% have charge-only resolution and 39% are taken with full spin and charge resolution.
Small drifts in the DMD pattern relative to the lattice sites strongly affect the potential landscape of the ladders, especially the balance between the two legs. We thus keep track of the ladder potential by continuous automatic evaluation of the charge distribution and regular feedback to the DMD pattern. If despite the monitoring and regular feedback the average leg-to-leg occupation imbalance of standard ladders exceeds 2 holes, we dismiss the respective set of data due to the uncontrolled drift in the potential.
For data analysis, unless otherwise mentioned, we only take into account ladder snapshots without double occupancies and with a leg-to-leg occupation imbalance of maximally one hole. Furthermore, most results are obtained in the subset with two to four holes per ladder. If the data is postselected on different hole numbers, this is explicitly mentioned. This leaves us with more than 24 000 individual ladders, about half of which contain between two and four holes, as can be seen in Fig. 4.8a. The majority

Figure 4.9: Density of the mixD system. a, Average occupation without postselection. The charge distribution shows a clear imbalance, with the higher density on the lower leg of the system. **b**, Density of the mixD system postselected on having no doub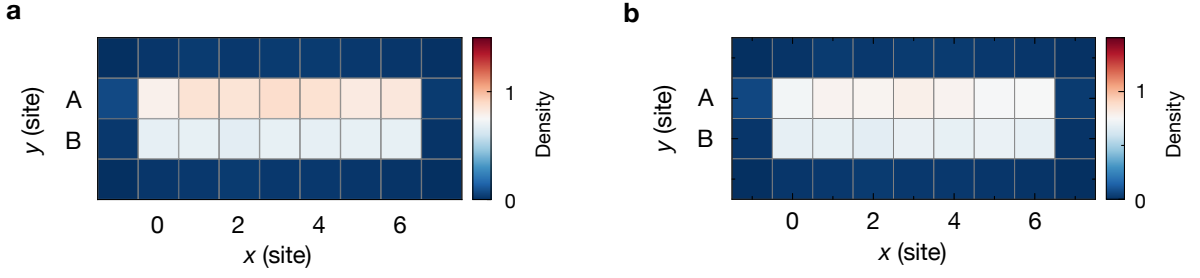lons. The comparison between the two plots shows that doublons on the lower leg have the largest contribution to the density imbalance between the legs.

of ladders contain three holes and thus a leg-to-leg imbalance of one particle. The doping of the data set lies at around 20%. The majority of ladders show a magnetization of $|M^z| < 2$ (see Fig. 4.8b). The magnetization distribution of the data set has a maximum at $M^z = 0$ and a slight imbalance towards positive spin, which has been observed before in our experiment, e.g. [121, 143] and might derive from a small spin dependence in the evaporation process.

Despite our preparation sequence being aimed at the creation of ladders with an equal population in both legs, we see a small density imbalance between the upper and lower leg. Fig. 4.9a shows the average density of the mixD ladders without postselection on doublon number or total occupation. Leg $y = B$, which has the additional potential offset $\Delta \approx U/2$, has a lower density than leg $y = A$. Doublon-hole fluctuations make up the biggest contribution to this imbalance. In the standard system, doublon-hole pairs appear along the rungs with probability $\sim (\tilde{t}_\perp/U)^2$ [57] and the chances for doublons to appear on one leg or the other are symmetric. In the mixD system the potential offset lowers the energy difference between the doubly occupied state and two singly occupied states to $U - \Delta$, if the doublon sits on the lower leg. The energy difference increases to $U + \Delta$ for a doublon on the higher leg. This means that doublon-hole fluctuations with the doublon on leg A are enhanced, while they are suppressed for the doublon on leg B. Fig. 4.9b shows the same density plot, but ladders with double occupancies are removed from the data. The density is more homogeneous, with a small remaining imbalance, probably due to both static and time-dependent imperfections in the potential pattern.

The spin correlations in the system are dominated by a high singlet fraction along the rungs with an average of $C(0,1) = -0.38(1)$. The nearest-neighbor correlations along the leg of $C(1,0) = -0.10(1)$ are however not negligible and indicate that coupling along the leg plays a considerable role in the system. Fig. 4.10 shows a map of the spin correlations for different positions in the ladder. While the rung correlations are relatively independent of position and vary by only about 20 % of their value, the leg correlations vary by about 65 % of their value. There is a tendency for the leg correlation to be weaker in the center, but the trend is not significant.

In order to estimate the temperature of our system, we compare the measured rung
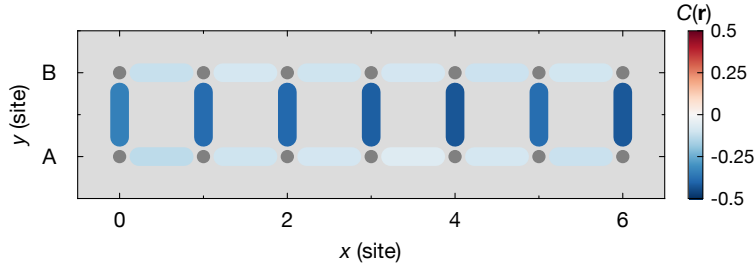
Figure 4.10: Spin correlation map of the mixD system. The space resolved spin correlations $C(0,1)$ and $C(1,0)$ are plotted as bonds, whose color indicates the strength of the correlation. The endpoints of the bonds represent the position of the correlated sites within the ladder.

spin correlations $C(0,1)$ to numerical (MPS) simulations at finite temperature. The MPS snapshots are sampled to match the experimental hole distribution and account for the experimental detection fidelity (details on the numerical simulations can be found in Appendix B). Nearest-neighbor spin correlations are a suitable effective thermometer, because they are directly related to temperature with a strong monotonous dependence in our temperature regime. The mapping of this singlet strength $C(0,1)$ to temperature is plotted in Fig. 4.11a.

The spin correlation vs. temperature calibration can be used to assign a temperature to our data set. The average correlations along the rung in the doped mixD system correspond to a temperature of

$$k_\mathrm{B}T = 0.77(2)\, J_\perp.$$

However, our system is not well described by a single average spin correlation value, but correlation strength varies in time and over the four simultaneously realized ladders. Time-dependent variations are due to slow drifts in the evaporation procedure and beam alignment. These drifts can lead to heating, for example due to mass transport when loading the atoms into the optical lattice after magnetic evaporation. Spatial differences in temperatures between the different ladders are due to differences in the optical potential and varying degrees of exchange with the outer bath, which is supposed to host particles of higher entropy.

We characterize the variations by computing rolling averages of the spin correlations with a window size of about 24 h. Each of the four ladder positions is evaluated independently. Each shot is then assigned a temperature, based on the average spin correlations in its time window. The distribution of these time-dependent spin correlations is plotted in Fig. 4.11b. It reaches from $C(0,1) = -0.5$ to $C(0,1) = -0.2$ and has a relatively flat maximum around the average spin correlation value. Fig. 4.11c shows the distribution of temperature derived from the spin correlations in Fig. 4.11b, which reaches from below $k_\mathrm{B}T = 0.6\, J_\perp$ to above $k_\mathrm{B}T = 1.0\, J_\perp$, with a long but thin tail of even hotter temperatures.
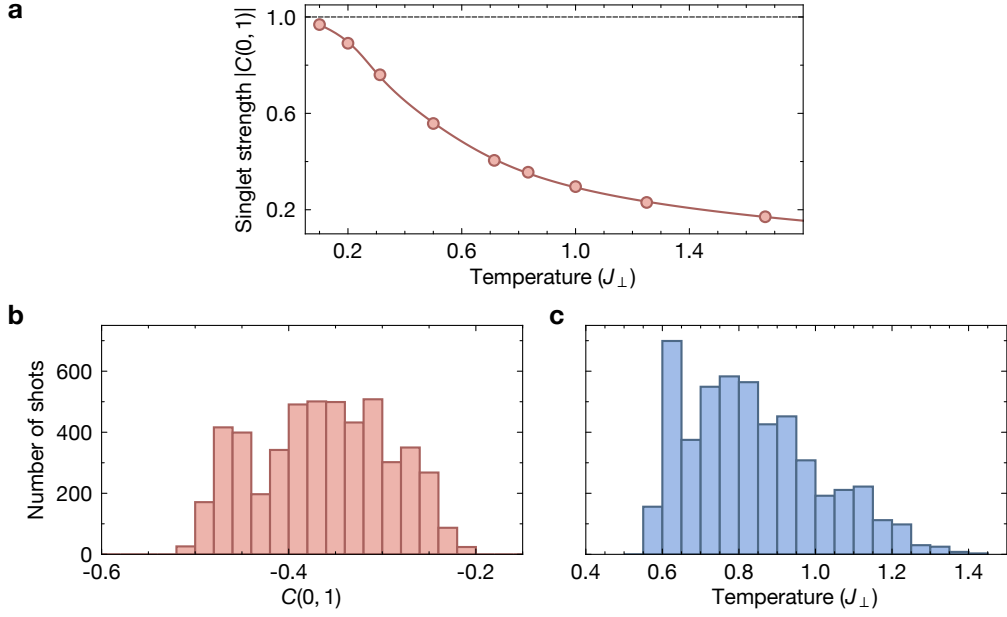
Figure 4.11: Temperature estimation of the data set. a, Rung singlet strength versus temperature. The spin correlations show a strong decay between temperatures of $0.1\,J_\perp$ to $1.0\,J_\perp$. The temperature calibration is based on finite temperature MPS snapshots. **b,** Distribution of the experimental singlet strength $C(0,1)$ in time windows (rolling average) of about $24\,\mathrm{h}$. Each time bin is assigned a temperature based on the calibration curve of **a**. The resulting distribution of temperatures is plotted in **c**.

4.6 Hole pairing

In the following section we analyze the hole-hole correlation in the mixD system and contrast it with the hole-hole correlation in the standard system. The mixD system shows significant hole pairing of tightly bound pairs, while the standard system shows repulsion of holes at close distances. Fig. 4.12 shows an example shot containing two holes on the same rung in the mixD ladder system, which is characteristic for tightly bound pairs.

We find a high probability for snapshots to contain two neighboring holes. This is shown in Fig. 4.13a, which shows the histograms of mutual hole distance d, for two holes on different legs. The plotted quantity is described by the excess events

$$\delta_{\mathrm{h}}(d) = \sum_{i-j=(d,1)} (\langle \hat{n}_i^{\mathrm{h}} \hat{n}_j^{\mathrm{h}} \rangle - n_{\mathrm{h}}^2), \tag{4.2}$$

where $\hat{n}_i^{\mathrm{h}}$ denotes the hole-density operator at position i. In this formula, we subtract the global hole density n_{h}, in order to correct for finite size effects. In a small system and random hole distribution, short hole distances are more likely than large distances, because there are more possible combinations of short distances in the system. Eq. (4.2) has this offset removed.

In the mixD ladders the occurrence of hole distance $d = 0$ is strongly enhanced
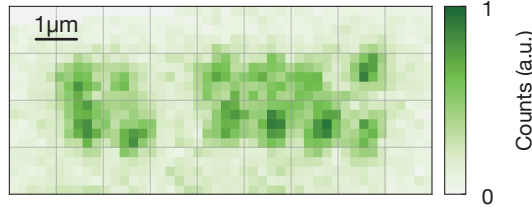
Figure 4.12: Example snapshot of the mixD system. A single experimental snapshot containing two holes on the same rung. While a single occurrence does not demonstrate binding between these holes, the high probability of snapshots featuring holes on the same rung leads to the conclusion of a bound state.

(Fig. 4.13a), corresponding to two holes on the same rung. The slight asymmetry of the distribution is caused by optical potential inhomogeneities in our system. The standard ladders on the other hand show strong repulsion on the same rung (Fig. 4.13b). The positive excess events for larger distances do not indicate pairing, but derive from the finite system size. If holes avoid close distances, the probability for larger distances is in return increased.

4.6.1 Hole correlations

In order to characterize the pairing of holes in our system, and to exclude trivial effects like bunching from potential inhomogeneities, we further investigate the signal. We use the density-normalized, connected two-point correlator

$$g_h^{(2)}(r) = \frac{1}{\mathcal{N}_r} \sum_{i-j=r} \left(\frac{\langle \hat{n}_i^h \hat{n}_j^h \rangle}{\langle \hat{n}_i^h \rangle \langle \hat{n}_j^h \rangle} - 1 \right), \tag{4.3}$$

where $\mathcal{N}_r$, the number of sites i, j at distance r, is a normalization of the sum in order to obtain the average value. The function $g_h^{(2)}(r)$ is a connected correlator, meaning it removes uncorrelated contributions like potential inhomogeneities. These can influence the uncorrelated contributions because potential defects can lead to holes being more likely in certain positions, independent of the presence of other holes. The correlator $g_h^{(2)}$ returns a negative value if the presence of a hole at position i makes the presence of a second hole at distance r less likely, and a positive value if it makes it more likely. The correlator is bounded by $-1 \leq g_h^{(2)}(r) \leq (1/n_h - 1)$, where $n_h = N_h/2L$ is the hole density with the number of holes N_h in the system. Note that we use the more explicit notation $g_h^{(2)}(d_x, d_y)$ instead of $g_h^{(2)}(r)$, wherever the distance r is kept fixed along one or two directions. In the following, we will consider hole correlations within the same leg $g_h^{(2)}(d, 0)$, as well as correlations between holes in different legs $g_h^{(2)}(d, 1)$, as depicted in the schematic ladder system on top of Fig. 4.14a.
The hole correlations between different legs (Fig. 4.14a) have a maximum at distance $d = 0$ of $g_h^{(2)}(0, 1) = 0.15(2)$, which correspond to two holes occupying the same rung.
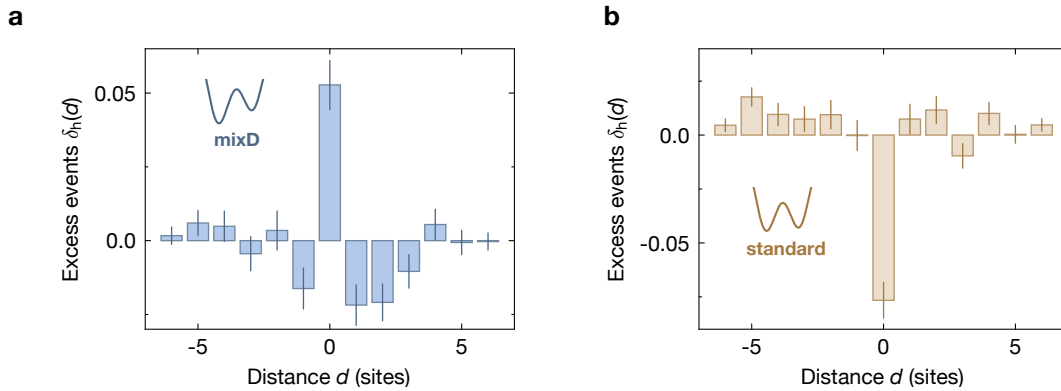
Figure 4.13: Excess events of hole distance in the mixD and standard ladder. The figure shows the occurrence of excess events $\delta_h(d)$, that is the likelihood to find holes at distance d compared to the infinite temperature distribution. **a**, for mixD ladders, and **b** for standard ladders. Error bars denote one s.e.m.

This significantly positive connected correlation shows that holes pair in the mixD ladder. The signal qualitatively agrees with the theoretical prediction. The measured correlation value sharply drops at $|d| = 1$, which shows that the hole pairs are tightly bound and mostly occupy the same rung. The exponential decrease of correlation strength which is expected to occur with distance, is not visible in the plot due to the presence of up to four holes per ladder. These additional holes are most likely to be found at a distance of three to five sites from the pair, which can be seen by the broad maximum of $g_h^{(2)}(|d|, 1)$ around these distances. This broad distribution overshadows the exponential extension of the pair and leads to a minimum at distance $|d| = 1$.

Fig. 4.14b shows the hole correlation $g_h^{(2)}(|d|, 0)$ for several holes on the same leg. The correlation is corrected for a finite-size offset (see below). The curve has a minimum at distance $d = 1$, which shows repulsion of holes along the leg direction. This is not surprising, as Pauli repulsion is only suppressed along the rungs, but remains present along the leg. The visibility of this repulsion demonstrates the significant mobility of holes along the leg. The correlator shows a broad maximum at distances $|d| = 3$ to $|d| = 5$, because the holes try to maximize their mutual distance while avoiding the system edge. Occupying the system edge comes with a high cost in kinetic energy, because particles cannot delocalize into the wall. Note that the hole correlation within the same leg and the hole correlation between opposite legs show a qualitatively similar broad maximum around $d = 4$. This is most likely caused by the same effect.

Finite size offset

Two-point density correlations, as well as spin correlations, are prone to finite-size offsets in small systems. The reason is self-correlation at fixed particle number N. Finding a particle at position r_1 makes it less likely to find a particle at any other position r_2 because only $N - 1$ particles are left to occupy other sites. These finite size offsets do not affect hole correlations between opposite legs, because the hole density

Figure 4.14: Hole-hole correlation in the mixD ladder. **a**, Hole-hole correlation $g_{\mathrm{h}}^{(2)}(|d|,1)$ of holes in opposite legs in the mixD ladder versus absolute distance $|d|$. The correlator is illustrated by the sketch above the plot. A significant positive correlation appears at distance $d = 0$, corresponding to two holes on the same rung and indicating the presence of tightly bound pairs. The experimental data is compared to the theoretical prediction at $k_{\mathrm{B}}T = 0.8\,J_{\perp}$ calculated using MPS (shaded line) and corrected by the experimental detection fidelity. **b**, Offset corrected hole-hole correlation $g_{\mathrm{h}}^{(2)}(|d|,0)$ of holes in the same leg for the mixD ladder versus absolute distance $|d|$. Illustrated by the sketch above the plot. The negative correlation at distance $|d| = 1$ shows that holes repel each other within the same leg. The error bars are calculated by bootstrapping.

is independent for each leg due to the previously described preparation sequence. Hence, self-correlation between positions in different legs does not appear. Hole correlations within the same leg, however, are strongly affected by finite-size offsets. We correct for these finite size offsets using

$$g_{\mathrm{h}}^{(2)}(d,0) = \frac{1}{\mathcal{N}_d} \sum_{i-j=(d,0)} \left(\frac{\langle \hat{n}_i^{\mathrm{h}} \hat{n}_j^{\mathrm{h}} \rangle}{\langle \hat{n}_i^{\mathrm{h}} \rangle \langle \hat{n}_j^{\mathrm{h}} \rangle} \frac{N_{\mathrm{l}}}{N_{\mathrm{l}} - 1} - \frac{L}{L-1} \right), \qquad (4.4)$$

where N_{l} is the number of holes in the leg and L is the length of the leg. The offset correction applies a global correction, affecting the absolute value, but not the shape of the curve. This offset correction is applied to the curve in Fig. 4.14b.

Standard ladder

The presence of tightly bound pairs in the mixD ladder setup stands in direct connection with the suppression of tunneling along the rungs. The suppression of tunneling eliminates the Pauli repulsion between holes and thus strongly enhances the binding energy and pair size. To confirm this, we compare the correlations of the mixD ladder
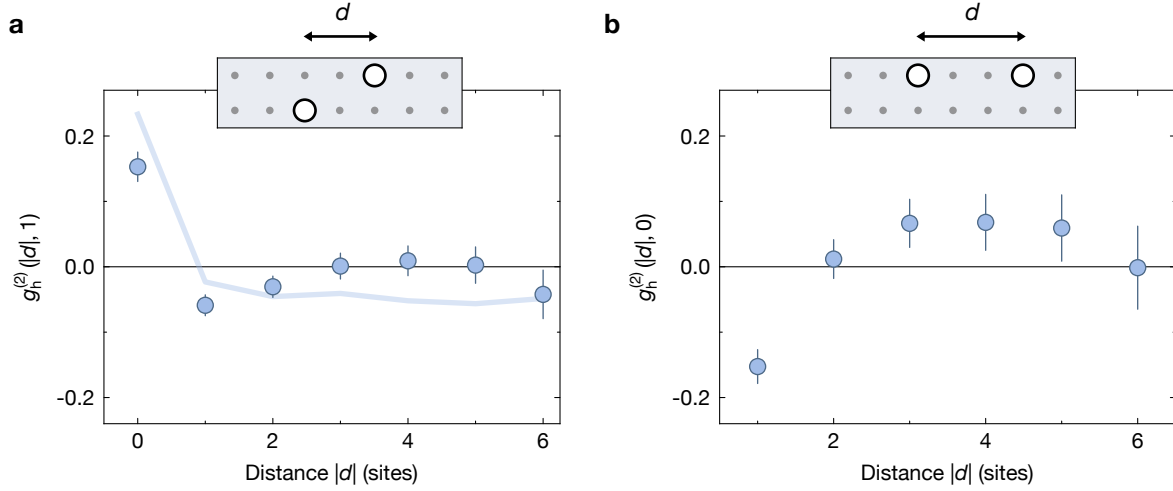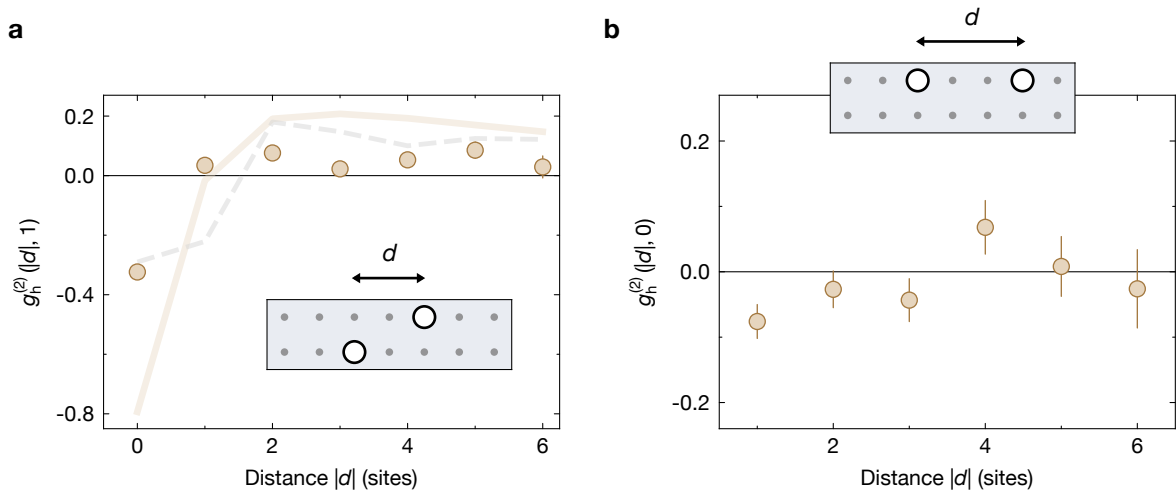
Figure 4.15: Hole-hole correlation in the standard ladder. a, Hole-hole correlation $g_{\mathrm{h}}^{(2)}(|d|,1)$ of holes in opposite legs in the standard ladder versus absolute distance $|d|$, as illustrated by the sketch. A strong negative correlation appears at distance $d = 0$, indicating that holes avoid occupying the same rung. The experimental data is compared to the theoretical prediction at $k_{\mathrm{B}}T = 0.7\,J_{\perp}$ calculated using MPS (shaded line) and corrected by the experimental detection fidelity. The grey dashed line shows MPS calculations with a random disorder $\sim t_{\perp}$ in the potential at $k_{\mathrm{B}}T = 0.5\,J_{\perp}$. **b**, Offset corrected hole-hole correlation $g_{\mathrm{h}}^{(2)}(|d|,0)$ of holes in the same leg for the standard ladder versus absolute distance $|d|$, as illustrated by the sketch above the plot. The negative correlation at distance $|d| = 1$ shows, that holes repel each other within the same leg. The error bars are calculated by bootstrapping.

to the standard ladder with strong rung tunneling $t_{\perp} > J_{\perp}$.

Fig. 4.15a shows the hole correlation on opposite legs $g_{\mathrm{h}}^{(2)}(|d|,1)$ in the standard system. There is a strongly negative value at distance $d = 0$, which corresponds to strong repulsion of holes along the same rung and shows that tightly bound pairs are energetically unfavorable in this system. This does not show that pairing cannot exist in this system, it only demonstrates that the system does not feature tightly bound pairs. At our experimental temperatures, we cannot resolve small binding energies, and at our system sizes, pairs of large sizes cannot be distinguished from random hole distributions. The measured hole correlator shows two small, but distinct maxima and distances $|d| = 2$ and $|d| = 5$. We assume these are caused by the presence of up to two holes per leg. The pattern is consistent with a checkerboard pattern of particles and holes in the ladder system, which is to be expected if holes repel each other both on the rungs as well as along the leg.

The numerical simulation (shaded line in Fig. 4.15a) qualitatively agrees with the experimental results, but shows a repulsion more than twice as strong as in the experimental data. We attribute this discrepancy to inhomogeneities, which affect the tunneling probability in the standard ladder. We see in the MPS simulations that adding

a random disorder to the standard ladder decreases the hole repulsion. For disorder of order $t_\perp$, we find a reduction that is even stronger than in the experimental data and thus gives us an upper boundary for this type of disorder in the system. We note that the simulated system with disorder does not reproduce our experimental observations for distance $d = 1$. We attribute this to the type of the disorder, which is random in the MPS data, but has systematic reasons in the experiment. We thus do not expect to reproduce the exact experimental result with this simulation.

We can identify the DMD-shaped potential as the most likely source for these inhomogeneities. Residual light speckles and finite resolution introduce spatially varying disorder to the ladder potential, while drifts of the ladder potential with respect to the lattice grid can also cause a small offset between the two legs. When the potential wall between ladders drifts partially onto the lattice sites, a small potential offset is added onto one of the legs, but not the other one. Drifts as small as a fraction of a lattice site can indeed already create a potential offset on the order of $t_\perp$ between the legs. We note that this has a negligible effect on the suppression of tunneling in the mixD system. The quenched effective tunneling vanishes due to the potential offset Δ, which is much larger than the disorder in our system and therefore mostly insensitive to it. Furthermore, spin-independent potential inhomogeneities, on the scale present in the experiment, do not alter the spin exchange significantly, but only lead to a small correction lying within the error bars of our system parameters.

Fig. 4.15b shows the hole correlator $g_\mathrm{h}^{(2)}(|d|, 0)$ of holes on the same leg. The value at distance $d = 1$ is significantly negative, but smaller than in the mixD case. This means there is repulsion along the leg, but the physics is mostly dominated by the much stronger tunneling along the rungs. The correlation peaks at distance $|d| = 4$, consistent with the repulsion along the legs in the mixD ladder.

4.6.2 Doping and magnetization dependence

To gain a better understanding of the system dependencies, we analyze how the pairing strength depends on the doping and magnetization of the system. For that, we consider the rung hole-hole correlation $g_\mathrm{h}^{(2)}(0, 1)$, which can be used as a measure of the pairing strength due to the small pair size. In Fig. 4.16a we plot the dependence of this pairing strength on the magnetization of the system. We see that the data points are consistent with a trend towards less pairing at higher total magnetization. This is to be expected, because the pairing is mediated by the magnetic correlations in the system. these correlations get reduced for magnetization imbalance. A fully magnetized system would show neither singlets nor pairing. For the standard system, on the other hand, magnetization does not affect the hole correlations, because Pauli repulsion does not depend on the magnetic environment. Unfortunately, we do not have enough data to analyze higher magnetization sectors. Due to the reduced statistics of spin-resolved shots, averaging over magnetization sectors (horizontal bars in Fig. 4.16a) was necessary in order to reduce the error bars on $g_\mathrm{h}^{(2)}(0, 1)$.

Furthermore, we investigate the dependence of pairing strength on doping, that is, on the number of holes in the system. For this, we adjust the correlator $g_\mathrm{h}^{(2)}$ to compensate
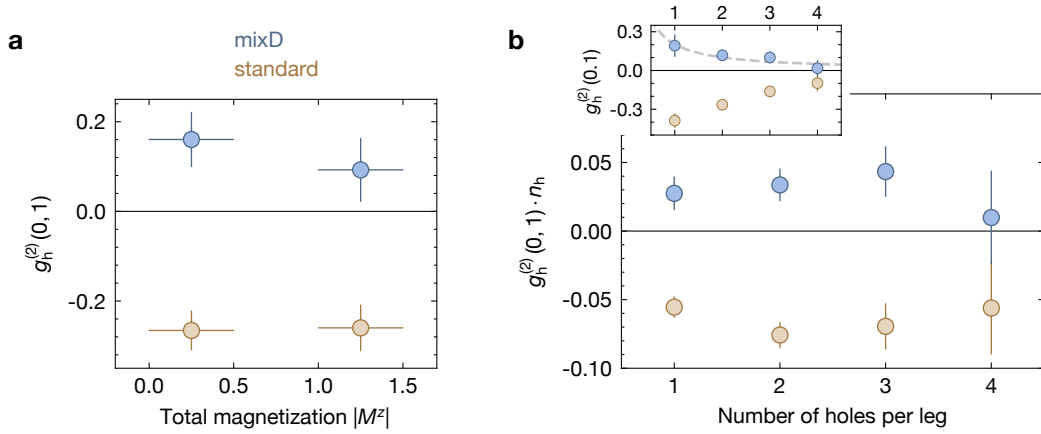
Figure 4.16: Doping and magnetization dependence of pairing. a, Rung hole correlation $g_{\mathrm{h}}^{(2)}(0,1)$ depending on the total magnetization $|M^z|$ of the system for the mixD (blue) and standard (brown) ladder. The pairing strength in the mixD system decreases with increasing magnetization imbalance. **b**, Rung hole correlation $g_{\mathrm{h}}^{(2)}(0,1)$ scaled with the hole density n_{h} depending on the number of holes per leg for the mixD (blue) and standard (brown) ladder. Within the error bars, we find this scaled correlator to be independent of doping. The inset shows the correlator $g_{\mathrm{h}}^{(2)}$, which decreases with doping but is consistent with the inherent density-dependent scaling of the correlator, as it can be seen by the $1/n_{\mathrm{h}}$ fit (dashed line). Vertical error bars denote one s.e.m. Horizontal error bars in **a** denote the magnetization bin width.

for its intrinsic density-dependent $1/n_{\mathrm{h}}$ scaling. Multiplying the correlator with this scaling factor leads to an adjusted correlator $g_{\mathrm{h}}^{(2)} \cdot n_{\mathrm{h}}$, which is plotted in Fig. 4.16b. The experimental results do not show a significant doping dependence. For pairing in the mixD ladder, this is consistent with a system of independent pairs. The inset of Fig. 4.16b shows the correlator $g_{\mathrm{h}}^{(2)}$ which is not corrected for its intrinsic density dependence. This correlator decreases with increasing number of holes per leg but is consistent with a $1/n_{\mathrm{h}}$ fit.

4.6.3 Binding energy

We estimate the binding energy of holes from the measured $g_{\mathrm{h}}^{(2)}(0,1)$ correlator. To that end, we analytically derive a formula for the binding energy based on the assumption that the system is reasonably close to the uncoupled rung limit. We furthermore assume there are exactly two holes in the system and describe the bound state by two holes occupying the same rung. We arrive at the following expression

$$E_{\mathrm{b}} = -\beta^{-1} \ln \left[\frac{\left(1 + 3e^{-\beta J_{\perp}}\right)\left(1 - \frac{g_h^{(2)}(0,1)}{L-1}\right)}{4\left(1 + g_h^{(2)}(0,1)\right)} \right], \tag{4.5}$$

where $\beta = 1/(k_B T)$. The detailed derivation can be found in Appendix A.

We insert our estimated temperature of $k_B T = 0.77(2) J_\perp$, system length of $L = 7$, and the measured value for the $g_h^{(2)}(0,1)$ correlator into this formula. Since our derivation assumes exactly one hole per leg, we cannot simply insert the correlation value obtained from averaging over several density sectors. We can however use the measured correlation value for exactly one hole per leg, as in the inset of Fig. 4.16b and apply a small correction to account for our detection fidelity. This leads to

$$E_b = 0.79(9) J_\perp,$$

where the error derives from the error on the experimental value and the error on the temperature estimation. We can reduce the error by using the correlation value obtained from averaging over several density sectors. Using the insights obtained from Fig. 4.16b, we can correct this correlation value by applying a density-dependent n_h correction factor. This yields

$$E_b = 0.82(6) J_\perp, \tag{4.6}$$

which is consistent with the previous result of exactly one hole per leg.

The experimentally derived binding energy is consistent with DMRG calculations, which suggest a binding energy of $E_b^{\text{theo}} = 0.81 J_\perp$. This is an order of magnitude larger than the highest binding energy that can be achieved in a standard ladder with the same interaction strength (see section 4.6.3 below for a detailed discussion of the binding energy in the standard ladder). Finding strategies to increase the binding energy is an essential ingredient to achieve higher temperature superconductivity, a quest for quantum simulation and material science alike.

In Fig. 4.17, we have plotted the rung hole correlation $g_h^{(2)}(0,1)$ for different temperatures and binding energies as they are predicted by the derived formula of Eq. (4.5). As expected, the hole correlator is strongly positive at very cold temperatures for all binding energies. In this case mostly the ground state is occupied. Also for very high temperatures all binding energies show the same behavior with the hole correlator approaching zero. However, around the temperatures of our system, the hole correlation turns negative for small binding energies around $0.5 J_\perp$ and below. This makes it impossible to detect binding through the $g_h^{(2)}$ correlator in this temperature regime. For $E_b = 0.8 J_\perp$, the correlator stays positive and binding can thus also be detected at higher temperatures given enough statistics.

Negative correlation values $g_h^{(2)}$ at intermediate temperatures happen when the binding energy is much smaller than the spin gap of the system. The reason is, that the spectrum features more low-lying unbound states, than low-lying bound states, despite the ground state being a bound one. This is illustrated in Fig. 4.18. We consider only states that do not break the singlet gap. These states are relatively low in energy. In that case, a ladder containing a pair has all spin directions fixed, because they all form singlets. In a ladder with an unbound pair, however, there are four different combinations of spin states, that do not break the singlet gap. That means there are more unbound states with low energy than bound states. The unbound states are
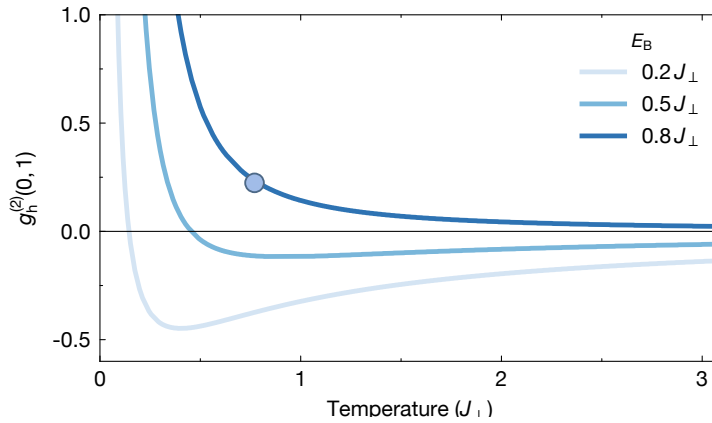
Figure 4.17: Hole correlation strength $g_{\mathrm{h}}^{(2)}(0,1)$ **as predicted by the simplified analytic model.** The rung correlation $g_{\mathrm{h}}^{(2)}(0,1)$ as predicted by our model (Eq. (4.5)) is plotted against temperature for a binding energy of $E_{\mathrm{b}} = 0.3J_{\perp}$ (light blue), $E_{\mathrm{b}} = 0.5J_{\perp}$ (blue) and $E_{\mathrm{b}} = 0.8J_{\perp}$ (dark blue). For our experimental system of $k_{\mathrm{B}}T = 0.77(2)J_{\perp}$, only the high binding energy yields a positive $g_{\mathrm{h}}^{(2)}(0,1)$. The marker indicates the experimental result.

E_b higher in energy than the paired state, but for intermediate temperatures $T \gtrsim E_b$, due to the minimization of free energy, the system will be more likely to occupy an unbound state than a paired state.

Binding energy in the standard ladder

The standard ladder is realized with $t_{\perp}$ four times larger than $t_{\parallel}$. For these parameters and our experimental system size of $L = 7$, our theoretical calculations show no signatures of a bound state. Even if we consider a much larger system of $L = 80$ containing two holes, we see that the holes preferably occupy the opposite sides of the ladder. Fig. 4.19 shows a map of the bare hole correlator $\langle \hat{n}_{\mathrm{h}}^i \hat{n}_{\mathrm{h}}^j \rangle$ at zero temperature for the standard and the mixD system of length $L = 80$. The mixD system shows tightly bound pairs, sitting preferably on the same rung and avoiding the system edge. The standard system shows no such structure. Instead, one hole occupies one side of the
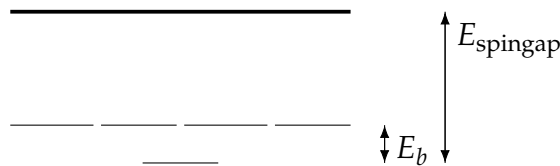
Figure 4.18: Illustration of spin gap and binding energy in the spectrum. The low energy part of the spectrum of a ladder system with two holes features more unbound states than bound states. The difference between the binding energy and the spin gap thus determines the sign of the hole correlator $g_{\mathrm{h}}^{(2)}(0,1)$ at finite temperatures.
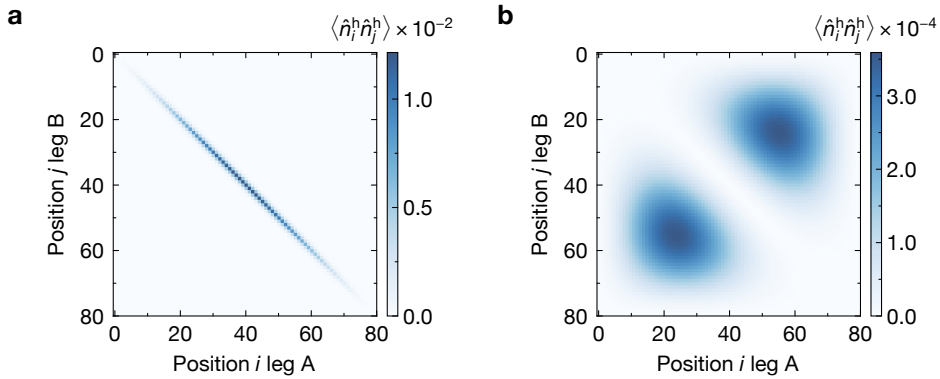
Figure 4.19: Hole correlation in a large system. Maps showing the bare correlator $\langle \hat{n}_h^i \hat{n}_h^j \rangle$ in a system of $L = 80$ at zero temperature. The coupling parameters correspond to the experimental system for mixD ladders (**a**) and standard ladders (**b**). While holes are tightly bound in the mixD ladders, they avoid each other in the standard system. The calculations were carried out using DMRG.

ladder, between site $x = 10$ and site $x = 40$ and the other hole occupies the other side of the ladder, between site $x = 40$ and site $x = 70$. The edges of the system are not occupied because of the high associated energy cost. This shows that even in this large system, no effect of pairing, meaning no degree of attraction between the holes, can be seen. We however suspect that the binding energy is not completely zero, but instead too small to be identified in our calculations.

The theoretical binding energies in standard ladders increase with increasing $t_\parallel$, a tendency that also holds for the mixD ladder [221]. We find the strongest binding energies in standard ladders for the isotropic case $t_\perp = t_\parallel$, where we find $E_B = 0.006 J_\perp$ for a ladder system of $L = 7$ and interactions strength similar to the experimental system with $U/t_\perp = 13.4$. This means the binding energy we have achieved in the mixD setting is about a factor of 13 larger than the highest achievable binding energy for the standard ladder, even though the parameters of our mixD system are not optimized for large binding energies (see eg. Fig. 4.4a). For parameter regimes that are not accessible from the pure Fermi-Hubbard model, as well as for lower $U/t_\perp$ values, higher binding energies are predicted in isotropic $t - J$ ladders, e.g. [84, 155, 226].

4.6.4   Limits of the $t - J$-model as an effective description of Hubbard ladders

Binding energies for isotropic $t - J$ ladders derived from the Fermi-Hubbard model have been predicted to be as large as $0.6 J$ [84, 226]. We however find that simulations taking into account the full Fermi-Hubbard model predict considerably smaller binding. For the isotropic Fermi-Hubbard ladder we find, in agreement with [227], that binding energies do not exceed $0.25 J$.

We attribute these discrepancies to the additional next-nearest neighbor tunneling term (see section 2.4.1 and [102]), which arises in the derivation of the $t - J$ model
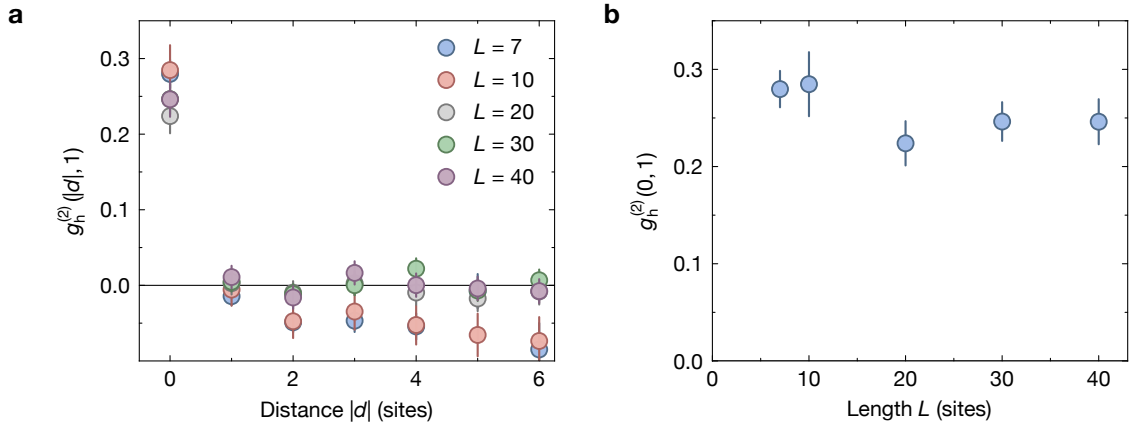
Figure 4.20: Numerical hole-hole correlation in different system sizes. **a**, Hole-hole correlation $g_{\mathrm{h}}^{(2)}(|d|, 1)$ in a mixD system of different lengths between $L = 7$ and $L = 40$ at a temperature of $k_{\mathrm{B}}T = 0.7\,J_\perp$ calculated using MPS. The hole doping is kept constant at 15 % to 30 %. The points at $|d| = 0$ are plotted against system size in **b** and show no significant trend for systems larger than $L = 10$.

but is often neglected because it is much smaller than the nearest-neighbor tunneling term. Assuming a perfect antiferromagnetic checkerboard for the spin pattern, one can however see that next-nearest neighbor tunneling is much more beneficial for dopant delocalization because it does not disturb the spin pattern.

In our mixD ladder system, we avoid the discrepancy between the $t - J$ and Fermi-Hubbard model, because the only term arising is $\sim t_\parallel^2/U \ll J_\perp, t_\parallel \ll t_\perp$, which is much smaller than the relevant energy scales in the system and can thus be omitted. In the standard ladder, however, there are more possible processes like $\sim t_\parallel t_\perp/U$. In the isotropic regime and with lower U/t these terms become increasingly important to the physics of the system. In that regime, the Fermi-Hubbard ladder is not well approximated by the $t - J$ ladder anymore. Even though it appears to make only a quantitative difference in the binding energy in our ladders, the discrepancy can quickly lead to qualitative differences in a system with many competing processes and comparable energy scales.

4.6.5 Finite size effects

With a length of $L = 7$, the experimentally realized ladder system is relatively small. To ensure that the physics we observe in this system is not dominated by finite-size effects, we compare our results to numerical simulations of large systems. It has already been shown in Fig. 4.19a, that pairing persists in systems of length $L = 80$. In Fig. 4.20a, the numerically simulated hole-hole correlations are plotted versus distance. We consider systems of several sizes at a temperature of $k_{\mathrm{B}}T = 0.7\,J_\perp$. The main difference between the system sizes is that small systems show a negative correlation for distances $d > 1$. This negative value is a consequence of finite-size effects. Fig. 4.20b shows the rung correlation value plotted against system size. Be-
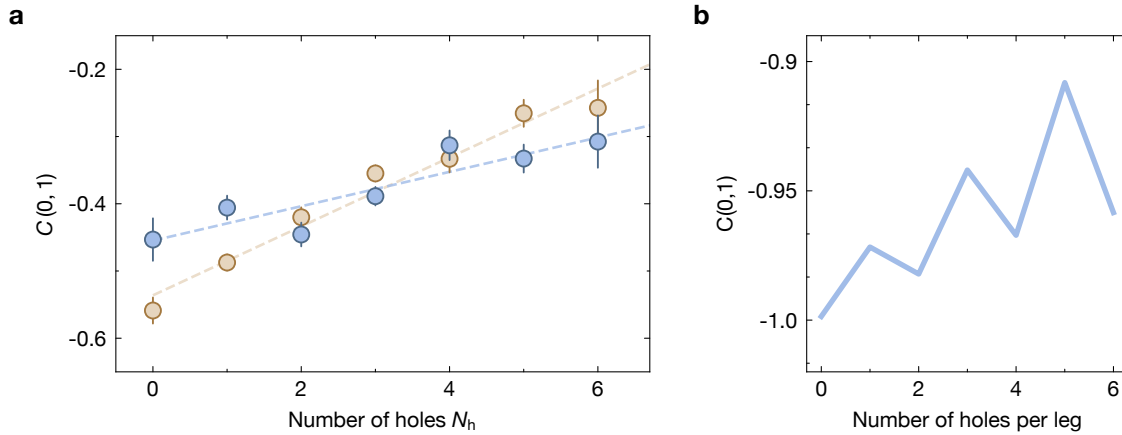
Figure 4.21: Singlet strength depending on doping. a, Rung spin correlations $C(0,1)$ of the experimental system are plotted versus the number of holes in the system for the mixD (blue) and standard (brown) ladders. For both systems, the singlet strength decreases with increasing doping, but the slope is more shallow for the mixD system. Dotted lines denote linear fits to the data. Error bars denote one s.e.m. **b**, Numerical simulation of the spin rung correlation at a temperature of $0.1\,J_\perp$, calculated using MPS. The curve shows a strong even-versus-odd dependence on the hole number.

sides slightly higher correlation values for very small systems $L \leq 10$, the correlation strength seems to stagnate at a constant value.

We see a similar picture calculating the binding energy for different system lengths. While the system of length $L = 7$ has a binding energy of $E_{\mathrm{B}}^{\mathrm{theo}} = 0.81\,J_\perp$, we find that the value settles quickly to around $E_{b,\infty} = 0.78\,J_\perp$ for larger systems. For length $L = 40$ rungs we find $E_{b,40} = 0.7805\,J_\perp$ and for $L = 80$ rungs we find $E_{b,80} = 0.7797\,J_\perp$. This demonstrates that our system with its tightly bound pairs provides a good approximation to the physics in larger systems. While or $L = 7$ system is small, it is still many times larger than the hole pair, which predominantly occupies a single rung. The separation of lengthscales allows us to approximate the physics in the thermodynamic limit despite the relatively small system size.

4.7 Magnetic environment

The pairing mechanism in our Fermi-Hubbard ladders, which we assume to simulate pairing in unconventional superconductors, is mediated by the magnetic correlations in the system. To understand better the important interplay of magnetic background and hole pairs, we investigate the magnetic environment in the system.

Fig. 4.21a shows the rung spin correlations $C(0,1)$ for the mixD and standard ladders depending on the number of holes in the system. The singlet strength decreases with increasing hole number for both systems. They do, however, not decrease at the same rate, but the correlations in the standard system decrease faster than in the mixD system. This can be explained by the presence of pairs in the mixD system, while the

standard system only contains independent holes. Mobile single holes shuffle around the spin occupation in the system, thereby displacing the singlet bonds and decreasing the singlet strength. In the mixD ladders, holes are bound in pairs, which can freely move in the system without considerable damage to the spin environment. The decrease in correlation strength is thus caused by unbound holes, whose kinetic energy competes with the magnetic order in the system. Due to the finite temperature in the system, there are also unbound holes present in the mixD system. These still considerably decrease the spin correlations. The linear fits highlight the different slopes, which clearly distinguish between the mixD and the standard system. This not only hints at the pairing mechanism, but also demonstrates the considerable mobility of holes along the system.

We note that the mixed-dimensionality should be of minor effect in the undoped case, yet the rung spin correlations of the mixD and standard ladders differ significantly for the undoped system. We attribute this to heating in the mixD system caused by the quenched optical potential offset.

Fig. 4.21b shows the numerically simulated rung spin correlation strength for the mixD system at very low temperatures of $k_B T = 0.1 J_\perp$. There we see a strong even versus odd effect, with odd numbers of holes leading to weaker correlations than even numbers of holes. The explanation is that odd numbers of holes cannot pair up, there will always be one hole left without a pair. This unpaired hole disturbs the spin environment. Even though it is not expected at our temperatures, the experimental data shows an onset of this behavior with a significant tick-tack pattern at low doping. This might be another indication that our system is not well described by a single temperature value. We do, however, not see this behavior at higher doping.

We furthermore want to investigate the dependence of pairing strength on spin correlations. For this, we make use of the temperature drifts of our system and the time-dependent average rung spin correlations that we have assigned to our data. In Fig. 4.22, we plot the rung hole correlations $g_h^{(2)}(0,1)$ for different singlet strengths, which we have summarized in discrete bins. We see that the pairing in the mixD system becomes significant around $C(0,1) = -0.3$, or a temperature of about $k_B T = 1 J_\perp$. The rung spin correlations then increase with increasing spin correlations. Since the spin correlations are directly related to the temperature of the system, this is equivalent to an increase in ground state fraction with decreasing temperature. The highest reached correlations of $g_h^{(2)}(0,1) = 0.3(1)$ are however still smaller than the theoretically achievable $g_h^{(2)}(0,1) > 1.2$ for very low temperatures. This demonstrates that our system, despite the large boost in binding energy, still displays significant temperature limitations.

In the standard system, however, we do not see such a strong temperature dependence in our regime. This is because the repulsion between holes is governed by the energy scale of the tunneling $t_\perp \gg k_B T$, while pairing is governed by the spin exchange $J_\perp$.

The mobility of holes in the system is not only visible by unpaired holes breaking singlet bonds, but can also be seen in the antiferromagnetic spin pattern along the leg. This pattern gets stretched when holes, and especially hole pairs, move along the lad-
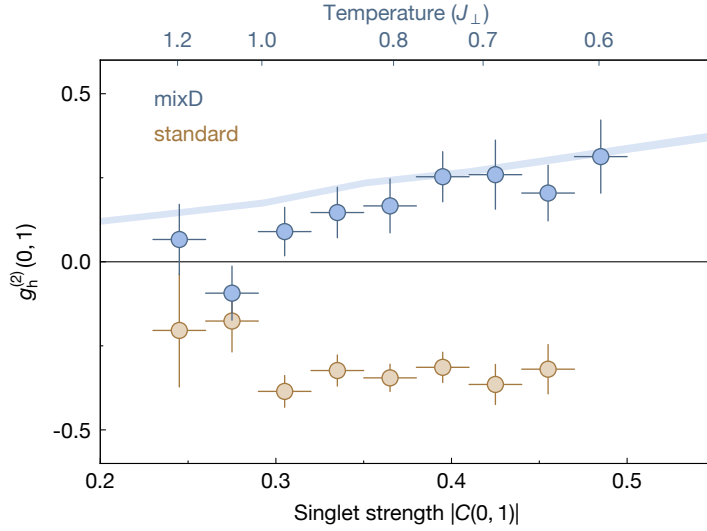
Figure 4.22: Thermal unbinding of pairs. Rung hole correlations $g_{\mathrm{h}}^{(2)}(0,1)$ for the mixD (blue) and standard (brown) ladders binned by the rung spin correlations $C(0,1)$. The temperature of the mixD system (top axis) is estimated by comparing the spin correlations (lower axis) to theoretical values. The solid line is calculated using MPS and corrected by the experimental detection fidelity. We see unbinding of pairs at low singlet strength, i.e. high temperature. Error bars denote one s.e.m.

der. This process is comparable to spin-charge separation in one dimension. A map of spin correlations around a hole pair is shown in Fig. 4.23a. The spin pattern shows a π phase shift at the position of the hole pair. In a perfect antiferromagnet, the nearest-neighbor bonds (distance $d_x = 1$) are negative, while the next-nearest-neighbor bond ($d_x = 2$) is positive, and the $d_x = 3$ bond is negative again. However, when a hole pair moved through this pattern, it stretches the pattern at the location of the pair and reverses the sign of the spin correlations. The nearest neighbor bond then becomes a next-nearest neighbor bond, which is indeed negative across the holes (bond 'C' in Fig. 4.23a). Furthermore, the distance $d_x = 3$ bond ('D') is positive, which is also consistent with a stretched antiferromagnetic pattern. This clearly demonstrates the mobility of the hole pair along the legs of the system, as opposed to a localized rung pair, which merely cuts the system into two uncorrelated sides.

4.8   Pair interaction

In the following, we investigate the behavior of several hole pairs in the system. The interplay of these bosonic objects is a key aspect of the emergence of superconductivity, which stands in competition with charge-density ordered states. In order to shed light on their origin, we observe the interaction between pairs in our system.

In the following, for simplicity, we will identify pairs as two holes occupying the same rung. This is justified by the hole correlations indicating that the short-ranged pairs
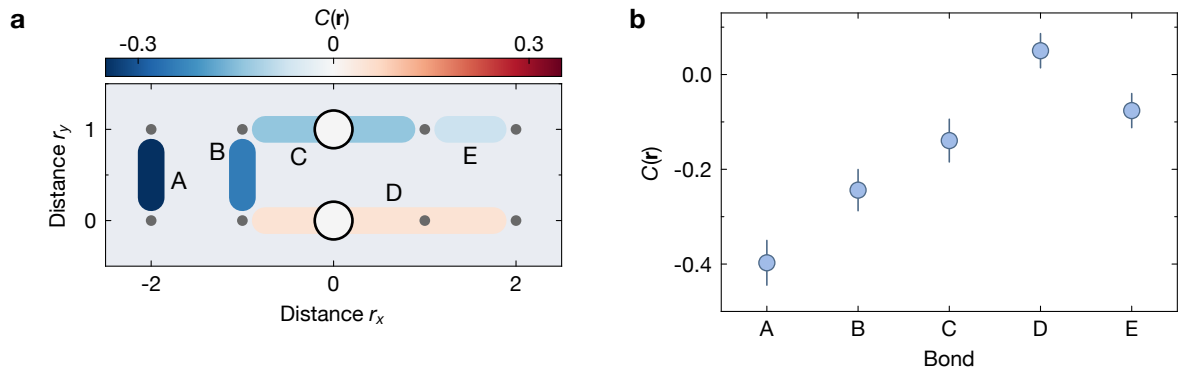
Figure 4.23: Spin correlations around a hole pair. a, Map of spin correlations around a hole pair in the mixD system. The colored bonds indicate the strength of the spin correlator, and the endpoints of the bonds represent the position of the correlated sites in the frame of the hole pair. For example, bond C denotes the spin correlation of next-nearest-neighbors across a hole pair. The data used for the analysis includes up to four holes, but no leg imbalance in the system. **b**, Quantitative values corresponding to the bonds shown in **a**. The error bars denote one s.e.m.

in our mixD system predominantly occupy one rung. We quantify pair interactions using the pair-pair correlator

$$
g_{\text{pair}}^{(2)}(d) = \frac{1}{\mathcal{N}_d} \sum_x \left(\frac{\langle \hat{n}_x^{\text{p}} \hat{n}_{x+d}^{\text{p}} \rangle}{\langle \hat{n}_x^{\text{p}} \rangle \langle \hat{n}_{x+d}^{\text{p}} \rangle} - 1 \right), \tag{4.7}
$$

where we have defined the pair operator $\hat{n}_x^{\text{p}}$, which is equal to 1 if both sites of rung x are occupied by a hole, and 0 otherwise. The pair operator $g_{\text{pair}}^{(2)}$ is analogous to the hole operator $g_{\text{h}}^{(2)}$ within a single leg and we thus apply the same finite size offset correction that was introduced in Eq. (4.4).

To evaluate the $g_{\text{pair}}^{(2)}$ correlator, we consider the sub-set of our data which contains at least two rung pairs. Fig. 4.24a shows the $g_{\text{pair}}^{(2)}$ correlator for ladders in this subset, which in total contain between four and five holes. We find a peak at distance $d = 4$, meaning that our pairs preferably have a mutual distance of four sites. This is the maximal distance two pairs can assume without occupying the energetically expensive system edge. The data points, however, have large error bars and the result does not show clear statistical significance.

Fig. 4.24b shows the pair density in the system extracted from numerical simulations. At low temperatures we see a clear maximum density at sites $x = 1$ and $x = 5$, corresponding to a distance of $d = 4$, consistent with the experimental results. This can be explained by pairs repelling each other. Since pairs lower their kinetic energy by delocalizing, it is energetically expensive to be close to other pairs. At higher temperatures, the signal washes out.

The density modulation caused by the interaction of pairs becomes more prominent

Figure 4.24: Distribution of two rung hole pairs in the mixD ladders. a, Measured pair-pair correlation $g_{\text{pair}}^{(2)}(d)$ of rung hole pairs in the experimental system for 4-5 holes, i.e. not more than two pairs per ladder. Error bars were estimated using boot-strapping. **b**, Theoretical (MPS) results for the density of rung pairs in the system for temperatures from $0.1\,J_\perp$ to $0.7\,J_\perp$ and four holes in the system. The pairs maximize their respective distance, while also avoiding the edge of the system.

when there are more holes in the system. A system of length $L = 7$ containing three pairs shows a strong density pattern, because there there is a unique pattern that avoids occupation on the edge of the system as well as pairs neighboring each other. The optimal configuration is an alternating pattern of spins and holes, as illustrated in the sketch of Fig. 4.25a. The corresponding plot shows the $g_{\text{pair}}^{(2)}$ correlator for ladders containing between six and seven holes. We see a significant modulation, with peaks at distance $d = 2$ and $d = 4$, consistent with the aforementioned pair distribution. The numerically simulated pair density shown in Fig. 4.25b shows a density pattern which as well is consistent with the experimental result. It shows high density of pairs on sites $x = 1$, $x = 3$ and $x = 5$, corresponding to pair distances of $d = 2$ and $d = 4$. This visibility in the pair density is a direct consequence of the open boundary conditions, because the presence of sharp edges fixes the phase of the density modulation.

Both the experimental system and numerical simulations display a spatial structure where pairs maximize their mutual distance. This repulsion between pairs is an indication of the comparably high mobility of pairs in mixD settings, which could be further enhanced by increasing the leg tunneling $t_\parallel$ in larger systems. Such highly mobile pairs can potentially reach very high critical temperatures [221], and can be an important ingredient for high-T_C superconductivity.

The observed charge-density modulation of the pair distribution is reminiscent of Friedel oscillations of indistinguishable fermions near an impurity [228], as well as of charge-density-waves [229]. In our system of size $L = 7$ we cannot distinguish these two phenomena, because we cannot see if the density modulation is of long range, as in charge-density-waves, or if it quickly decays with distance like Friedel oscillations. Larger systems are needed to distinguish between these effects.
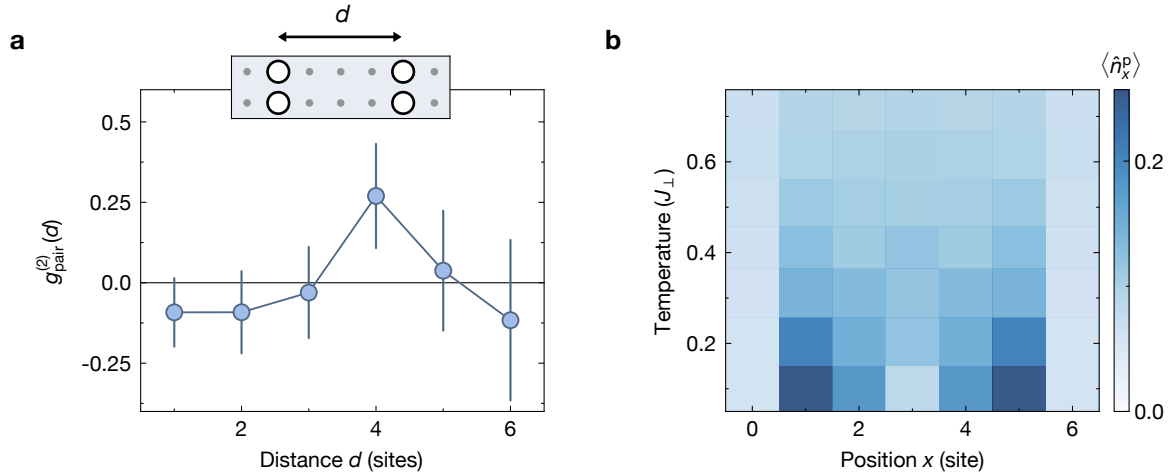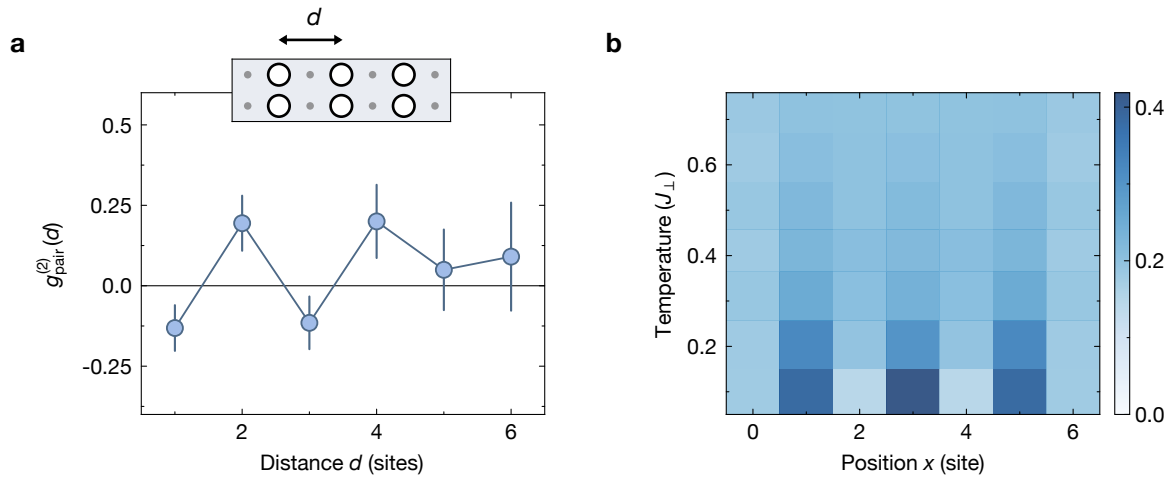
Figure 4.25: Distribution of three rung hole pairs in the mixD ladders. a, Measured pair-pair correlation $g_{\mathrm{pair}}^{(2)}(d)$ of rung hole pairs in the experimental system for 6-7 holes, i.e. up to three pairs per ladder. Error bars were estimated using bootstrapping. **b**, Theoretical (MPS) results for the density of rung pairs in the system for temperatures from $0.1\,J_\perp$ to $0.7\,J_\perp$ and six holes in the system. The pairs maximize their respective distance, while also avoiding the edge of the system.

We investigate the distinction between these two phenomena theoretically, by performing MPS calculations for larger system sizes. Fig. 4.26a shows the pair density of a system of size $L = 15$ for different doping. We see that the wavelength of the density modulation is doping-dependent, similar as in the experimental system. The amplitude is strongest at the edge and slightly decays towards the center of the system. This is explained by the edge pinning the phase of the modulation. We do not see a settling of this decay within this system size. Fig. 4.26b shows the pair density of a system of size $L = 50$ for a doping of 20%. The density pattern is most pronounced at the edge of the system. After an initial decay, the amplitude stays rather constant within the bulk of the system. We believe that this behavior is representative of the thermodynamic limit, where we expect a charge-density wave to form.

4.9 Discussion

We have experimentally shown that magnetically mediated pairing exists in Fermi-Hubbard-like systems. This emphasizes the relevance of magnetic correlations as a potential origin for the pairing underlying high-T_C phases. Furthermore, by demonstrating a strongly increased binding energy, the experiment confirms that the effective mixD description is accurate. This is important, as for example higher-order processes in the many-body system could modify the effective Hamiltonian significantly at a finite U/t and Δ/t. We hope our demonstration motivates material scientists to engineer materials with high binding energy by following the mixD route, and thus potentially reach higher critical temperatures.

a

b
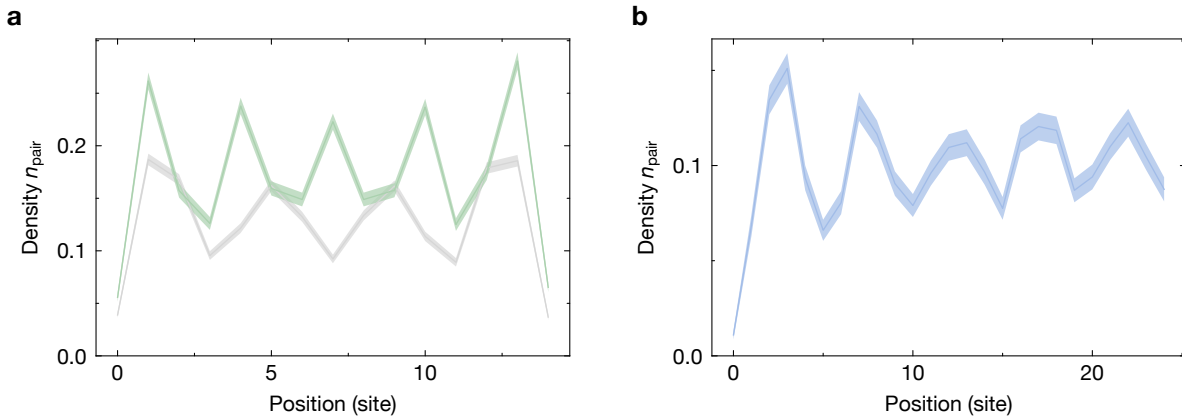
Figure 4.26: Hole-hole correlation in the standard ladder. a, Pair density n_{pair} of a system of size $L = 15$ at $k_{\text{B}}T = 0.1\, J_\perp$ for eight holes (grey line) and ten holes (green line) calculated using MPS. **b**, Pair density n_{pair} in the ground state for a system of length $L = 50$ and a doping of 20 % calculated using DMRG. Shaded areas denote one s.e.m.

4.9.1   System extensions

There are several possible ways in which our studies could be extended. As discussed earlier, higher leg coupling $t_\parallel$ leads to even higher binding energies. It, however, also comes at the cost of larger pair sizes. The small pair size is essential for our study in order to have a separation between system size and pair size. This allows us to approximate the physics of the thermodynamic limit despite the short length. If the pair size, however, becomes comparable to the system size, finite size effects become dominant. Eventually the pair cannot be distinguished from free holes. It thus needs larger systems to investigate settings with higher binding energy. The experimental apparatus is currently under reconstruction and larger system sizes might be achieved soon.

Another direction to follow up on this work is the extension to mixD bilayer systems using bilayer quantum gas microscopes [55–57]. The system hosts pairs with strong mobility in two dimensions and displays a BEC and a BCS regime which is tunable via controlling the doping [221]. Instead of extending the system orthogonal to the suppressed tunneling and creating a mixD bilayer system, one can also extend the system in the direction of the suppressed tunneling. This leads to a two-dimensional mixD system with suppressed tunneling in one direction. This kind of system features robust stripes that form collective charge-density waves [230]. In general, systems that go substantially beyond the two-leg ladder become very hard to simulate with numerical methods. Thus quantum simulation of mixD models of higher dimensions can have a computational advantage over classical computation.

4.9.2   Perspective on real materials

Since pairing is a prerequisite for superconductivity, it sets an upper bound for the critical temperature. The pairs in mixD systems like the one we have demonstrated

display high mobility, which can be increased even further by increasing $t_\parallel$. This high mobility in the mixD system, together with the extremely high binding energy, can potentially lead to very high critical temperatures [221]. We have thus experimentally shown a new route that not only boosts the binding of dopants but also has the potential to increase the critical temperature for superconductivity.

For our findings to have implications for real superconductors, one needs to find ways to modify the interplay of kinetic and exchange energies in solid state systems. One way to suppress the kinetic energy without suppressing the super-exchange interaction might be achieved by changing the lattice geometry and spin polarization. For example, in a weakly doped system of fermions on a triangular lattice, the kinetic energy of holes becomes geometrically frustrated, and hence strongly suppressed, in the regime of strong spin polarization [231]. In moiré systems, such as twisted graphene, one often finds systems that include a combination of flat and broad bands. One can control the kinetic energy and topology of electrons in the narrow band by varying the twist angle. On the other hand, magnetism of electrons in the narrow band may be dominated by interaction with electrons in the wider bands [232]. Furthermore, there already are reports of materials like the ladder compound $Sr_{14}Cu_{24}O_{41}$, that display effects which resemble the results in our mixD system [233, 234]. These observations might be explained by very similar underlying physics, and if so constitute an example of a material realization of our approach.

Our mixD setting might also be realized in an approach more closely related to our experimental technique, which probes pairing in a metastable state. One example is to use Floquet engineering to alter the effective exchange interactions in magnetic materials, as suggested, for example, in [235]. We thereby also open new regimes for dynamical superconductivity.

A symmetry-protected topological phase in Fermi-Hubbard ladders

In this chapter we present the experimental realization of the symmetry-protected Haldane phase using antiferromagnetic Fermi-Hubbard ladders in our quantum gas microscope. The results of this project are partially covered within this PhD thesis, other parts will be covered in a future PhD thesis due to the shared work on this project. After introducing the relevance and advantage of investigating the Haldane phase microscopically, we explain the preparation sequence and characterize the system. We then go on to compare the string order parameters for the topological and trivial phase and we investigate the system dependencies on system size and coupling parameters. We furthermore detect and characterize the edge states of the system and last but not least demonstrate an alternative realization of the Haldane phase involving ferromagnetic coupling along the rungs of the ladders. The numerical DMRG results presented in this chapter were calculated by Julian Bibo and Ruben Verresen.

5.1   The Haldane phase under the microscope

The study of topological phases has gotten great attention in the last years, including a Nobel prize "for theoretical discoveries of topological phase transitions and topological phases of matter" [236] in 2016, partially given to D. Haldane, who gives his name to one of the most paradigmatic topological phases, the Haldane phase. This symmetry-protected topological (SPT) phase appears in antiferromagnetic spin-1 chains and is characterized by short-range magnetic correlations, a spin gap in the bulk and fourfold degenerate spin-1/2 edge modes. The topological nature manifests itself in a non-local long-range order parameter, which can be probed using string operators.

Early solid state measurements on spin-1 chains, though not resolving the edge states, found evidence for the fractional spin-1/2 edge modes, as well as a bulk spin gap using neutron scattering [237] and electron resonance experiments [238, 239] on solid state materials. However, in order to reveal the non-local string order parameter, access to the local spin states is required. This can only be achieved by detecting the quantum many-body system with microscopic resolution. Quantum gas microscopy thus offers a rich diagnostic tool to detect the string order and gain further inside into such quantum phases of matter. A recent study has demonstrated these possibilities, realizing an SPT phase in the Su-Schrieffer-Heeger (SSH) model of hardcore bosons
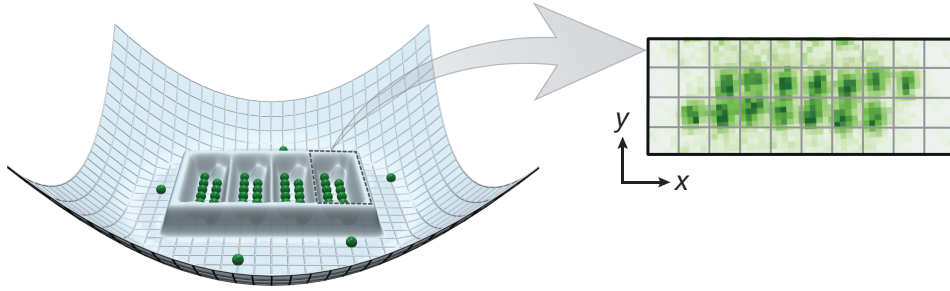
Figure 5.1: Ladder potential and snapshot in topological configuration. The figure shows the optical potential that is created from overlapping the DMD pattern and the optical lattices. We create four mutually disconnected ladder systems next to each other in each experimental run in order to increase statistics. The ladders are surrounded by a low density region which acts as a particle and entropy bath. An experimental snapshot of a single ladder is shown on the right. The boundaries of the ladder are not situated on a single rung, but show a tilted edge. This is achieved by blocking one site of the outermost rung using the DMD potential.

by using Rydberg atoms in optical tweezers [240]. In our setup, we can implement the Haldane phase based on antiferromagnetic spin-1/2 ladders, an approach that is conceptually close to the AKLT model. Such simple models help to visualize the microscopic structure of the Haldane phase and reveal the mechanisms leading to its characteristics, like the spin-1/2 edge states that emerge naturally from the spin-1/2 building blocks of our system. The implementation using ultracold atoms furthermore allows for a wide tuning range of coupling parameters and system sizes. We can thus study the system in different regimes, and contrast it to the trivial phase under the same experimental conditions and parameters.

5.2   System preparation

In our quantum gas microscope, we simulate Fermi-Hubbard two-leg ladders in the Heisenberg regime with antiferromagnetic couplings. By combining diagonal pairs of spins into unit cells, we effectively simulate an integer spin chain. This integer spin chain is adiabatically connected to the antiferromagnetic spin-1 chain and thus displays the same quantum phase in its ground state - the Haldane phase. The unit cell definition and the relation to the Haldane phase are discussed in details in section 2.6).

To prepare the system, we load a cold cloud of a balanced mixture of the two lowest hyperfine states of ^{6}Li in a single plane of our vertical optical lattice. We then adiabatically ramp up the optical lattices in xy-direction within 100 ms. Simultaneously, we ramp up a repulsive optical potential created using our DMD. This repulsive pattern compensates for the harmonic confinement of the lattice beams and shapes the two-leg ladder potential, as it is illustrated in Fig. 5.1. The ladder potential has a special *tilted* edge termination, which can be seen in the example shot in the same figure. The

length L (sites)	hopping $t_\parallel/h$(Hz)	hopping $t_\perp/h$(Hz)	interaction U/h(Hz)	ratio $J_\perp/J_\parallel$
5,6,7,9,11	250	280	3500	1.3(2)
5	330	38	4000	0.013(2)
5	300	130	3600	0.20(3)
5	340	280	3000	0.7(1)
5	250	280	3500	1.3(2)
5	150	300	3500	4.0(6)
5	130	390	3300	8(1)

Table 5.1: Experimental parameters. The parameters system size L, leg coupling $t_\parallel$, rung coupling $t_\perp$, interaction U and the resulting ratio $J_\perp/J_\parallel$ are shown for all data sets. The uncertainties are given for $J_\perp/J_\parallel$ and originate from a 5% uncertainty on the hopping parameters $t_\perp$ and $t_\parallel$. For the length scan we keep all other parameters constant, whereas the $J_\perp/J_\parallel$ scan demands a tuning of both tunnelling amplitudes in order to keep both $U/t_\parallel$ and $U/t_\perp$ high. Where the topologically trivial geometry is realized, it has the same parameters as the topological geometry.

edge termination is chosen to reflect the diagonal unit cell definition. Only if edge termination and unit cell definition coincide, there is a well-defined unit cell on the boundary of the system and the edge modes of the phase can be studied. We note that because of the short-range entangled nature of SPT phases, the edge termination does not affect the bulk physics. We change the edge termination to a straight cut, when we realize the trivial phase of the straight unit cell. In the following we will refer to the tilted-edge configuration as the topological configuration, because we choose diagonal unit cells with this edge termination. Likewise, we refer to straight-edge configuration as the trivial configuration, because we use the straight unit cell definition for the system with straight edges.

We individually tune the lattice depths to realize different parameter regimes and choose the interaction strength in order to realize the approximate Heisenberg regime of the Fermi-Hubbard model. The lattice depths range between $5\,E_R$ and $15\,E_R$, while the scattering length has up to $1200\,a_B$ and is adjusted using the broad Feshbach resonance of ^{6}Li. Furthermore, we realize ladder of different length L to investigate the influence of system size. Table 5.1 shows the parameters of the different data sets.

The optical potential shaping of the ladder system is separately adjusted for the different coupling parameters, because of the dependence of the harmonic confinement on lattice depth. The procedure to achieve a flat potential within the ladder areas consists of several feedback iterations. In each iteration we prepare systems with about 20% doping and average between 100 and 150 experimental shots, which we use as feedback to the DMD pattern. We however note that system inhomogeneities on the order of the tunneling strength are much smaller than the interaction energy U associated with doublon excitations. The inhomogeneities thus do not significantly affect the physics in the undoped Heisenberg regime, since the system stays incompressible and the corrections to the spin exchange energy (see Eq. (4.1)) are small.

At the end of the experimental sequence, we freeze the atomic configuration by ramp-
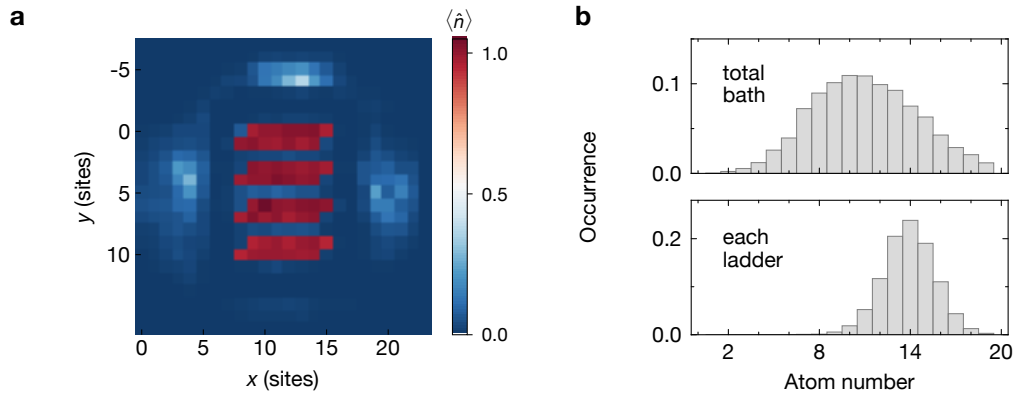
Figure 5.2: Density and atom number distribution. a, The figure shows the density of the tilted-edge system at length $L = 7$ and is averaged over about 7500 single snapshots. The four ladders are surrounded by a bath of low atomic density. **b**, shows the normalized histograms of atom numbers in the bath region (upper plot) and in each ladder (lower plot) for the data set of **a**. The atom number fluctuations in the bath are, despite the lower average number, considerably higher than inside the ladders. Almost one out of four ladders is half-filled with total atom number $N = 14$.

ing the $xy-$lattices to $43\,E_{\mathrm{R}}^{xy}$ within $250\,\mu\mathrm{s}$. We then take spin resolved images with an imaging time of $2.5\,\mathrm{s}$ and a detection fidelity per atom of $96(1)\,\%$. We estimate this detection fidelity by taking two subsequent images of the same atomic cloud and comparing the occupation, combined with the pumping fidelity of our spin resolution technique.

Data selection

In order to probe the physics of the Heisenberg model, we need to work at 0% doping. We thus postselect our data for exactly half-filling, meaning an occupation of $2L$ particles per ladder. Furthermore, we allow up to one doublon hole pair in the system and restrict the total magnetization per ladder to $M^z = 0$ or $|M^z| = 1$ and specify the magnetization sector for each data point presented. Unless otherwise specified, these restrictions hold for all experimental data presented within this chapter, except density plots, which contain no postselection.

5.3   System characterization

The tailored potential yields a homogeneous filling of the system with sharp boundaries. The main data set, the measurement of the topological configuration at length $L = 7$ unit cells, displays a remaining density variance over the system of 2×10^{-4} without postselection on atom number (see Fig. 5.2a). The bath region surrounding the ladders acts as a buffer for fluctuations of the total atom number, as shown by the histograms in Fig. 5.2b. As a result, almost one fourth of the ladders in the main data

a

b
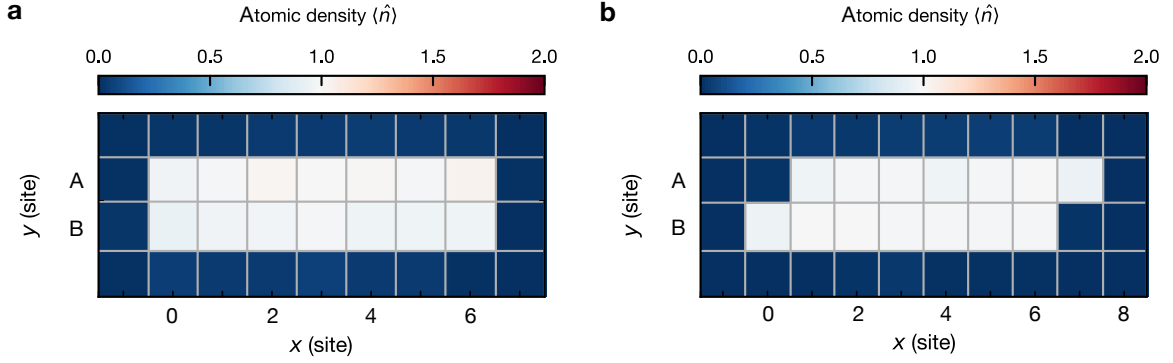
Figure 5.3: Average density of the topological and trivial configurations. The figure shows the average atomic density of the topological, tilted-edge configuration (**a**) and of the trivial, straight-edge configuration (**b**) for length $L = 7$ unit cells.

set have a total atom number $N = 2L$. The total magnetization $|M^z| \leq 1$ for 87.5 % of all ladders.

The trivial and topological configurations are realized with the same experimental parameters and length in unit cells. They thus show a similar system flatness and atom number distribution. Fig. 5.3 shows the average density profile of the trivial and topological ladders at length $L = 7$. To extract the temperature of our atomic system, we compare the measured spin correlations $C(d)$ to numerical calculations from exact diagonalization (ED) of the Heisenberg model at finite temperature. We find a temperature of $k_B T \approx 0.9(3) J_\parallel$ for the data set of length $L = 7$. Note, however, that we realize different coupling parameters $J_\perp / J_\parallel$ at length $L = 5$, whose temperature value is consequently not constant in terms of $J_\parallel$. We thus give our temperature in entropy per particle S/N, which stays roughly constant at $S/N = (0.3 - 0.45) \, k_B$ over the different coupling parameters.

Fig. 5.4a shows the nearest-neighbor spin correlation strength $C(1)$ along rung and leg of the ladders for different $J_\perp / J_\parallel$. The spin correlations along the rung vanish for very small rung coupling $J_\perp \to 0$, while the spin correlations along the leg have their maximum of $C(1) = -0.50(1)$ in this configuration. As the rung coupling increases with respect to the leg coupling, the correlations increase along the rung and decrease along the leg. At $J_\perp / J_\parallel = 8$ the rung spin correlations reach $C(1) = -0.58(1)$. From these spin correlations, we estimate the singlet fraction along the rungs by assuming that the system is $SU(2)$ symmetric. This means, in particular, that the three triplet states $|\uparrow\uparrow\rangle$, $|\downarrow\downarrow\rangle$, and $|\uparrow\downarrow\rangle + |\downarrow\uparrow\rangle$ all appear with the same probability, and the probability of the $|\uparrow\downarrow\rangle + |\downarrow\uparrow\rangle$ state can be derived from the observed probability of $|\uparrow\uparrow\rangle$ and $|\downarrow\downarrow\rangle$ states. This means the rung singlet fraction can be calculated as

$$p_{\text{sing}} = \frac{p_0 - 0.5 p_1}{p_0 + p_1},$$

where p_0 (p_1) is the fraction of rungs with total rung magnetization $m^z(x) = 0$ ($|m^z(x)| = $
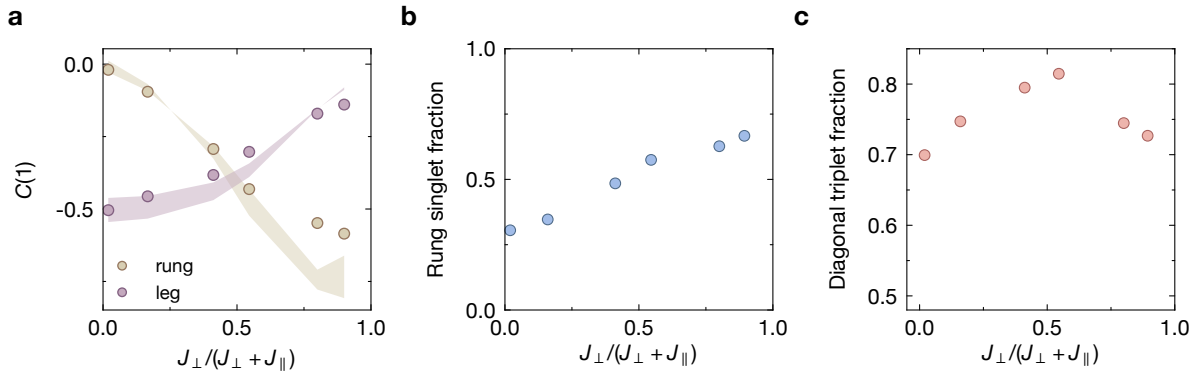
Figure 5.4: Spin correlations and singlet fraction. a, Nearest-neighbor spin correlations $C(1)$ along the rungs and legs of the system of length $L = 5$ for different coupling parameters $J_\perp / J_\parallel$. The shaded areas correspond to the correlations in the Heisenberg model with an entropy per particle of $S/N = (0.3 - 0.4) k_B$. The **b**, Experimentally estimated singlet fraction along the rungs of the system (see text). **c**, Experimentally estimated triplet fraction in the diagonal unit cells (see text). While the singlet fraction continuously increases with the rung coupling, the triplet fraction peaks at comparable coupling $J_\perp \approx J_\parallel$. The x-axes of **a**,**b**,**c** are given as $J_\perp / (J_\perp + J_\parallel)$, which in the limit of uncoupled chains is zero and in the limit of uncoupled rungs is one. The results are obtained from the magnetization sector $M^z = 0$. Error bars denote one s.e.m. and are smaller than the markers if not visible.

1), where the total rung magnetization $m^z(x)$ is defined as

$$m^z(x) = m^z_{x,A} + m^z_{x,B}. \tag{5.1}$$

Similarly, the unit cell triplet fraction can be calculated from the unit cell singlet fraction. Fig. 5.4b and c show the rung singlet and unit cell triplet fractions calculated under this assumption. We see that the singlet fraction continuously rises with increasing rung coupling and reaches almost 70% in the large rung coupling regime. The triplet fraction, on the other hand, has its maximum of above 80% around the point of isotropic coupling $J_\perp \approx J_\parallel$. We note that, even though our system does not represent a purely spin-1 chain, we can simulate the physics of the Haldane phase. The adiabatic mapping of the spin-1/2 ladder onto the antiferromagnetic spin-1 chain ensures that the ladder system realizes the Haldane phase despite the presence of a finite singlet fraction [101].

5.4   Signatures of the topological and the trivial phase

In order to investigate the signatures of the Haldane phase, we measure the correlations in the bulk. For this we use the definition of the k-th unit cell, which is given by the diagonal sites $(k + 1,A)$ and (k,B) in the topological configuration, and vertical sites (k,A) and (k,B) in the trivial configuration.

One of the characteristic properties of the Haldane phase is the short-range nature of

a

b
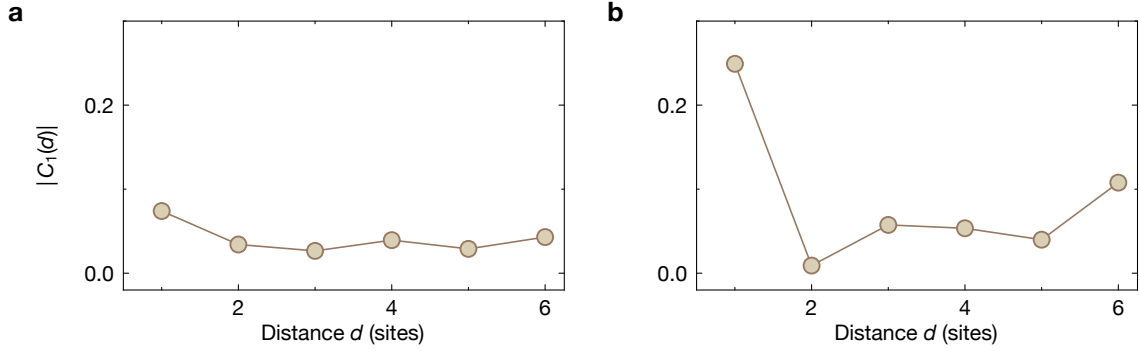
Figure 5.5: Short-range unit cell spin correlations. The unit cell spin correlations $C_1(d)$ are plotted for the trivial (topological) configuration in **a** (**b**) of length $L = 7$. The trivial configuration displays low spin correlations independent of distance d. The topological configuration features strong nearest-neighbor correlations, which decay quickly with distance. At the maximum distance $d = 6$, which corresponds to the correlation between the unit cells at the edge of the system, the correlation is partially revived. The figure contains data of magnetization sector $M^z = 0$.

spin correlations

$$C_1(d) = g_{S^z, \mathbb{1}} = \frac{1}{\mathcal{N}_d} \sum_x \langle \hat{S}_k^z \hat{S}_{k+x}^z \rangle, \tag{5.2}$$

which correlates the integer spin values between different unit cell positions. These are plotted versus distance d in Fig. 5.5. Both systems show short-range or vanishing correlations. The trivial configuration, which largely consists of spin-0 unit cells, shows low correlation values at all distances. The topological configuration with its majority spin-1 unit cells displays strong antiferromagnetic nearest-neighbor correlations, which drop sharply with distance. At maximum distance $d = 6$ the correlation value rises again. This corresponds to the correlation between the two edges of the system. This can be explained by the bulk-edge correspondence: The bulk of the Haldane phase has vanishing magnetization due to the singlet bonds between the spin-1. At total magnetization $M^z = 0$ the spin-1/2 edge modes thus need to have opposite spin states. The observation of the correlation between the edge unit cells thus indicates the existence of edge states. We will investigate these edge states later, and for now focus on the correlations in the bulk.

5.4.1   Measurement of the string order parameter

We have just seen that the spin correlations are vanishing in the bulk of both the topological and the trivial configuration. However, there still is a hidden long-range AFM order in the bulk of the topological configuration, which can be made visible
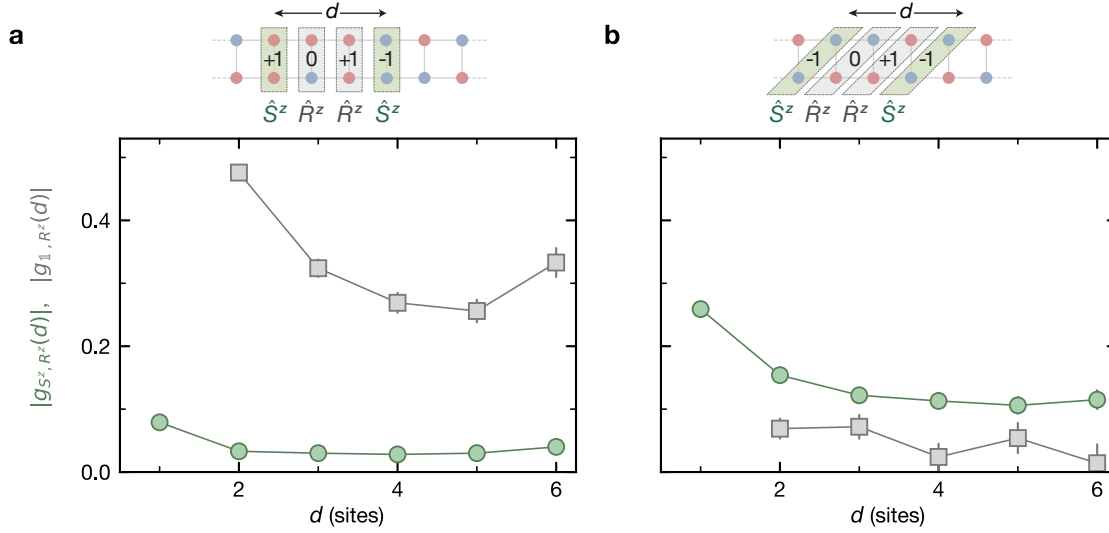
Figure 5.6: String correlators in the trivial and topological configuration. The figure shows the measured string correlators $g_{S^z,R^z}(d)$ (green circles) and $g_{\mathbb{1},R^z}(d)$ (grey squares) in our experimental system for the trivial (**a**) and topological (**b**) configuration and length $L = 7$. The comics above the plots illustrate the string correlation measurement in the trivial and topological unit cells. The measurement is averaged over about 2500 ladder instances with total magnetization $M^z = 0$. Error bars denote one s.e.m. and are smaller than the markers where they are not visible.

with the string order parameter

$$g_{S^z,R^z}(d) = \left\langle \hat{S}_k^z \left(\prod_{l=k+1}^{k+d-1} e^{i\pi\hat{S}_l^z} \right) \hat{S}_{k+d}^z \right\rangle , \qquad (5.3)$$

which corresponds to the general string correlators defined in Eq. (2.14) with endpoint correlator $\hat{O}_k = \hat{S}^z$ and bulk transformation under $\hat{U}_l = \hat{R}_l^z \equiv \exp\left(i\pi\hat{S}_l^z\right)$. This string correlator reveals the hidden order by effectively evaluating spin correlations in squeezed space. unit cells of spin $S_k^z = 0$ are neglected and only those unit cells containing spin $S_k^z = \pm 1$ contribute to the correlator. In Fig. 5.6a we have evaluated this correlator for the straight unit cells of the trivial configuration. The string correlation values and its distance dependence are very similar to the local spin correlation values $C_1(d)$ and we have thus not revealed a hidden order in the trivial configuration. In the topological configuration, however, we find a non-zero correlation that does not decay substantially over the whole system (see Fig. 5.6b). This is in stark contrast to the short-ranged spin correlations observed in this system. The correlator reveals the hidden AFM order, which is characteristic for the Haldane phase.

We furthermore evaluate the pure-string correlator

$$g_{\mathbb{1},R^z}(d) = \left\langle \hat{\mathbb{1}}_k \left(\prod_{l=k+1}^{k+d-1} e^{i\pi\hat{S}_l^z} \right) \hat{\mathbb{1}}_{k+d} \right\rangle , \qquad (5.4)$$

with trivial endpoint correlator $\hat{\mathcal{O}}_k = \hat{\mathbb{1}}_k$. This correlator is non-zero at $d \gg 1$, if the edges do not have half-integer spins [195]. Consequently, this string correlator is non-zero in the topologically trivial configuration, and vanishes for large distances in the topological configuration. Thereby, the pure-string correlator reveals symmetry fractionalization in the topological configuration.

The measured correlation values for the pure-string correlator are plotted in Fig. 5.6 together with the string order parameter $g_{S^z,R^z}(d)$. As expected, this correlator is non-zero in the trivial configuration and almost vanishes in the topological configuration. This opposite behavior of the two different string correlators identifies the Haldane phase and distinguishes it from the topologically trivial phase, which is also clearly identified by the behavior of the two string correlators. We note that the magnitudes of the two correlators differ, because the endpoint correlator $\hat{\mathcal{O}}_k = \hat{\mathbb{1}}_k$ by definition is normalized to one, while $\hat{\mathcal{O}}_k = \hat{S}^z$ shows lower value even in a perfect spin-1 chain due to the contribution of $m^z = 0$ unit cells.

5.4.2 Coupling parameter dependence

In the following we investigate the dependence of the system with regard to variations in the coupling ratio $J_\perp / J_\parallel$. The SPT phase is expected to maintain the charge gap in the bulk of the system and be robust for all $0 < J_\perp, J_\parallel$ [101]. We measure both string correlators, the pure-string correlator $g_{\mathbb{1},R^z}(d)$ and the spin string correlator $g_{S^z,R^z}(d)$ at maximum distance $d = L - 1$ in systems with different couplings and for both configurations (see Fig. 5.7). The pure string correlator behaves qualitatively very different in the two configurations and distinguishes the different phases. While it is consistent with zero everywhere in the topological configuration, it is significantly non-zero with monotonous slope in the trivial regime.

For the spin-string correlator the distinction between the two phases is less strong. In the trivial phase we observe lower correlation values than in the topological phase, but the evolution is very smooth. The charge gap becomes very small for small $J_\perp$ and thus the signal can barely be distinguished from the trivial phase for small rung couplings at our temperatures. In the topological phase, we find a maximum of the string correlation value around equal couplings $J_\perp \approx J_\parallel$ with decreasing values towards stronger rung couplings. This behavior is consistent with the zero temperature behavior in the thermodynamic limit and derives solely from the probability to find $m^z = 0$ at the endpoint and not from imperfections in the hidden AFM order [101].

The change of unit cell from the trivial to the topological configuration can be made a continuous transition with a suitable tuning parameter: In the trivial configuration, the rung coupling $J_\perp$ is reduced until the two legs of the ladder are effectively disconnected chains. At this point the coupling between the legs is increased again, but instead of coupling the two sites within the same unit cell, it is shifted in leg B by one site to the right and couples sites of neighboring unit cells. In the $J_\perp = 0$ limit the change of unit cell has no effect and we can draw a continuous phase diagram. The ED calculations result in smooth theoretical lines which corroborates our argument.
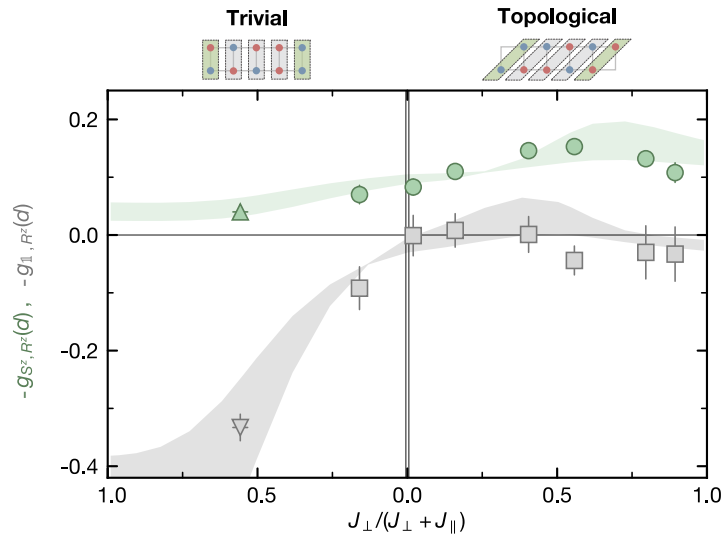
Figure 5.7: Influence of the spin coupling on the string order. The figure shows the dependence of the string order parameters $g_{S^z,R^z}(L-1)$ (green markers) and $g_{\mathbb{1},R^z}(L-1)$ (grey markers) on the coupling strength $J_\perp/J_\parallel$. The string order parameters are evaluated at the maximum distance $L-1$, thus stretching through the full system. The trivial (left) and topological (right) configurations can be understood as one continuously tunable system, connected via two uncoupled chains at $J_\perp = 0$. The shaded lines are Heisenberg ED results for an entropy per particle between $S/N = 0.3\,k_B$ and $0.45\,k_B$. The system has a length of $L = 5$ unit cells, except for the triangular markers, which are measured with a system length of $L = 7$ unit cells. All ladders have total magnetization $M^z = 0$. Error bars denote one s.e.m. and are smaller than the markers where they are not visible.

5.4.3 System size dependence

Our experimental system is relatively small and should not be considered to represent the thermodynamic limit. We argue, however, that we can still observe the characteristic signatures of the Haldane phase, which is vanishing local spin correlations and non-local string order due to symmetry fractionalization. Nevertheless, we want to investigate the effect of our small system size. For that we consider different system sizes up to length $L = 9$ using ED and up to length $L = 11$ experimentally.

As it can be seen in Fig. 5.8a, the ground state fraction decreases quickly with system size, even though the temperature is kept constant. The reason is that there are only four ground states, corresponding to the four edge states and one single state in the bulk, independent of the system length. At the same time the amount of excited states grows with the system length, and thus the probability with which one of them is populated. This means that our small system size is not a disadvantage for our experimental observation, but given our temperature it is necessary in order to achieve a convincing signal of the Haldane phase.

This is demonstrated in Fig. 5.8b, where we plot the spin string correlator, which is revealing the hidden AFM order. The plot shows that the string order is decaying
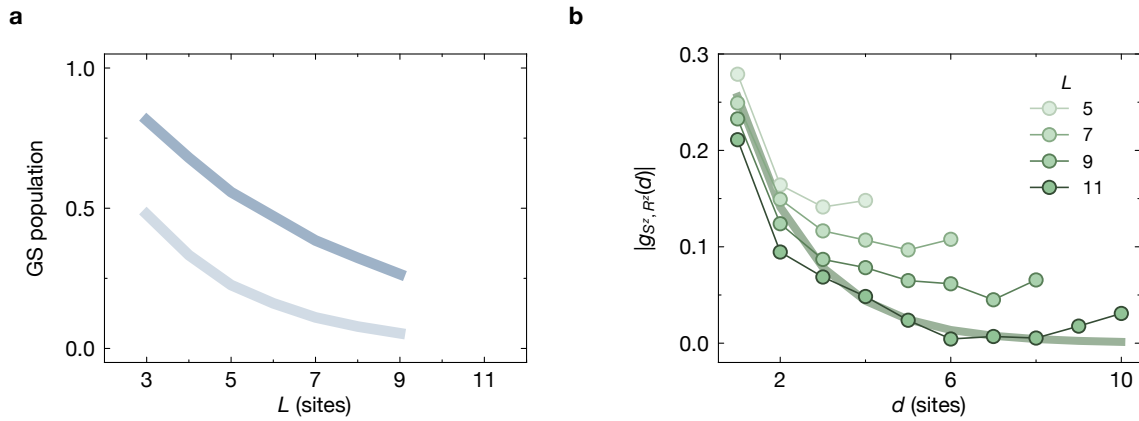
Figure 5.8: System size dependence. The figure shows the influence of system size on the ladders. **a**, Theoretical ground state (GS) fraction for a ladder system of length L with the diagonal edge termination and coupling strength $J_\perp / J_\parallel = 1.3$. The line in (light) blue is calculated using ED of the Heisenberg model at a fixed entropy per particle of $S/N = 0.3\,k_B$ ($0.45\,k_B$). The ground state population decreases despite the entropy per particle staying constant. **b**, The measured string order parameter $g_{S^z, R^z}(d)$ for systems of size $L = 5, 7, 9, 11$ in magnetization sector $M^z = 0$. Error bars denote one s.e.m. and are smaller than the markers where they are not visible. The shaded line shows finite temperature, infinite length calculations at our temperature of $k_B T = 0.9\,J_\parallel$ and coupling parameters $J_\perp / J_\parallel = 1.3$.

slower in smaller systems and seems to settle at different values for each length. At system size $L = 11$ the string order has decayed to a value consistent with zero at distance $d = 6$. At this length the shape of the string correlator versus distance is consistent with the shape in the thermodynamic limit at our temperature. Hence, at this length and this temperature, the system can not be said to display the signatures of the Haldane phase, because that would require a non-zero string order over the full system.

Length $L = 11$ is the maximum length we can realize experimentally due to the harmonic confinement of our lattices. For larger ladders we would need more power for our DMD, in order to compensate the harmonic confinement and still be able to project high barriers for the ladder potential. Length $L = 9$ was the maximum length we could calculate with ED at finite temperature and was limited by computational resources.

5.5 Edge states

We have already seen indications for the edge states when looking at the short-ranged spin correlations of Fig. 5.5b. These spin correlations vanish after few unit cells, but resurge in the correlation between the two edge states. This is due to the vanishing bulk magnetization and the selected magnetization sector $M^z = 0$. It thus directly
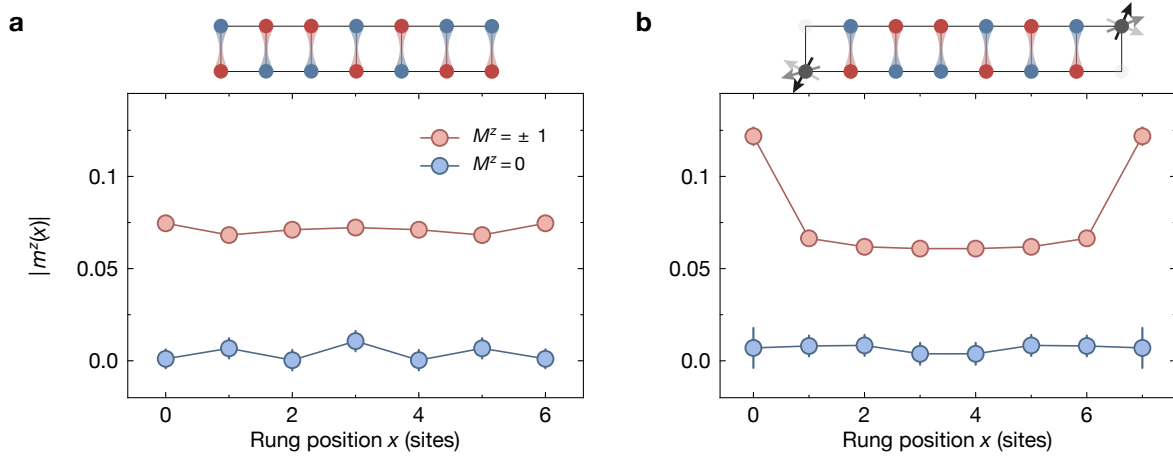
Figure 5.9: Average rung magnetization. We plot the average rung magnetization $m^z(x)$ as a function of position x in ladders of length $L = 7$. As illustrated by the comics above the plot, we measure ladder with straight (diagonal) edge termination in **a** (**b**). We measure both in the magnetization sector $M^z = 0$ (blue markers) and $|M^z| = 1$ (red markers). In the magnetization sector $|M^z| = 1$, we have averaged the magnetization $m^z(x)$ of sector $M^z = 1$ with the magnetization $-m^z(x)$ of sector $M^z = -1$. Error bars denote one s.e.m. and are smaller than the markers where they are not visible.

demonstrates the bulk-edge correspondence.

In the magnetized sector on the other hand, the edge states carry the excess magnetization, because the bulk has a strong singlet nature on the rungs. If the total magnetization is positive with $M^z = +1$, both edge modes thus carry an additional spin up. In the following we will investigate the edge states more thoroughly by analyzing the magnetization distribution in the total magnetization sector $|M^z| = 1$.

5.5.1   Detecting edge states

We reveal that the magnetization is rather located at the edge of the system by measuring the rung averaged magnetization $m^z(x)$ (see Fig. 5.9). For vanishing total magnetization we do not see a significant dependence of magnetization on the rung position. In the magnetized sector $|M^z| = 1$, however, the rung magnetization shows a clear dependence on the edge termination. While a straight-edge termination does not lead to a position dependent magnetization, the tilted-edge termination shows a localization of excess magnetization on the outermost rung. This signal comes from the edge states of the system. We can furthermore see a first indication for a position dependence of the magnetization within the bulk. Considering only the bulk of the system, magnetization decreases towards the center of the system, which is caused by the edge states not being completely localized on the edges, but penetrating into the bulk with a fast decay. This signal is, however, very small and overshadowed by an overall offset, which we attribute to the finite temperature of our system. Note that here we have not used the unit cell definition, because the edge magnetization is more
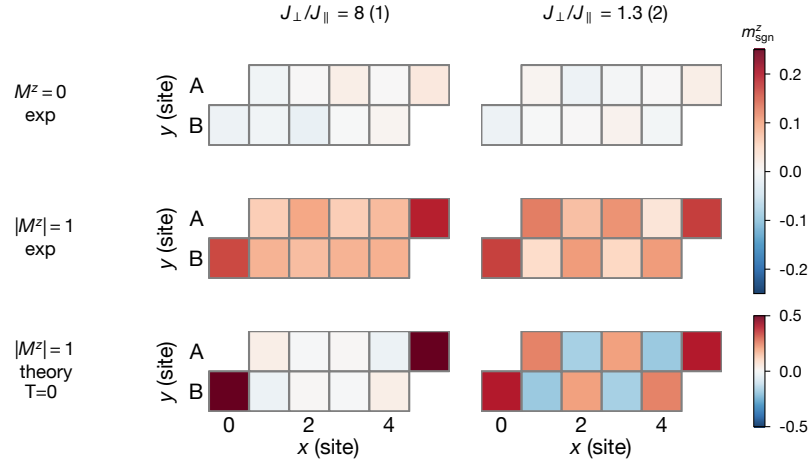
Figure 5.10: Spatial magnetization distribution in the tilted-edge ladder. Experimental magnetization maps $m^z_{x,y}$ are shown in the strong coupling regime $J_\perp/J_\parallel = 8(1)$ and the close to isotropic regime $J_\perp/J_\parallel = 1.3(2)$ for ladders of length $L = 5$. Ladders with total magnetization $M^z = 0$ doe not show a strong local magnetization, whereas ladders with total magnetization $|M^z| = 1$ display strongly magnetized edge sites and an alternating spin pattern for $J_\perp/J_\parallel = 1.3(2)$. The last row shows the theoretical magnetization at zero temperature calculated using ED. It is qualitatively similar to the experimental result, but with stronger edge magnetization and without a magnetization offset in the bulk.

striking when averaging over the singlets along the rung and the isolated excess spin on the very last site.

When considering the fully space resolved magnetization, one observes further structures in the ladder, which are hidden from the rung magnetization. Fig. 5.10 we show the magnetization maps of ladders at length $L = 5$ in the strong rung coupling regime $J_\perp = 8(1)J_\parallel$ and in the close to isotropic regime $J_\perp = 1.3(2)J_\parallel$. In the non-magnetized sector we find again no structure in the magnetization, except for system inhomogeneities, because bulk and edges both have magnetization zero. In the $M^z = \pm 1$ sector, however, we detect the strong magnetization on the edge sites of system. In the strong rung coupling regime the bulk displays a relatively homogeneous magnetization offset and a strong localization of the edge state, which does not visibly penetrate into the bulk.

In comparison, in the regime with similar rung and leg coupling, the magnetization map reveals an additional structure in the state. An alternating magnetization pattern appears that resembles antiferromagnetic correlations (with an additional total magnetization offset), but with a pinned orientation. The pattern arises due to the edge states being not fully localized on the outermost site, but leaking into the bulk with a certain localization length. The excess spin on the edge can be said to polarize the neighboring spin singlets, due to its delocalization on close by sites. This enforces a fixed the phase of the AFM correlations in the bulk. In the theoretical zero temperature case, the structure is more pronounced and for both coupling regimes the edge
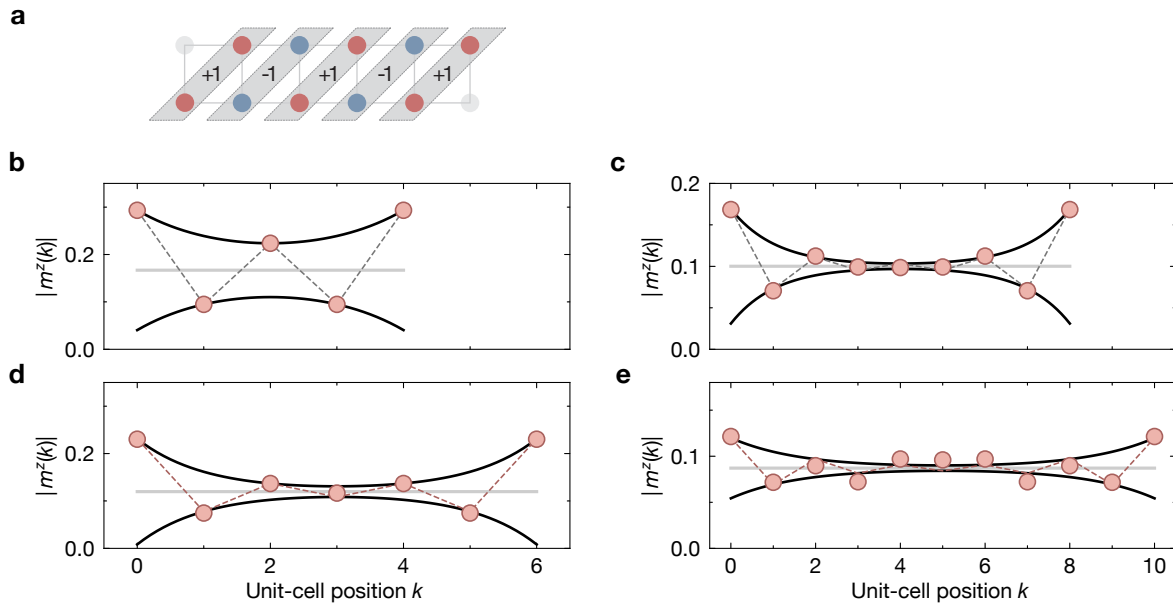
Figure 5.11: Staggered unit cell magnetization. We plot the magnetization per unit cell $m^z(k)$ for the topological configuration with system lengths L = 5 (**b**), L = 7 (**c**), L = 9 (**d**), L = 11 (**e**). The data is inversion averaged to increase statistics. An illustration of the plotted quantity is shown in **a**. The black lines show a fit to the data with the fit function (5.5).

magnetization is considerably stronger, while the bulk does not show the magnetization offset we see in the experimental data.

5.5.2   Decay length

The rung averaged data shown in the earlier Fig. 5.9 hides the staggered pattern, which was revealed in the magnetization maps. Measuring the magnetization along the unit cells, however, has the opposite effect of grouping sites according to the pattern. Fig. 5.11a illustrates the summed magnetization $m^z(k)$ over the unit cells. This quantity does not rely on the spin-1/2 representation of the Haldane phase which we realize in our spin ladders, but is a measure of the edge states that also exists in pure spin-1 systems.

Fig. 5.11b-e show the measured unit cell magnetization for different system lengths. The strong magnetization of the edge unit cell derives from the excess spin inhabiting the system edge with high probability. The exponentially localized AFM structure of the magnetization is induced by the edge mode leaking into the bulk [241]. With increasing length L the edge magnetization and the contrast of the AFM pattern decrease. This is due to the decreasing ground state fraction at longer system sizes. The bulk magnetization offset decreases with increasing length, despite the lower ground state fraction. This can be explained by the decreasing ratio of total magnetization and sites in the system $|M^z|/(2L)$. The excess spin is distributed over more sites.
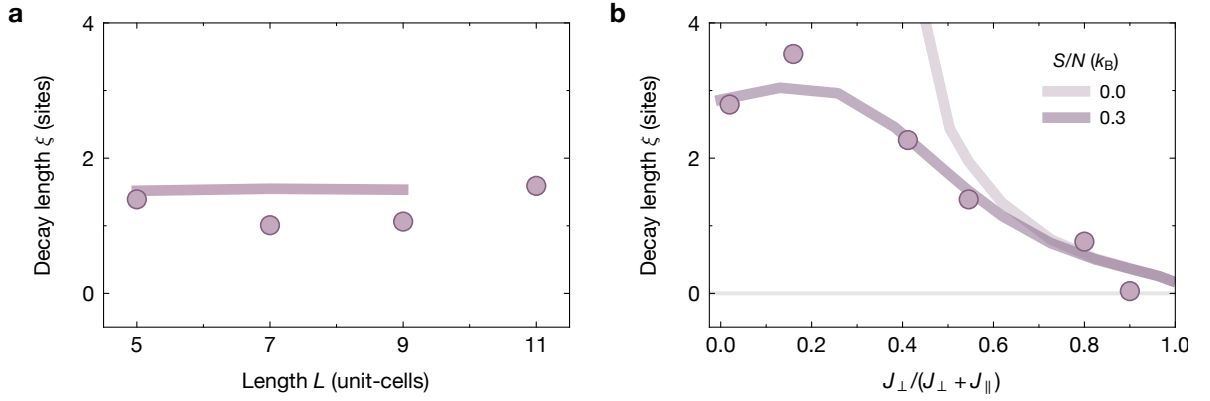
Figure 5.12: Measured edge state localization. The figure shows the fitted decay lengths ξ versus length L in **a** and versus coupling parameters in **b**. Shaded lines are indicate theoretical values calculated using ED of the Heisenberg model at fixed entropy per particle of $S/N = 0.3\,k_B$ in **a**, and both $S/N = 0\,k_B$ and $S/N = 0.3\,k_B$ in **b**. The localization length increases with leg coupling $J_\parallel$, but is independent of system size L.

The data for each system size is well described by an exponential fit function

$$m^z(k) = m_B + m_E \left((-1)^k e^{-k/\xi} + (-1)^{(L-k-1)/\xi} \right) , \tag{5.5}$$

with bulk magnetization offset m_B, edge magnetization m_E and the decay length ξ. This allows us to extract the localization length. In Fig. 5.12a the results of the fitted decay lengths ξ are plotted versus system length L. Despite the decreasing ground state fraction and decreasing edge magnetization and pattern visibility, we do not observe a clear tendency in the decay length versus system size. Instead, the decay length is relatively stable versus length. Small variations we attribute to experimental imperfections. The theoretical calculations up to system length $L = 9$ suggest a decay length completely independent of system size at our temperatures.

Fig. 5.12b shows the decay length for different coupling parameters. At strong rung coupling $J_\perp$ the edge states are almost completely localized on the edge unit cell. This is due to the lack of coupling along the ladder. In this parameter regime, the system basically consists of independent singlets and the excess magnetization has no other place to sit, than the site that is not forming a singlet. As the leg coupling $J_\parallel$ is increased with respect to the rung coupling, the excess spins are still largely confined to the edge of the system, but they can lower their kinetic energy by delocalizing onto neighboring sites. The localization length thus increases with the leg coupling, but eventually saturates due to a finite temperature cutoff. The edge mode can not delocalize beyond the thermal coherence length of the system.

We verify that our experimental method for extracting the decay length ξ gives a reliable estimate for the localization length. To this end, we relate the experimental

a

b
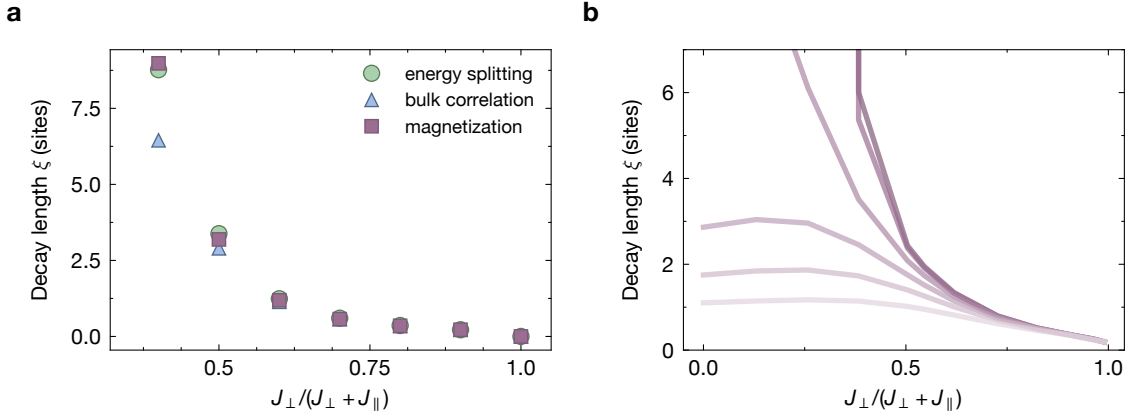
Figure 5.13: Edge state localization at zero temperature. a, We compare the approaches to calculate the decay length ξ from different quantities. Using DMRG of a Fermi-Hubbard ladder of large lengths $L > 50$ and $U/t_{\parallel} = 13$ at zero temperature, we calculate the decay length of the magnetization pattern (purple squares) as it was previously evaluated on the experimental data. We compare this to the localization length derived from the edge state splitting (green circles). Furthermore, the bulk correlation length is shown as blue triangles. When markers are not visible they coincide. The decay length from the magnetization pattern and the edge state splitting agree with a deviation of less than 6 % of their values. **b**, Finite temperature results for a system with $L = 5$ and entropy per particle $S/N = 0\,k_{\mathrm{B}}$ to $0.5k_{\mathrm{B}}$ in steps of $0.1\,k_{\mathrm{B}}$ with the lightest shading being the highest entropy. The decay length is calculated from the magnetization pattern in the Heisenberg model using ED.

decay length, which is determined from the staggered magnetization

$$\left|m^z(k)\right| \propto e^{-k/\xi}$$

to the theoretical localization length of the edge states at zero temperature. Numerically, the length over which the edge modes delocalize can be readily extracted from the energy splitting δ between the triplet and singlet ground states at a given system length via

$$\left|\delta\right| \propto e^{-L/\xi}.$$

Using DMRG of the Fermi-Hubbard model, we calculate the decay length of the magnetization pattern and the localization length from the edge state splitting (see Fig. 5.13a) for different coupling strengths $J_{\perp}/J_{\parallel}$. Both quantities agree over the full parameter range with deviations of less than 6 % of their value. Furthermore, we compare the decay length to the bulk correlation length and find that this quantity considerably deviates from the localization length and the magnetization pattern decay. The magnetization pattern is thus not governed by the bulk correlation length.

This demonstrates that the localization length can indeed be extracted from the decaying magnetization pattern. The difference between the two methods is, that the definition of the localization length via the edge state splitting depends on the spectrum
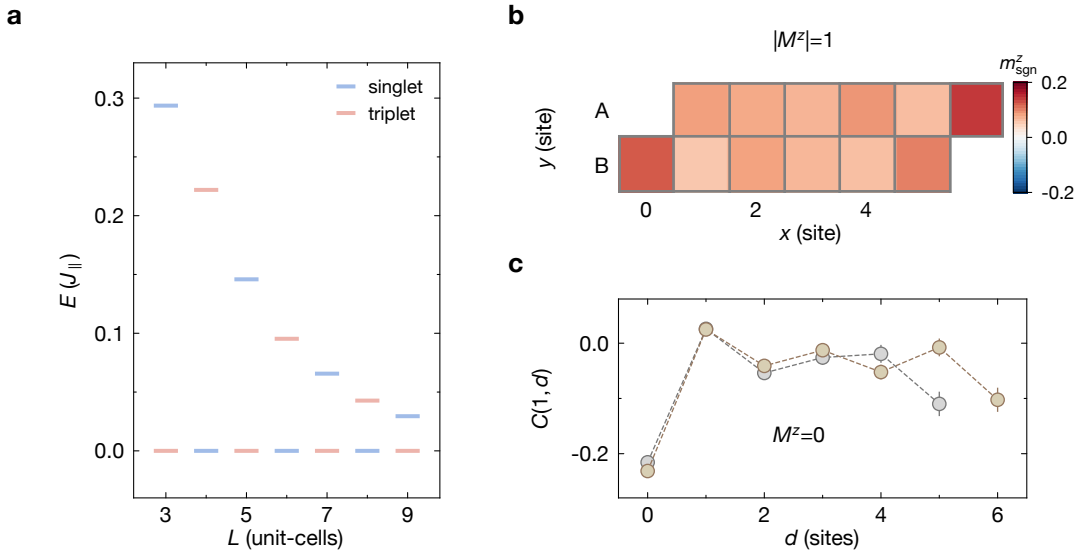
Figure 5.14: Edge state splitting.a, Energy splitting between the four ground states of the system in topological configuration. The ground states consist of three triplet (red bars) states with equal energy and one singlet (blue bars) state. The energy difference $\Delta_{ts} = E_{triplet} - E_{singlet}$ alternates its sign, with $\Delta_{ts} > 0$ for even system lengths and $\Delta_{ts} < 0$ for odd system lengths. The absolute value of the split decreases with increasing system size. **b**, Magnetization map of system length $L = 6$ and magnetization sector $|M^z| = 1$. At this length the alternating pattern can not extend over the full system, because the AFM structure of the two edges cancel in the center. **c**, Spin correlations $C(1, d)$ for system length $L = 6$ (brown markers) and $L = 5$ (grey markers) in magnetization sector $M^z = 0$. At both lengths the system shows strong nearest neighbor correlations and edge-to-edge correlations. At even length $L = 6$, a small alternating signal can be tracked through the system, similar to the magnetization patterns observed at add lengths in the magnetized sector. At odd length $L = 5$, the alternating signal cannot be observed through the system.

of the system, and is thus independent of temperature. The actual localization of the edge state, however, changes with temperature due to factors like a finite temperature cutoff. The decay of the magnetization pattern thus allows to extract a temperature-dependent localization length, which closely agrees with the temperature-independent definition at zero temperature.

In Fig. 5.13b we show the finite temperature decay length for a small system of $L = 5$ calculated from ED. We see that temperature effects play a minor role for the decay length at strong rung coupling $J_\perp$, but become dominant in the intermediate to strong leg coupling regime. At low temperatures, the decay length diverges in this regime, but at higher temperature the decay length reaches an upper limit and then stays relatively constant in the regime $0 \leq J_\perp \leq J_\parallel$.

5.5.3   Edge state energy splitting

In the thermodynamic limit, the Haldane phase has a bulk gap and four degenerate ground states. In finite size systems, however, there is a finite energy splitting between the total spin $S_{\text{tot}} = 0$ and total spin $S_{\text{tot}} = 1$ states, which are the respective singlet and triplet states of the edge modes. We have already made use of this edge state splitting in the calculations of the localization length. Now we will investigate the experimental signatures of the edge state splitting in our system. Fig. 5.14a shows the energy levels of the four ground states. The singlet and triplet ground states display a small energy difference, which quickly decreases with system length. The energy difference arises from the overlap of the edge modes in the bulk of the system due to their finite localization length. Depending on the parity of the system - whether it has even or odd length L - the triplet state or the singlet state have lower energy. This parity dependence can also be intuitively understood from the structure of the singlet and triplet states at even and odd length. For this we consider the magnetization map at $|M^z| = 1$ of a system at even length $L = 6$ (see Fig. 5.14b) and compare it to the magnetization maps and patterns at odd length (Fig. 5.10 and Fig. 5.11). At even length the magnetization pattern does not extend through the whole system, because the phase of the pattern starting at the left edge and the phase of the pattern starting at the right edge are shifted by π. They thus cancel in the center of the system, This is in contrast to the odd length systems, where we observe alternating magnetization patterns in the center of the bulk at length $L = 7$ and beyond. This gives an intuitive picture of why the triplet states, which the $|M^z| = 1$ states are a subset of, have lower energy at odd system length.

The singlet state, on the other hand, has an energy advantage for even system lengths. To understand this, we consider magnetization sector $M^z = 0$, which is not identical with the singlet state but allows for insights nevertheless. Fig. 5.14c shows the spin correlation $C(1, d)$ versus distance along the ladder. In this case, the alternating AFM pattern fits with the even length system of $L = 6$, but cancels in the center of the odd system of $L = 5$. This behavior is opposite to the structure of the system in the triplet state and explains, why the singlet state has lower energy for systems of even length.

5.6   Using ferromagnetic rung coupling

We have shown a realization of the Haldane phase which is conceptually close to the AKLT model. Our model consists of antiferromagnetically coupled spin-1/2 particles in a ladder system ($J_\perp, J_\parallel > 0$) leading to singlet character along the rungs and a unit cell definition, that connects the neighboring unit cells with singlet bonds. This, however, is not the only way to realize the Haldane phase from a spin-1/2 ladder system. An approach that is conceptually closer to the Heisenberg spin-1 chain uses ferromagnetic (FM) couplings ($J_\perp < 0$) on the rungs of the ladders and straight unit cells. Ferromagnetic couplings directly lead to a high spin-1 fraction along the rungs, which are chosen as the unit cells of the system. In the following we will demonstrate the realization of ferromagnetic rung couplings and observe the signatures of the Haldane phase in the system. We refer to this system as FM ladders, despite the leg coupling
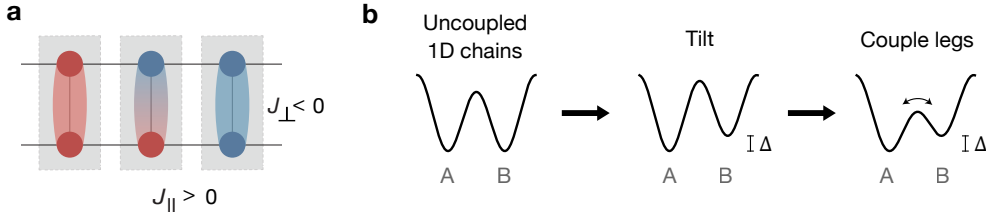
Figure 5.15: Preparing ladders with ferromagnetic rung coupling.a, A ladder system with antiferromagnetic leg coupling $J_\parallel > 0$ and ferromagnetic rung coupling $J_\perp < 0$. The unit cells are defined along the rungs. The colored oval bonds indicate triplet bonds between the spins. **b**, Preparation scheme. We first prepare undoped, uncoupled chains. Then we apply an optical potential offset $\Delta \gg U$ and subsequently we couple the chains by reducing the optical lattice depth in perpendicular direction.

being antiferromagnetic, in order to distinguish them from the completely antiferromagnetic spin ladders discussed until now, which we will refer to as AFM ladders.

System preparation

We can realize a ladder system with ferromagnetic coupling along the rungs, using a similar preparation sequence as in Ch. 4. We first prepare undoped ladder consisting of uncoupled 1D chains with a lattice depth of $V_{\mathrm{rung}} = 20\,E_R$ and $V_{\mathrm{leg}} = 3\,E_R$. We then apply an optical potential offset to one leg of each ladder using our DMD. We then slowly ramp the system to the final parameters of $V_{\mathrm{rung}} = 6\,E_R$ anf $V_{\mathrm{leg}} = 7\,E_R$ within $100\,\mathrm{ms}$ (see also Fig. 5.15b). The optical potential offset between the legs of the ladder is bigger than the interaction energy, $\Delta \gg U$. According to Eq. (4.1), this leads to a ferromagnetic rung coupling $J_\perp < 0$. The final FM system has coupling parameters $J_\perp = 1.2(2)\,J_\parallel$. The high optical potential offset of $\Delta \approx 1.5\,U$ is susceptible to long term drifts. To avoid taking into account data with $\Delta \leq U$ we had to discard data sets that show an average rung correlation $C(0,1) \leq 0$.

System characterization

We confirm the realization of FM ladders by measuring the rung spin correlations $C(0,1) = 0.07(1)$. The nearest neighbor spin correlations on the leg reach a value of $C(1,0) = -0.38(1)$, which is stronger than the leg correlations in the AFM ladders at comparable coupling strength. The spin correlations along the leg and rung do not compete in the FM ladders, because the rungs tend to form triplets and the system can effectively be understood as a 1D chain of spin-1 objects. This allows for higher correlation along the leg as compared to AFM ladders because spins that form pure singlets are fully entangled along the rung and thus cannot have correlations along the leg. Fig. 5.16 shows a map of the nearest-neighbor correlations of the system. The bonds along the rungs show positive correlations, while the bonds along the leg show strongly negative correlations. On the edges of the system, the leg spin correlations

are strongest. This is due to the reduced number of neighbors that the edge spins have to entangle with.

We note that, similar to the AFM ladders, also the ground state of the FM ladders does not display a 100 % triplet fraction in the unit cell at finite $J_\perp/J_\parallel$. The theoretical ground state triplet fraction can be seen in Fig. 5.17. The triplet fraction is above 80 % for all couplings and rises monotonically with $J_\perp/J_\parallel$. It reaches its maximum at $J_\parallel = 0$. At this point the zero temperature FM ladders consist of 100% triplets, but it realizes a relatively uninteresting spin-1 chain of uncoupled spins. The AFM ladders, in comparison, reach a maximum triplet fraction at the point of equal couplings $J_\perp = J_\parallel$ and display a decreasing value for higher rung coupling.

Signatures of the Haldane phase

To demonstrate the signatures of the Haldane phase in this system, we measure the same observables as previously for the AFM ladders. Fig. 5.18a shows the string correlators g_{S^z,R^z} and $g_{\mathbb{1},R^z}$. The spin-string correlator stays finite over the whole system with correlation values around $g_{S^z,R^z}(d > 1) \approx 0.1$, comparable to the AMF ladders in topological configuration. This reveals the hidden antiferromagnetic order in this system. The pure-string correlator is smaller than the spin-string correlator for most distances, except for distance $d = 3$. The two string correlators together are a clear sign of the Haldane phase. However, longer chains would be required to assure that the pure-string correlator decays to zero for all large distances $d \gg 1$ and the point at $d = 3$ is a short-distance effect. The inset of Fig. 5.18a shows the local spin correlations $C_1(d)$ between unit cells. The spin correlations decay quickly with distance and show a resurge in correlation value for maximum distance, indicating the edge states in the system. However, the decay is slower than in the AFM ladders with a clear alternating pattern up to distance $d = 4$ and a considerable correlation value at $d = 3$ of $C_1(3) = 0.092(7)$. The reason for this slightly longer-range spin correlation in the unit cell is the effective 1D nature of the system, with spin correlations not competing
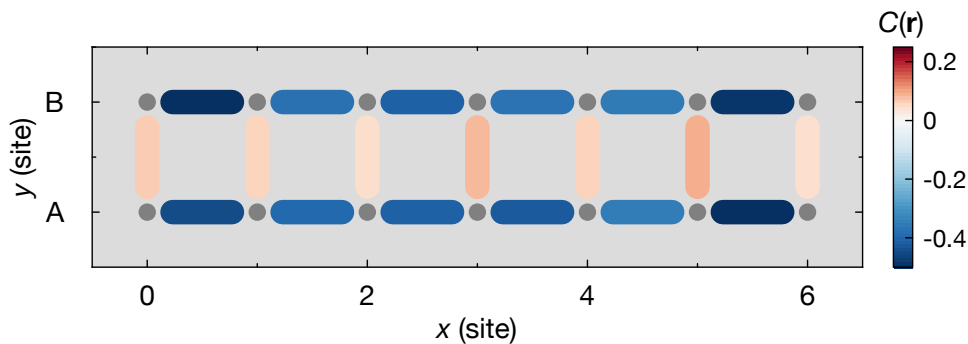
Figure 5.16: Map of the spin correlations in the FM ladders. The space resolved spin correlations $C(0,1)$ and $C(1,0)$ of the ferromagnetic ladders are plotted as bonds, whose color indicates the strength of the correlation. The endpoints of the bonds represent the position of the correlated sites within the ladder.
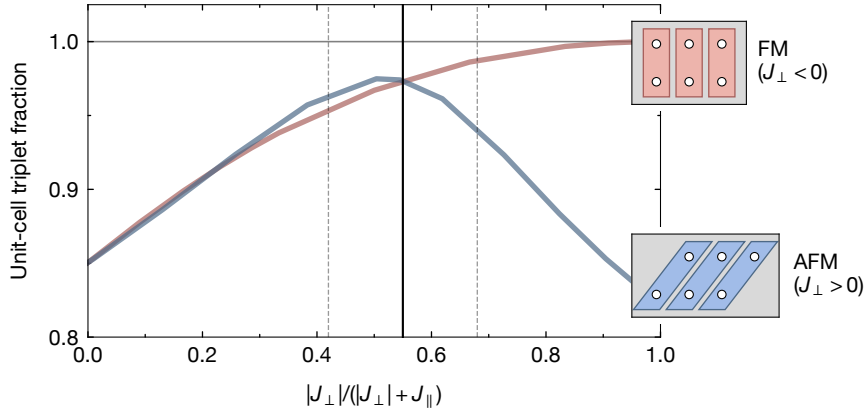
Figure 5.17: Unit-cell triplet fraction. The figure shows the ground state unit cell triplet fraction in the FM ladders with straight unit cell, compared to the AFM ladders with diagonal unit cell. In the low rung coupling regime, both systems have a comparable triplet fraction of about 85 %. The FM ladders reach their maximum in the strong rung coupling machine with up to 100 % triplets. The AFM ladders, on the other hand, reach the maximum triplet fraction at isotropic coupling $J_\perp = J_\parallel$. The figure is calculated using ED of the Heisenberg spin-1/2 model.

in the leg and rung direction.

The Haldane phase signatures include not only hidden AFM correlations but vanishing two-point spin correlations at large distances. At low temperatures and short lengths of our FM ladders, the spin correlations do not vanish, and thus they cannot be clearly identified as a finite-size version of the Haldane phase. Our temperatures, however, are high enough, so that the spin correlations vanish sufficiently and we can observe the features of the Haldane phase. In other words, temperature helps us to reduce the correlation length in the system and recover the features of the Haldane phase. This problem does not arise in the AFM ladders, because the spin correlations are inherently shorter due to the competition of the two directions.

Fig. 5.18b shows the unit cell averaged magnetization $|m^z(k)|$ in the magnetized sector $|M^z| = 1$. The strong magnetization on the outermost unit cell indicates the presence of edge states. The additional majority spins in the system sit predominantly at the edge of the system and induce an alternating magnetization pattern that decays towards the center of the system. We extract a localization length of $\xi = 1.3(1)$ sites, which is consistent with the results obtained in the AFM ladders. Note that, in the FM ladder realization of the Haldane phase, the edge mode is not strongly localized on the outermost lattice site, but is equally shared between both sites of the outermost unit cell.

5.7 Discussion

In this chapter, we have studied the physics of the Haldane phase using fermionic two-leg ladders in the Heisenberg regime. We have demonstrated two different ap-

a

b
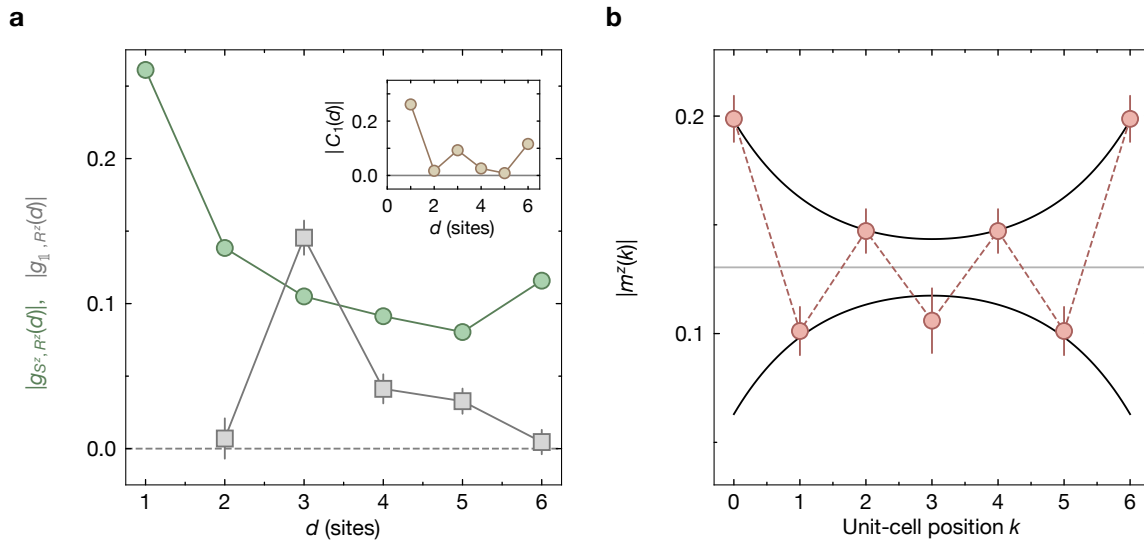
Figure 5.18: Signatures of the Haldane phase in ladders with ferromagnetic rung coupling. a, The string-spin g_{S^z,R^z} and string-only $g_{\mathbb{1},R^z}$ correlators are evaluated as a function of the rung distance d in straight-edge ladders (vertical unit cells) of length $L = 7$ with FM coupling along the rungs, in the sector of fixed total magnetization $M^z = 0$. Their behavior is analogous to the case of AFM ladders in the topological configuration, indicating topological order. (Inset) The two-point spin-spin correlator $C_1(d)$ decays rapidly to zero as a function of the distance d. **b**. In the magnetized sector $|M^z| = 1$ of the rung-FM ladder, the (vertical) unit cell averaged magnetization $|m^z(k)|$ shows a staggered pattern with decaying amplitude, similar to the one observed in the AFM ladder in topological configuration, indicating the presence of edge states.

proaches to realize this phase. One approach is based on antiferromagnetic ladders with diagonal unit cells and a tilted-edge termination. The other one is a mixed system with ferromagnetic rung couplings and antiferromagnetic leg couplings and straight unit cells along the rungs of the system. We have observed the main signatures of the Haldane phase in both systems. However, the AFM ladders are more suitable to observe the features of the Haldane phase at finite system size, due to the shorter bulk correlation length. We have thus used this system to investigate the robustness of the phase with respect to different system lengths and coupling parameters. We have compared the system to the trivial phase, which we have realized using antiferromagnetic ladders with straight unit cells.

The FM ladders are symmetric with respect to the legs, meaning that exchanging the particles in leg A with leg B does not change the system. This is in contrast to the AFM ladders, where the outermost edge site is unique. For the FM ladders the symmetry means that the edge state is not localized on the outermost lattice site, but equally shared between both sites of the edge unit cell. In that sense, the system is closer to the Haldane phase in a pure spin-1 chain, which is not divided into spin-1/2. The system is however less close to the AKLT model, which is built up of spin-1/2s and the edge

state is predominantly carried by the outermost spin-1/2. This confirms once more the view, that the AFM ladders in the topological configuration are conceptually very close to the AKLT model and thus present a very visual realization of the Haldane phase, which can help to demystify its properties. The realization using FM ladders, on the other hand, rather disguises the mechanisms of the Haldane phase, similar to an antiferromagnetic spin-1 chain. We thus argue that the AFM ladders are a more instructive way to demonstrate the Haldane phase. In the future, studies may extend the two-leg ladder to a varying number of legs where one expects clear differences between even and odd numbers of legs [242] and topological effects away from half-filling [243], or investigate topological phases in higher dimensions [244].

Conclusion and Outlook

6.1 Conclusion

In this thesis, I have presented quantum simulation experiments of antiferromagnetic Fermi-Hubbard ladders in the doped and undoped regimes. Spin-1/2 two-leg ladders were realized using ultracold fermionic atoms in optical lattices with arbitrary potential shaping. Harnessing the single site spin and density resolution of our quantum gas microscope, we have extracted real space correlations in the spin and charge sectors.

The main result of this thesis is the observation of magnetically mediated hole pairing in doped systems. By engineering a mixed-dimensional system, in which dopant motion is suppressed along one direction, we are able to confirm the formation of tightly bound pairs. We have reached a binding energy of about $E_B = 0.8\,J_\perp$, which constitutes an increase of more than an order of magnitude as compared to a standard, not mixed-dimensional ladder system. We have demonstrated the magnetic character of the binding mechanism and found signatures of considerable hole mobility along the system. At higher doping, a repulsive interaction between pairs was shown.

By demonstrating magnetically mediated hole pairing in a Fermi-Hubbard system, we confirm the role of magnetic correlations for a pairing mechanism possibly underlying unconventional superconductivity. Our mixed-dimensional approach delineates a strategy to increase the critical temperature for superconductivity.

A further result presented within this thesis is the observation of signatures of the Haldane phase. Mapping the spin-1/2 ladder system onto an integer spin chain has enabled the realization of a finite-size and finite-temperature version of this symmetry-protected topological phase. We have revealed symmetry fractionalization and the hidden antiferromagnetic order, which are characteristic of the Haldane spin-1 chain, by measuring non-local string order correlators. We have demonstrated the existence of edge states and extracted their localization length.

Besides the results of quantum simulating hole pairing and the Haldane phase, we have also achieved technical progress in the course of this thesis. We have developed a bilayer imaging technique which enables our vertical spin resolution of two-dimensional systems. Furthermore, we have equipped our experiment with a digital micromirror device for arbitrary potential shaping. We have also implemented real-time evaluation of the experimental snapshots and improved monitoring. Based on this, we have introduced several automatic feedback algorithms for the optical potential and vertical lattice phase.

Limitations

Even though we have demonstrated that magnetic correlations can mediate pairing, the role of this mechanism in unconventional superconductors remains to be experimentally verified. The biggest obstacle in the way of observing superconductivity in our quantum gas microscope is the current temperature limitation. Colder systems are needed to reach the critical temperature for superconductivity, even for our mixed-dimensional system. The same limitation holds for the realization of the Haldane phase, as topological phases of matter only truly exist at zero temperature [93]. Getting closer to this ideal regime is needed in order to observe the signatures of these phases in larger systems.

Besides temperature, system size is among our biggest experimental limitations. The short length of our ladder system has prevented us from exploring pairing in ladders with larger leg coupling, where even higher binding energies are expected [221]. The small system size in this thesis made it necessary to go to low leg coupling in order to reach a separation of scale between the pair size and the system size.

6.2 Outlook

The experimental results described within this thesis can be extended in several future studies, some of which have already been mentioned in the discussion of the respective chapters. In the following, we will thus give an overview of technical improvements that can overcome some of the technical limitations of the current setup. We will then discuss possible future studies for our setup and the possibilities of quantum simulation with ultracold fermions beyond the scope of our setup.

Technical improvements

Quantum gas microscopes are machines consisting of thousands of optical elements, electronic devices, and mechanical constructions. This complexity means that the failure of one component can make the whole machine inoperable. A future direction to improve the stability and reliability of our setups is modularization. For example, optical setups for different purposes can be standardized and placed in 19-inch racks [245]. In case of failure, such a setup can be quickly replaced. Miniaturization goes along a similar line, making setups more efficient and stable. A first step in this direction has been taken in our group by using a home-designed optics mounting system [246].

Imperfections in our optical lattice potential, as well as harmonic confinement, severely limit our system size and also affect the physics of the system by altering the tunneling strength and leading to density inhomogeneities. A new lattice setup can substantially reduce imperfections by choosing a new beam path that avoids high-NA lenses [207]. Furthermore, the red detuned lattice beams can be replaced by blue detuned ones, which avoids harmonic confinement in trade-off for a smaller anti-confinement. The experimental team of our lab is currently implementing these improvements with a new bichromatic superlattice setup for the xy-lattices, similar to

the z-lattice design discussed within this thesis.

Reaching colder temperatures

To tackle the temperature limitation of fermionic quantum gas microscopes, several cooling schemes have been proposed. A vertical superlattice can be utilized to couple the system to an entropy bath [247, 248]. This bilayer cooling technique has homogeneous contact between the system and the bath. It is thus advantageous over a reservoir surrounding the system in a two-dimensional plane, which is already being used in our and other experiments [212, 249]. In addition to such entropy redistribution schemes one can prepare low entropy band insulators, which have a larger charge gap than Mott insulators. The low entropy system is then adiabatically transformed into an antiferromagnet, either using a superlattice and lattice for the band insulator and Mott insulator or by introducing empty lattice sites around the system [59].
A different approach for effectively reaching colder systems is to reduce the lattice spacing. A shorter lattice constant increases the energy scales of the system and thus increases the absolute temperature required to reach low-temperature phases like superconductivity. Shorter lattices can be achieved by using blue-detuned laser sources in a retro-reflected configuration. spacings on the order of 200 nm could for example be reached using blue laser diodes. Atoms in a lattice with spacings on this order can not be resolved in situ, but quantum gas magnifiers [250] have the potential to overcome this challenge.

Future experiments

Bilayer systems are an interesting direction for future investigations in our system. Our vertical superlattice setup with its bilayer imaging is well equipped to study this setting. Bilayer systems are expected to display strong pairing in the mixed-dimensional setting, as it was discussed in the respective chapter. But also in the standard setting they are highly interesting systems that display a phase transition from two- dimensional antiferromagnetic layers to a band insulator of singlets between the layers [251]. Bilayer systems are highly relevant regarding the quantum simulation of high-T_C superconductivity because higher critical temperatures are expected for the bilayer Hubbard model [252, 253]. Unfortunately, spin resolution in the vertical direction is not possible for a bilayer system in our setup, but in-plane spin resolution will be readily available with the new xy-superlattice setup.
Further experimental directions that can be explored with our system is the creation of Mott-Hubbard excitons [254], which play an important role in semiconductor physics. These doublon-hole pairs can be excited in our system by local or global periodic modulation of the lattice potential. Another possible direction is to demonstrate collisional or spin-exchange gates [255, 256]. If we encode a qubit in the two spin states, we can realize a two-qubit gate by coupling two atoms for a well-defined time using our superlattice potential. Through the spin-exchange interaction, the two spin states become entangled and we can realize a $\sqrt{\text{SWAP}}$ gate. The realization of high-fidelity two-qubit gates in our system would be an important step towards programmable quantum simulation with cold fermionic atoms.

Programmability is an exciting direction to demonstrate and harness the quantum advantage of the cold atom platform [8]. Near-deterministic initial state preparation allows for the engineering of low entropy initial states. It also enables the time evolution of arbitrary initial states, thereby vastly increasing the scope and precision of quantum simulation. Initial state engineering has for example recently been demonstrated for tunnel-coupled optical tweezers of fermionic atoms with full spin and density resolved readout [257].

Programmable quantum simulators can furthermore be used to construct the dynamics of the system. The analogue evolution under the native Hamiltonian can be supplemented with periodic digital gates. This is a field which is rapidly progressing [258, 259], and programmable quantum simulators based on cold fermions are currently being construction, e.g. [260]. A hybrid approach of this kind offers new possibilities to simulate the dynamics of a whole range of Hamiltonians on a single machine, without the requirements of a full-fledged quantum computer, like the need for error correction.

Derivation of the binding energy

In order to estimate the binding energy of the paired state from the experimental data, we compare the measured $g_{\mathrm{h}}^{(2)}(0,1)$ correlation to an analytically tractable effective Hamiltonian. We start from the $t - J$ Hamiltonian (2.9) and neglect the two smallest energy scales $t_{\parallel}, J_{\parallel}$, which are both below the estimated temperature T of our dataset. Since the Hamiltonian then completely decouples into individual rungs, we can then exactly diagonalize it. The eigenstates of each rung are the two-hole state $|\mathrm{hh}\rangle$, the spin-hole states $|\mathrm{sh}, y, \sigma\rangle$, of which there are four, with leg index $y = 0, 1$ and spin index $\sigma = \uparrow, \downarrow$, the spin-singlet state $|\mathrm{S}\rangle$ and the three spin-triplet states $|\mathrm{T}, m\rangle$ with $m = -1, 0, 1$. The corresponding eigenenergies are

$$
\begin{aligned}
\epsilon_{\mathrm{hh}} &= V, \\
\epsilon_{\mathrm{sh}} &= \epsilon_{\mathrm{T}} = 0 \quad \text{and} \\
\epsilon_{\mathrm{S}} &= -J_{\perp},
\end{aligned}
\tag{A.1}
$$

with a variable hh state energy V. In the uncoupled rung limit of $t_{\parallel} = J_{\parallel} = 0$, this energy vanishes to $V = 0$, but for finite couplings $t_{\parallel}, J_{\parallel} \neq 0$, we expect a non-zero renormalization. While V can be calculated perturbatively [261], we treat it as a free parameter here and thus go beyond a perturbative analysis.

We consider the binding energy of our simplified model in the thermodynamic limit $L = \infty$, which in the undoped ground state has an energy of $E_{0\mathrm{h}} = -LJ_{\perp}$. A system containing two independent holes has ground state energy $2(E_{1\mathrm{h}} - E_{0\mathrm{h}}) = 2J_{\perp}$, because it misses two singlets that are part of the undoped ground state. The ground state energy of a system with two holes, however, is $E_{2\mathrm{h}} - E_{0\mathrm{h}} = V + J_{\perp}$, due to one missing singlet and the additional energy V of the two holes. The binding energy follows as the difference between two independent holes and a pair of holes

$$
E_{\mathrm{b}} = 2E_{1\mathrm{h}} - E_{0\mathrm{h}} - E_{2\mathrm{h}} = J_{\perp} - V.
\tag{A.2}
$$

For $E_{\mathrm{b}} > 0$ the ground state of a doped system is paired.

To relate the binding energy to the measured $g_{\mathrm{h}}^{(2)}$ correlator, we perform a canonical calculation assuming exactly one hole per leg. We remember the probability in a canonical ensemble [262]

$$
p_i = \frac{1}{Z} e^{-E_i \beta}
$$

with the partition function

$$Z = \sum_i e^{-E_i \beta},$$

where $\beta = 1/(k_B T)$. The probability for two holes to occupy the same rung is thus given by

$$p_{hh} = \frac{L}{Z} e^{-\beta E_{hh}} Z_S^{L-1}, \tag{A.3}$$

which is composed of L different rungs that can host the two holes and the different combinations of singlets and triplets that are possible on the $L - 1$ other rungs

$$Z_S = e^{-\beta E_S} + 3e^{-\beta E_T},$$

with E_S and E_T defined as in Eq. (A.1). The total partition function is given by

$$Z = L e^{-\beta E_{hh}} Z_S^{L-1} + 4L(L-1) e^{-2\beta E_{sh}} Z_S^{L-2}.$$

Furthermore, following the definition of the $g_h^{(2)}$ function in Eq. (4.3), we obtain the relation

$$g_h^{(2)}(0,1) = \frac{p_{hh}/L}{(1/L)^2} - 1, \tag{A.4}$$

where we have assumed a homogeneous density of $\langle \hat{n}_i \rangle = 2/(2L)$ on each site and a homogeneous probability per rung of $1/L$. Thus $\langle \hat{n}_i^h \hat{n}_j^h \rangle = p_{hh}/L$ for fixed (i,j) on one rung. There are thus L identical terms in the sum of $g_h^{(2)}$, which cancel with $\mathcal{N}_{(0,1)} = L$.

Finally, inserting A.3 and A.2 into A.4, yields Eq. (4.5)

$$E_b = -\beta^{-1} \ln \left[\frac{\left(1 + 3e^{-\beta J_\perp}\right) \left(1 - \frac{g_h^{(2)}(0,1)}{L-1}\right)}{4 \left(1 + g_h^{(2)}(0,1)\right)} \right].$$

Numerical simulations

B.1 DMRG calculations for chapter 4

In chapter 4, the experimental results for the mixed-dimensional and standard ladders are compared to theoretical expectations. Those calculations were carried out by Annabelle Bohrdt. She performed simulations of the $t - J$ model, Eq. (2.9), using matrix product states (MPS). In the mixed-dimensional system, the simulated parameter regime is $J_\parallel / J_\perp = 0.047$, $t_\parallel / J_\perp = 0.7$ and $t_\perp = 0$. For the standard system the parameters are $J_\parallel / J_\perp = 0.06$, $t_\parallel / J_\perp = 0.9$, and $t_\perp / J_\perp = 3.57$. This corresponds to the $t - J$ model derived from a Fermi-Hubbard model with $U/t_\perp = 14.16$, $t_\parallel / t_\perp = 0.26$, and, in the mixed-dimensional case, $\Delta / U = 0.5$. The MPS simulations are performed using the TeNPy package [263, 264]. For ground state simulations, for example to obtain the binding energies, the DMRG algorithm is used with a fixed S_z^{tot} as well as particle number sector. For simulations are finite temperature, the purification method [265, 266] is used, where the Hilbert space is enlarged by an auxiliary site $a(i)$ per physical site i. The auxiliary degrees of freedom are traced out in order to obtain the finite temperature state. The starting point is an infinite temperature state, in which the physical and auxiliary degrees of freedom on each site are maximally entangled. An entangler Hamiltonian [267] is implemented to prepare the infinite temperature state of the $t - J$ model. A chemical potential μ is introduced to control the average number of holes in the system. The W^{II}-time-evolution method [268] is then used to perform imaginary-time evolution up to the desired temperature. Depending on the system size, model (standard $t - J$ versus mixed-dimensional or Fermi-Hubbard), doping, and temperature (finite temperature versus ground state), a bond dimension between $\chi = 50$ and $\chi = 400$ is used. For the finite temperature calculations, an imaginary time step of $dt/J_\perp = 0.025$ is employed. The results have been carefully checked for convergence in the bond dimension as well as the size of the time step. We benchmarked the MPS calculations by comparing them to exact diagonalization for small system sizes and found the same results.

In order to directly compare to the experimental data, snapshots were directly sampled from the matrix product state using the perfect sampling algorithm [269]. In the evaluation of the snapshots, we account for the experimental detection fidelity by randomly placing artificial holes in the MPS snapshots according to our detection fidelity. We then apply the same filters regarding hole number and occupation imbalance as for the experimental data and model the hole number distribution of the experimental data by weighting the snapshots accordingly.

B.2 Numerical calculations for chapter 5

In chapter 5, we employed two different numerical methods to obtain theoretical predictions for the experimentally measured observables. Exact diagonalization was used for calculations of the Heisenberg model at small system sizes and for finite temperatures. DMRG calculations were performed for the Fermi-Hubbard model by Julian Bibo and Ruben Verresen, calculating the ground state at large system sizes.

ED calculations

The results in the Heisenberg regime were obtained using exact diagonalization (ED) of our spin-1/2 ladders up to sizes of $L = 9$, limited by computational resources. For each data point, the system size and geometry in the ED simulation are the same as in the experimental data. The finite temperature results were obtained by using the full spectrum. We specify the entropy per particle $s = S/N$, which we find to be approximately independent of coupling parameters in the experimental realizations.

DMRG calculations

The results for large systems at zero temperature are calculated using the Density Matrix Renormalization Group (DMRG) Ansatz [3] based on the TeNPy library (version 0.3.0) [263]. The simulations of the ladder system go beyond the $t - J$-model and take into account the full Fermi-Hubbard model. Total particle number and total magnetization are conserved. To obtain the infinite length value of the string order parameters, different lengths $d \in [200, 400, ..., 1600]$ were calculated to make sure its final value is converged. To numerically compare different approaches to extract the decay length, a system with $L = 100$, $U/t_\parallel = 13$ is simulated at zero temperature. The decay length of the edge magnetization is extracted from the ground state in the sector $M^z = 1$ using a bond dimension $\chi = 1000$. The maximal energy truncation error is kept below 10^{-7} for all parameters. To obtain the localization length from the energy splitting, the different spin sectors $M^z \in \{0, 1\}$ are calculated. Choosing system lengths of $L \in [4, 8, ..., 52]$ and a bond dimension $\chi = 1000$, the maximal energy truncation error is again kept below 10^{-7}.

Bibliography

[1] D. J. Thouless. *The quantum mechanics of many-body systems*. Courier Corporation (2014). (Cited on page **1**)

[2] A. L. Fetter and J. D. Walecka. *Quantum theory of many-particle systems*. Courier Corporation (2012). (Cited on page **1**)

[3] S. R. White. *Density matrix formulation for quantum renormalization groups*. Phys. Rev. Lett. **69**, 2863 (1992). (Cited on pages **1** and **110**)

[4] K. G. Wilson. *The renormalization group: Critical phenomena and the Kondo problem*. Rev. Mod. Phys. **47**, 773–840 (1975). (Cited on page **1**)

[5] W. M. C. Foulkes, L. Mitas, R. J. Needs, and G. Rajagopal. *Quantum Monte Carlo simulations of solids*. Rev. Mod. Phys. **73**, 33–83 (2001). (Cited on page **1**)

[6] M. T. Mora-Aznar. *Condensed-Matter and Materials Physics: Basic Research for Tomorrow's Technology*. Eur. J. Phys. **21**, 197 (2000). (Cited on page **1**)

[7] R. P. Feynman. *Simulating physics with computers*. Int. J. Theor. Phys. **21**, 467–488 (1982). (Cited on page **1**)

[8] A. J. Daley, I. Bloch, C. Kokail, S. Flannigan, N. Pearson, M. Troyer, and P. Zoller. *Practical quantum advantage in quantum simulation*. Nature **607**, 667–676 (2022). (Cited on pages **1**, **10**, and **106**)

[9] I. H. Deutsch. *Harnessing the Power of the Second Quantum Revolution*. PRX Quantum **1**, 020101 (2020). (Cited on page **1**)

[10] D. Porras and J. I. Cirac. *Quantum manipulation of trapped ions in two dimensional Coulomb crystals*. Phys. Rev. Lett. **96**, 250501 (2006). (Cited on page **1**)

[11] J. Chiaverini and W. Lybarger Jr. *Laserless trapped-ion quantum simulations without spontaneous scattering using microtrap arrays*. Phys. Rev. A **77**, 022324 (2008). (Cited on page **1**)

[12] R. Schmied, T. Roscilde, V. Murg, D. Porras, and J. I. Cirac. *Quantum phases of trapped ions in an optical lattice*. New J. Phys **10**, 045017 (2008). (Cited on page **1**)

[13] M. Lewenstein, A. Sanpera, V. Ahufinger, B. Damski, A. Sen, and U. Sen. *Ultracold atomic gases in optical lattices: mimicking condensed matter physics and beyond*. Adv. Phys. **56**, 243–379 (2007). (Cited on page **1**)

[14] E. Manousakis. *A quantum-dot array as model for copper-oxide superconductors: A dedicated quantum simulator for the many-fermion problem*. J. Low Temp. Phys. **126**, 1501–1513 (2002). (Cited on page **1**)

[15] T. Byrnes, N. Y. Kim, K. Kusudo, and Y. Yamamoto. *Quantum simulation of Fermi-Hubbard models in semiconductor quantum-dot arrays*. Phys. Rev. B **78**, 075320 (2008). (Cited on page **1**)

[16] A. van Oudenaarden and J. Mooij. *One-dimensional Mott insulator formed by quantum vortices in Josephson junction arrays*. Phys. Rev. Lett. **76**, 4947 (1996). (Cited on page **1**)

[17] T. Yamamoto, M. Watanabe, J. You, Y. A. Pashkin, O. Astafiev, Y. Nakamura, F. Nori, and J. Tsai. *Spectroscopy of superconducting charge qubits coupled by a Josephson inductance*. Phys. Rev. B **77**, 064505 (2008). (Cited on page **1**)

[18] I. Bloch, J. Dalibard, and W. Zwerger. *Many-body physics with ultracold gases*. Rev. Mod. Phys. **80**, 885–964 (2008). (Cited on pages **1** and **10**)

[19] C. Gross and I. Bloch. *Quantum simulations with ultracold atoms in optical lattices*. Science **357**, 995–1001 (2017). (Cited on page **1**)

[20] S. I. Mistakidis, A. G. Volosniev, R. E. Barfknecht, T. Fogarty, T. Busch, A. Foerster, P. Schmelcher, and N. T. Zinner. *Cold atoms in low dimensions – a laboratory for quantum dynamics*. arXiv:2202.11071 (2022). (Cited on page **1**)

[21] K. Martiyanov, V. Makhalov, and A. Turlapov. *Observation of a Two-Dimensional Fermi Gas of Atoms*. Phys. Rev. Lett. **105**, 030404 (2010). (Cited on page **1**)

[22] Z. Hadzibabic, P. Krüger, M. Cheneau, S. P. Rath, and J. Dalibard. *The trapped two-dimensional Bose gas: from Bose–Einstein condensation to Berezinskii–Kosterlitz–Thouless physics*. New J. Phys **10**, 045006 (2008). (Cited on page **1**)

[23] B. DeMarco and D. S. Jin. *Onset of Fermi Degeneracy in a Trapped Atomic Gas*. Science **285**, 1703–1706 (1999). (Cited on pages **1** and **10**)

[24] F. Serwane, G. Zürn, T. Lompe, T. B. Ottenstein, A. N. Wenz, and S. Jochim. *Deterministic Preparation of a Tunable Few-Fermion System*. Science **332**, 336–338 (2011). (Cited on page **1**)

[25] R. Meppelink, S. B. Koller, J. M. Vogels, P. van der Straten, E. D. van Ooijen, N. R. Heckenberg, H. Rubinsztein-Dunlop, S. A. Haine, and M. J. Davis. *Observation of shock waves in a large Bose-Einstein condensate*. Phys. Rev. A **80**, 043606 (2009). (Cited on page **1**)

[26] M. J. H. Ku, A. T. Sommer, L. W. Cheuk, and M. W. Zwierlein. *Revealing the Superfluid Lambda Transition in the Universal Thermodynamics of a Unitary Fermi Gas*. Science **335**, 563–567 (2012). (Cited on page **1**)

[27] L. Sobirey, N. Luick, M. Bohlen, H. Biss, H. Moritz, and T. Lompe. *Observation of superfluidity in a strongly correlated two-dimensional Fermi gas*. Science **372**, 844–846 (2021). (Cited on page 1)

[28] W. D. Phillips. *Nobel Lecture: Laser cooling and trapping of neutral atoms*. Rev. Mod. Phys. **70**, 721–741 (1998). (Cited on page 1)

[29] M. H. Anderson, J. R. Ensher, M. R. Matthews, C. E. Wieman, and E. A. Cornell. *Observation of Bose-Einstein Condensation in a Dilute Atomic Vapor*. Science **269**, 198–201 (1995). (Cited on page 1)

[30] K. B. Davis, M. O. Mewes, M. R. Andrews, N. J. van Druten, D. S. Durfee, D. M. Kurn, and W. Ketterle. *Bose-Einstein Condensation in a Gas of Sodium Atoms*. Phys. Rev. Lett. **75**, 3969–3973 (1995). (Cited on page 1)

[31] C. C. Bradley, C. A. Sackett, J. J. Tollett, and R. G. Hulet. *Evidence of Bose-Einstein Condensation in an Atomic Gas with Attractive Interactions*. Phys. Rev. Lett. **75**, 1687–1690 (1995). (Cited on page 1)

[32] W. Zwerger. *The BCS-BEC crossover and the unitary Fermi gas*, volume 836. Springer Science & Business Media (2011). (Cited on page 1)

[33] M. Greiner and S. Fölling. *Optical lattices*. Nature **453**, 736–738 (2008). (Cited on page 1)

[34] D. Jaksch, C. Bruder, J. I. Cirac, C. W. Gardiner, and P. Zoller. *Cold Bosonic Atoms in Optical Lattices*. Phys. Rev. Lett. **81**, 3108–3111 (1998). (Cited on page 1)

[35] W. Hofstetter, J. I. Cirac, P. Zoller, E. Demler, and M. D. Lukin. *High-Temperature Superfluidity of Fermionic Atoms in Optical Lattices*. Phys. Rev. Lett. **89**, 220407 (2002). (Cited on page 1)

[36] M. Greiner, O. Mandel, T. Esslinger, T. W. Hänsch, and I. Bloch. *Quantum phase transition from a superfluid to a Mott insulator in a gas of ultracold atoms*. Nature **415**, 39 (2002). (Cited on page 1)

[37] I. Bloch and M. Greiner. *The superfluid-to-Mott insulator transition and the birth of experimental quantum simulation*. Nat. Rev. Phys. **4**, 739–740 (2022). (Cited on page 1)

[38] M. Schreiber, S. S. Hodgman, P. Bordia, H. P. Lüschen, M. H. Fischer, R. Vosk, E. Altman, U. Schneider, and I. Bloch. *Observation of many-body localization of interacting fermions in a quasirandom optical lattice*. Science **349**, 842–845 (2015). (Cited on page 1)

[39] G. Jotzu, M. Messer, R. Desbuquois, M. Lebrat, T. Uehlinger, D. Greif, and T. Esslinger. *Experimental realization of the topological Haldane model with ultracold fermions*. Nature **515**, 237–240 (2014). (Cited on page 2)

[40] M. Aidelsburger, M. Atala, M. Lohse, J. T. Barreiro, B. Paredes, and I. Bloch. *Realization of the Hofstadter Hamiltonian with Ultracold Atoms in Optical Lattices.* Phys. Rev. Lett. **111**, 185301 (2013). (Cited on page 2)

[41] J. F. Sherson, C. Weitenberg, M. Endres, M. Cheneau, I. Bloch, and S. Kuhr. *Single-atom-resolved fluorescence imaging of an atomic Mott insulator.* Nature **467**, 68–72 (2010). (Cited on pages 2 and 13)

[42] W. S. Bakr, A. Peng, M. E. Tai, R. Ma, J. Simon, J. I. Gillen, S. Fölling, L. Pollet, and M. Greiner. *Probing the Superfluid–to–Mott Insulator Transition at the Single-Atom Level.* Science **329**, 547–550 (2010). (Cited on page 2)

[43] E. Haller, J. Hudson, A. Kelly, D. A. Cotta, B. Peaudecerf, G. D. Bruce, and S. Kuhr. *Single-atom imaging of fermions in a quantum-gas microscope.* Nat. Phys. **11**, 738–742 (2015). (Cited on pages 2 and 13)

[44] L. W. Cheuk, M. A. Nichols, M. Okan, T. Gersdorf, V. V. Ramasesh, W. S. Bakr, T. Lompe, and M. W. Zwierlein. *Quantum-Gas Microscope for Fermionic Atoms.* Phys. Rev. Lett. **114**, 193001 (2015). (Cited on pages 2 and 13)

[45] M. F. Parsons, F. Huber, A. Mazurenko, C. S. Chiu, W. Setiawan, K. Wooley-Brown, S. Blatt, and M. Greiner. *Site-Resolved Imaging of Fermionic ^{6}Li in an Optical Lattice.* Phys. Rev. Lett. **114**, 213002 (2015). (Cited on pages 2, 13, and 33)

[46] A. Omran, M. Boll, T. A. Hilker, K. Kleinlein, G. Salomon, I. Bloch, and C. Gross. *Microscopic Observation of Pauli Blocking in Degenerate Fermionic Lattice Gases.* Phys. Rev. Lett. **115**, 263001 (2015). (Cited on pages 2 and 13)

[47] M. Boll, T. A. Hilker, G. Salomon, A. Omran, J. Nespolo, L. Pollet, I. Bloch, and C. Gross. *Spin- and density-resolved microscopy of antiferromagnetic correlations in Fermi-Hubbard chains.* Science **353**, 1257–1260 (2016). (Cited on pages 2, 13, 14, and 39)

[48] M. Endres, M. Cheneau, T. Fukuhara, C. Weitenberg, P. Schauß, C. Gross, L. Mazza, M. C. Bañuls, L. Pollet, I. Bloch, and S. Kuhr. *Observation of Correlated Particle-Hole Pairs and String Order in Low-Dimensional Mott Insulators.* Science **334**, 200 (2011). (Cited on page 2)

[49] L. W. Cheuk, M. A. Nichols, K. R. Lawrence, M. Okan, H. Zhang, and M. W. Zwierlein. *Observation of 2D Fermionic Mott Insulators of ^{40}K with Single-Site Resolution.* Phys. Rev. Lett. **116**, 235301 (2016). (Cited on page 2)

[50] M. F. Parsons, A. Mazurenko, C. S. Chiu, G. Ji, D. Greif, and M. Greiner. *Site-resolved measurement of the spin-correlation function in the Fermi-Hubbard model.* Science **353**, 1253–1256 (2016). (Cited on pages 2 and 13)

[51] A. Ashkin. *Optical trapping and manipulation of neutral particles using lasers.* Proc. Natl. Acad. Sci. **94**, 4853–4860 (1997). (Cited on page 2)

[52] H. Bernien, S. Schwartz, A. Keesling, H. Levine, A. Omran, H. Pichler, S. Choi, A. S. Zibrov, M. Endres, M. Greiner, V. Vuletić, and M. D. Lukin. *Probing many-body dynamics on a 51-atom quantum simulator*. Nature **551**, 579–584 (2017). (Cited on page **2**)

[53] D. Barredo, S. d. Léséleuc, V. Lienhard, T. Lahaye, and A. Browaeys. *An atom-by-atom assembler of defect-free arbitrary two-dimensional atomic arrays*. Science **354**, 1021–1023 (2016). (Cited on page **2**)

[54] S. Ebadi, T. T. Wang, H. Levine, A. Keesling, G. Semeghini, A. Omran, D. Bluvstein, R. Samajdar, H. Pichler, W. W. Ho, S. Choi, S. Sachdev, M. Greiner, V. Vuletić, and M. D. Lukin. *Quantum phases of matter on a 256-atom programmable quantum simulator*. Nature **595**, 227–232 (2021). (Cited on page **2**)

[55] P. M. Preiss, R. Ma, M. E. Tai, J. Simon, and M. Greiner. *Quantum gas microscopy with spin, atom-number, and multilayer readout*. Phys. Rev. A **91**, 041602 (2015). (Cited on pages **2** and **76**)

[56] J. Koepsell, S. Hirthe, D. Bourgund, P. Sompet, J. Vijayan, G. Salomon, C. Gross, and I. Bloch. *Robust Bilayer Charge Pumping for Spin- and Density-Resolved Quantum Gas Microscopy*. Phys. Rev. Lett. **125**, 010403 (2020). (Cited on pages **2**, **14**, **48**, and **76**)

[57] T. Hartke, B. Oreg, N. Jia, and M. Zwierlein. *Doublon-Hole Correlations and Fluctuation Thermometry in a Fermi-Hubbard Gas*. Phys. Rev. Lett. **125**, 113601 (2020). (Cited on pages **2**, **14**, **57**, and **76**)

[58] C. Weitenberg, M. Endres, J. F. Sherson, M. Cheneau, P. Schauß, T. Fukuhara, I. Bloch, and S. Kuhr. *Single-spin addressing in an atomic Mott insulator*. Nature **471**, 319–324 (2011). (Cited on page **2**)

[59] C. S. Chiu, G. Ji, A. Mazurenko, D. Greif, and M. Greiner. *Quantum State Engineering of a Hubbard System with Ultracold Fermions*. Phys. Rev. Lett. **120**, 243201 (2018). (Cited on pages **2** and **105**)

[60] G. R. Stewart. *Unconventional superconductivity*. Adv. Phys. **66**, 75–196 (2017). (Cited on page **2**)

[61] P. A. Lee, N. Nagaosa, and X.-G. Wen. *Doping a Mott insulator: Physics of high-temperature superconductivity*. Rev. Mod. Phys. **78**, 17–85 (2006). (Cited on pages **2**, **11**, **14**, and **47**)

[62] A. Schilling, M. Cantoni, J. D. Guo, and H. R. Ott. *Superconductivity above 130 K in the Hg–Ba–Ca–Cu–O system*. Nature **363**, 56–58 (1993). (Cited on page **2**)

[63] J. Brooks and J. Schrieffer. *Handbook of High -Temperature Superconductivity: Theory and Experiment*. Springer New York (2007). (Cited on page **2**)

[64] J. Bardeen, L. N. Cooper, and J. R. Schrieffer. *Microscopic Theory of Superconductivity*. Phys. Rev. **106**, 162–164 (1957). (Cited on page **2**)

[65] D. J. Scalapino. *Superconductivity and Spin Fluctuations*. J. Low Temp. Phys. **117**, 179–188 (1999). (Cited on pages **2** and **47**)

[66] D. J. Scalapino. *A common thread: The pairing interaction for unconventional superconductors*. Rev. Mod. Phys. **84**, 1383–1417 (2012). (Cited on pages **2** and **14**)

[67] B. White, J. Thompson, and M. Maple. *Unconventional superconductivity in heavy-fermion compounds*. Phys. C: Supercond. Appl. **514**, 246–278 (2015). (Cited on page **2**)

[68] H.-H. Wen and S. Li. *Materials and Novel Superconductivity in Iron Pnictide Superconductors*. Annu. Rev. Condens. Matter Phys. **2**, 121–140 (2011). (Cited on page **2**)

[69] J. Wosnitza. *Superconductivity in Layered Organic Metals*. Crystals **2**, 248–265 (2012). (Cited on pages **2** and **47**)

[70] J. G. Bednorz and K. A. Müller. *Possible highTc superconductivity in the Ba–La–Cu–O system*. Z. Phys. B **64**, 189–193 (1986). (Cited on pages **2** and **14**)

[71] J. G. Bednorz, M. Takashige, and K. A. Müller. *Susceptibility Measurements Support High- T c Superconductivity in the Ba-La-Cu-O System*. EPL **3**, 379–386 (1987). (Cited on page **2**)

[72] S.-i. Uchida, H. Takagi, K. Kitazawa, and S. Tanaka. *High Tc Superconductivity of La-Ba-Cu Oxides*. Jpn. J. Appl. Phys **26**, L1 (1987). (Cited on page **2**)

[73] Y. Cao, V. Fatemi, S. Fang, K. Watanabe, T. Taniguchi, E. Kaxiras, and P. Jarillo-Herrero. *Unconventional superconductivity in magic-angle graphene superlattices*. Nature **556**, 43–50 (2018). (Cited on pages **2** and **47**)

[74] X. Lu, P. Stepanov, W. Yang, M. Xie, M. A. Aamir, I. Das, C. Urgell, K. Watanabe, T. Taniguchi, G. Zhang, A. Bachtold, A. H. MacDonald, and D. K. Efetov. *Superconductors, orbital magnets and correlated states in magic-angle bilayer graphene*. Nature **574**, 653–657 (2019). (Cited on page **2**)

[75] P. W. Anderson. *The Resonating Valence Bond State in La_2CuO_4 and Superconductivity*. Science **235**, 1196–1198 (1987). (Cited on pages **2**, **7**, and **21**)

[76] M. Troyer and U.-J. Wiese. *Computational Complexity and Fundamental Limitations to Fermionic Quantum Monte Carlo Simulations*. Phys. Rev. Lett. **94**, 170201 (2005). (Cited on page **2**)

[77] M. Qin, C.-M. Chung, H. Shi, E. Vitali, C. Hubig, U. Schollwöck, S. R. White, and S. Zhang. *Absence of Superconductivity in the Pure Two-Dimensional Hubbard Model*. Phys. Rev. X **10**, 031016 (2020). (Cited on pages **2**, **7**, and **14**)

[78] P. Corboz, T. M. Rice, and M. Troyer. *Competing States in the t-J Model: Uniform d-Wave State versus Stripe State*. Phys. Rev. Lett. **113**, 046402 (2014). (Cited on page **2**)

[79] T. A. Maier, M. Jarrell, T. C. Schulthess, P. R. C. Kent, and J. B. White. *Systematic Study of d-Wave Superconductivity in the 2D Repulsive Hubbard Model*. Phys. Rev. Lett. **95**, 237001 (2005). (Cited on page **2**)

[80] A. S. Darmawan, Y. Nomura, Y. Yamaji, and M. Imada. *Stripe and superconducting order competing in the Hubbard model on a square lattice studied by a combined variational Monte Carlo and tensor network method*. Phys. Rev. B **98**, 205132 (2018). (Cited on page **2**)

[81] E. Dagotto, J. Riera, and D. Scalapino. *Superconductivity in ladders and coupled planes*. Phys. Rev. B **45**, 5744–5747 (1992). (Cited on pages **2** and **21**)

[82] M. Sigrist, T. M. Rice, and F. C. Zhang. *Superconductivity in a quasi-one-dimensional spin liquid*. Phys. Rev. B **49**, 12058–12061 (1994). (Cited on pages **2** and **21**)

[83] M. Troyer, H. Tsunetsugu, and T. M. Rice. *Properties of lightly doped t-J two-leg ladders*. Phys. Rev. B **53**, 251–267 (1996). (Cited on pages **2** and **21**)

[84] A. L. Chernyshev, P. W. Leung, and R. J. Gooding. *Comprehensive numerical and analytical study of two holes doped into the two-dimensional $t - J$ model*. Phys. Rev. B **58**, 13594–13613 (1998). (Cited on pages **2**, **19**, **21**, and **68**)

[85] T. Giamarchi. *Quantum physics in one dimension*. International series of monographs on physics. Clarendon Press, Oxford (2004). (Cited on pages **2**, **10**, **16**, **19**, and **21**)

[86] S. R. White. *Density matrix formulation for quantum renormalization groups*. Phys. Rev. Lett. **69**, 2863–2866 (1992). (Cited on pages **3** and **7**)

[87] M. Uehara, T. Nagata, J. Akimitsu, H. Takahashi, N. Môri, and K. Kinoshita. *Superconductivity in the Ladder Material $Sr_{0.4}Ca_{13.6}Cu_{24}O_{41.84}$*. J. Phys. Soc. Japan **65**, 2764–2767 (1996). (Cited on pages **3** and **23**)

[88] T. Nagata, M. Uehara, J. Goto, J. Akimitsu, N. Motoyama, H. Eisaki, S. Uchida, H. Takahashi, T. Nakanishi, and N. Môri. *Pressure-Induced Dimensional Crossover and Superconductivity in the Hole-Doped Two-Leg Ladder Compound* $Sr_{14-x}Ca_xCu_{24}O_{41}$. Phys. Rev. Lett. **81**, 1090–1093 (1998). (Cited on pages **3** and **23**)

[89] E. Dagotto. *Experiments on ladders reveal a complex interplay between a spin-gapped normal state and superconductivity*. Rep. Prog. Phys. **62**, 1525–1571 (1999). (Cited on pages **3**, **21**, and **23**)

[90] J. M. Kosterlitz and D. J. Thouless. *Ordering, metastability and phase transitions in two-dimensional systems*. J. Phys. C Solid State Phys. **6**, 1181 (1973). (Cited on pages **3** and **24**)

[91] L. Landau. *The Theory of Phase Transitions*. Nature **138**, 840–841 (1936). (Cited on pages **3** and **24**)

[92] S. Sachdev. *Quantum Phase Transitions*. Cambridge University Press (2011). (Cited on page **3**)

[93] X.-G. Wen. *Colloquium: Zoo of quantum-topological phases of matter*. Rev. Mod. Phys. **89**, 041004 (2017). (Cited on pages **3**, **24**, and **104**)

[94] M. Aidelsburger, M. Lohse, C. Schweizer, M. Atala, J. T. Barreiro, S. Nascimbène, N. R. Cooper, I. Bloch, and N. Goldman. *Measuring the Chern number of Hofstadter bands with ultracold bosonic atoms*. Nat. Phys. **11**, 162–166 (2015). (Cited on page **3**)

[95] T. Senthil. *Symmetry-Protected Topological Phases of Quantum Matter*. Annu. Rev. Condens. Matter Phys. **6**, 299–324 (2015). (Cited on pages **3** and **24**)

[96] X. Chen, Z.-C. Gu, and X.-G. Wen. *Classification of gapped symmetric phases in one-dimensional spin systems*. Phys. Rev. B **83**, 035107 (2011). (Cited on pages **3**, **24**, and **25**)

[97] D. J. Thouless, M. Kohmoto, M. P. Nightingale, and M. den Nijs. *Quantized Hall Conductance in a Two-Dimensional Periodic Potential*. Phys. Rev. Lett. **49**, 405–408 (1982). (Cited on page **3**)

[98] A. Kitaev. *Anyons in an exactly solved model and beyond*. Ann. Phys. **321**, 2–111 (2006). (Cited on page **3**)

[99] F. D. M. Haldane. *Nonlinear Field Theory of Large-Spin Heisenberg Antiferromagnets: Semiclassically Quantized Solitons of the One-Dimensional Easy-Axis Néel State*. Phys. Rev. Lett. **50**, 1153 (1983). (Cited on pages **3** and **25**)

[100] F. D. M. Haldane. *Topological Quantum Matter*. Int. Journ. Mod. Phys. B **32**, 1830004 (2018). (Cited on pages **3** and **24**)

[101] S. R. White. *Equivalence of the antiferromagnetic Heisenberg ladder to a single S=1 chain*. Phys. Rev. B **53**, 52–55 (1996). (Cited on pages **3**, **19**, **24**, **28**, **84**, and **87**)

[102] A. Auerbach. *Interacting Electrons and Quantum Magnetism*. Graduate Texts in Contemporary Physics. Springer, New York (1994). (Cited on pages **7**, **15**, **25**, and **68**)

[103] J. Hubbard and B. H. Flowers. *Electron correlations in narrow energy bands*. Proc. R. Soc. A **276**, 238–257 (1963). (Cited on page **7**)

[104] E. W. Huang, C. B. Mendl, H.-C. Jiang, B. Moritz, and T. P. Devereaux. *Stripe order from the perspective of the Hubbard model*. npj Quantum Mater. **3**, 22 (2018). (Cited on pages **7** and **14**)

[105] E. Arrigoni, E. Fradkin, and S. A. Kivelson. *Mechanism of high-temperature superconductivity in a striped Hubbard model*. Phys. Rev. B **69** (2004). (Cited on page **7**)

[106] H. Fehske, R. Schneider, and A. Weiße. *Computational Many-Particle Physics*. Lecture Notes in Physics. Springer Berlin Heidelberg (2007). (Cited on page 7)

[107] E. Blomquist and J. Carlström. *Evidence of attraction between charge carriers in a doped Mott insulator*. Phys. Rev. Res **3**, 013272 (2021). (Cited on page 7)

[108] K. K. Nielsen, M. A. Bastarrachea-Magnani, T. Pohl, and G. M. Bruun. *The spatial structure of magnetic polarons in strongly interacting antiferromagnets*. arXiv:2106.14510 (2021). (Cited on page 7)

[109] D. Pines. *Nearly antiferromagnetic Fermi liquids: a progress report*. Z. Phys. B Con. Mat. **103**, 129–135 (1996). (Cited on page 7)

[110] A. Georges, G. Kotliar, W. Krauth, and M. J. Rozenberg. *Dynamical mean-field theory of strongly correlated fermion systems and the limit of infinite dimensions*. Rev. Mod. Phys. **68**, 13–125 (1996). (Cited on page 7)

[111] F. Grusdt, M. Kánasz-Nagy, A. Bohrdt, C. Chiu, G. Ji, M. Greiner, D. Greif, and E. Demler. *Parton Theory of Magnetic Polarons: Mesonic Resonances and Signatures in Dynamics*. Phys. Rev. X **8**, 011046 (2018). (Cited on pages 7 and 16)

[112] C. S. Chiu, G. Ji, A. Bohrdt, M. Xu, M. Knap, E. Demler, F. Grusdt, M. Greiner, and D. Greif. *String patterns in the doped Hubbard model*. Science **365**, 251–256 (2019). (Cited on page 7)

[113] T. Esslinger. *Fermi-Hubbard Physics with Atoms in an Optical Lattice*. Annu. Rev. Condens. Matter Phys. **1**, 129–152 (2010). (Cited on pages 8 and 10)

[114] R. Micnas, J. Ranninger, and S. Robaszkiewicz. *Superconductivity in narrow-band systems with local nonretarded attractive interactions*. Rev. Mod. Phys. **62**, 113–171 (1990). (Cited on page 9)

[115] A. F. Ho, M. A. Cazalilla, and T. Giamarchi. *Quantum simulation of the Hubbard model: The attractive route*. Phys. Rev. A **79** (2009). (Cited on page 9)

[116] R. Staudt, M. Dzierzawa, and A. Muramatsu. *Phase diagram of the three-dimensional Hubbard model at half filling*. Eur. Phys. J. B **17**, 411–415 (2000). (Cited on page 10)

[117] N. D. Mermin and H. Wagner. *Absence of Ferromagnetism or Antiferromagnetism in One- or Two-Dimensional Isotropic Heisenberg Models*. Phys. Rev. Lett. **17**, 1133–1136 (1966). (Cited on page 10)

[118] W. Ketterle and M. W. Zwierlein. *Making, probing and understanding ultracold Fermi gases*. Riv. del Nuovo Cim. **31**, 247–422 (2008). (Cited on page 10)

[119] A. M. Kaufman and K.-K. Ni. *Quantum science with optical tweezer arrays of ultracold atoms and molecules*. Nat. Phys. **17**, 1324–1333 (2021). (Cited on page 10)

[120] I. Bloch. *Ultracold quantum gases in optical lattices*. Nat. Phys. **1**, 23–30 (2005). (Cited on page **10**)

[121] J. Koepsell. *Quantum simulation of doped two-dimensional Mott insulators*. PhD thesis, Ludwig-Maximilians-Universität München (2021). (Cited on pages **11**, **17**, **34**, **36**, **37**, and **57**)

[122] R. Grimm, M. Weidemüller, and Y. B. Ovchinnikov. *Optical Dipole Traps for Neutral Atoms*. In B. Bederson and H. Walther, editors, *Advances In Atomic, Molecular, and Optical Physics*, volume 42, pages 95–170. Academic Press (2000). (Cited on page **11**)

[123] W. Kohn. *Analytic Properties of Bloch Waves and Wannier Functions*. Phys. Rev. **115**, 809–821 (1959). (Cited on page **12**)

[124] A. Mazurenko, C. S. Chiu, G. Ji, M. F. Parsons, M. Kanász-Nagy, R. Schmidt, F. Grusdt, E. Demler, D. Greif, and M. Greiner. *A cold-atom Fermi–Hubbard antiferromagnet*. Nature **545**, 462–466 (2017). (Cited on pages **12**, **13**, and **48**)

[125] A. Wietek, Y.-Y. He, S. R. White, A. Georges, and E. M. Stoudenmire. *Stripes, Antiferromagnetism, and the Pseudogap in the Doped Hubbard Model at Finite Temperature*. Phys. Rev. X **11**, 031007 (2021). (Cited on page **12**)

[126] S. Karakuzu, S. Johnston, and T. A. Maier. *Superconductivity in the bilayer Hubbard model: Two Fermi surfaces are better than one*. Phys. Rev. B **104**, 245109 (2021). (Cited on page **12**)

[127] T. Hilker. *Spin-resolved microscopy of strongly correlated fermionic many-body states*. PhD thesis, Ludwig-Maximilians-Universität München (2017). (Cited on pages **13** and **33**)

[128] L. R. B. Picard, M. J. Mark, F. Ferlaino, and R. v. Bijnen. *Deep learning-assisted classification of site-resolved quantum gas microscope images*. Meas. Sci. Technol. **31**, 025201 (2019). (Cited on page **13**)

[129] W. S. Bakr, J. I. Gillen, A. Peng, S. Fölling, and M. Greiner. *A quantum gas microscope for detecting single atoms in a Hubbard-regime optical lattice*. Nature **462**, 74–77 (2009). (Cited on page **13**)

[130] P. T. Brown, D. Mitra, E. Guardado-Sanchez, P. Schauß, S. S. Kondov, E. Khatami, T. Paiva, N. Trivedi, D. A. Huse, and W. S. Bakr. *Spin-imbalance in a 2D Fermi-Hubbard system*. Science **357**, 1385–1388 (2017). (Cited on page **13**)

[131] G. A. Phelps, A. Hébert, A. Krahn, S. Dickerson, F. Öztürk, S. Ebadi, L. Su, and M. Greiner. *Sub-second production of a quantum degenerate gas*. arXiv:2007.10807 (2020). (Cited on page **14**)

[132] A. Altland and B. D. Simons. *Condensed matter field theory*. Cambridge University Press, Cambridge, second edition (2010). (Cited on page **14**)

[133] M. R. Norman, D. Pines, and C. Kallin. *The pseudogap: friend or foe of high T c ?* Adv. Phys. **54**, 715–733 (2005). (Cited on page **14**)

[134] A. P. Mackenzie, S. R. Julian, D. C. Sinclair, and C. T. Lin. *Normal-state magneto-transport in superconducting* $Tl_2Ba_2CuO_{6+ffi}$ *to millikelvin temperatures.* Phys. Rev. B **53**, 5848–5855 (1996). (Cited on page **14**)

[135] T. I. Vanhala and P. Törmä. *Dynamical mean-field theory study of stripe order and d-wave superconductivity in the two-dimensional Hubbard model.* Phys. Rev. B **97**, 075112 (2018). (Cited on page **14**)

[136] H. Yokoyama and H. Shiba. *Variational Monte-Carlo Studies of Superconductivity in Strongly Correlated Electron Systems.* J. Phys. Soc. Japan **57**, 2482–2493 (1988). (Cited on page **14**)

[137] M. Qin, H. Shi, and S. Zhang. *Benchmark study of the two-dimensional Hubbard model with auxiliary-field quantum Monte Carlo method.* Phys. Rev. B **94**, 085103 (2016). (Cited on page **14**)

[138] C. Kollath and U. Schollwöck. *Cold Fermi gases: a new perspective on spin-charge separation.* New J. Phys **8**, 220–220 (2006). (Cited on page **16**)

[139] F. D. M. Haldane. *Effective Harmonic-Fluid Approach to Low-Energy Properties of One-Dimensional Quantum Fluids.* Phys. Rev. Lett. **47**, 1840–1843 (1981). (Cited on page **16**)

[140] F. D. M. Haldane. *'Luttinger liquid theory' of one-dimensional quantum fluids. I. Properties of the Luttinger model and their extension to the general 1D interacting spinless Fermi gas.* J. Phys. C Solid State Phys. **14**, 2585–2609 (1981). (Cited on page **16**)

[141] T. A. Hilker, G. Salomon, F. Grusdt, A. Omran, M. Boll, E. Demler, I. Bloch, and C. Gross. *Revealing hidden antiferromagnetic correlations in doped Hubbard chains via string correlators.* Science **357**, 484–487 (2017). (Cited on page **16**)

[142] G. Salomon, J. Koepsell, J. Vijayan, T. A. Hilker, J. Nespolo, L. Pollet, I. Bloch, and C. Gross. *Direct observation of incommensurate magnetism in Hubbard chains.* Nature **565**, 56–60 (2019). (Cited on page **16**)

[143] J. Vijayan. *Microscopy of spin-charge dynamics in Fermi-Hubbard chains.* PhD thesis, Ludwig-Maximilians-Universität München (2020). (Cited on pages **16** and **57**)

[144] J. R. Schrieffer and J. S. Brooks. *Handbook of high-temperature superconductivity: theory and experiment.* Springer (2007). (Cited on page **16**)

[145] F. Ronning, K. M. Shen, N. P. Armitage, A. Damascelli, D. H. Lu, Z.-X. Shen, L. L. Miller, and C. Kim. *Anomalous high-energy dispersion in angle-resolved photoemission spectra from the insulating cuprate* $Ca_2CuO_2Cl_2$. Phys. Rev. B **71**, 094518 (2005). (Cited on page **16**)

[146] J. Koepsell, J. Vijayan, P. Sompet, F. Grusdt, T. A. Hilker, E. Demler, G. Salomon, I. Bloch, and C. Gross. *Imaging magnetic polarons in the doped Fermi–Hubbard model*. Nature **572**, 358–362 (2019). (Cited on page **16**)

[147] G. Ji, M. Xu, L. H. Kendrick, C. S. Chiu, J. C. Brüggenjürgen, D. Greif, A. Bohrdt, F. Grusdt, E. Demler, M. Lebrat, and M. Greiner. *Coupling a Mobile Hole to an Antiferromagnetic Spin Background: Transient Dynamics of a Magnetic Polaron*. Phys. Rev. X **11**, 021022 (2021). (Cited on page **17**)

[148] S. R. White and D. J. Scalapino. *Why do stripes form in doped antiferromagnets and what is their relationship to superconductivity?* arXiv:cond-mat/0006071 (2000). (Cited on page **18**)

[149] J. M. Tranquada, B. J. Sternlieb, J. D. Axe, Y. Nakamura, and S. Uchida. *Evidence for stripe correlations of spins and holes in copper oxide superconductors*. Nature **375**, 561–563 (1995). (Cited on page **18**)

[150] D. J. Scalapino and S. R. White. *Superconducting condensation energy and an antiferromagnetic exchange-based pairing mechanism*. Phys. Rev. B **58**, 8222–8224 (1998). (Cited on page **18**)

[151] S. Zhang, J. Carlson, and J. E. Gubernatis. *Pairing Correlations in the Two-Dimensional Hubbard Model*. Phys. Rev. Lett. **78**, 4486–4489 (1997). (Cited on page **18**)

[152] D. Sénéchal, P.-L. Lavertu, M.-A. Marois, and A.-M. S. Tremblay. *Competition between Antiferromagnetism and Superconductivity in High-T_c Cuprates*. Phys. Rev. Lett. **94**, 156404 (2005). (Cited on page **18**)

[153] B.-X. Zheng and G. K.-L. Chan. *Ground-state phase diagram of the square lattice Hubbard model from density matrix embedding theory*. Phys. Rev. B **93**, 035126 (2016). (Cited on page **18**)

[154] E. Dagotto and T. M. Rice. *Surprises on the Way from One- to Two-Dimensional Quantum Magnets: The Ladder Materials*. Science **271**, 618–623 (1996). (Cited on pages **19** and **20**)

[155] H. J. Schulz. *Metal-insulator transition in the two-chain model of correlated fermions*. Phys. Rev. B **59**, R2471–R2473 (1999). (Cited on pages **19**, **22**, **48**, **50**, and **68**)

[156] K. Hida. *Crossover between the Haldane-gap phase and the dimer phase in the spin-1/2 alternating Heisenberg chain*. Phys. Rev. B **45**, 2207 (1992). (Cited on pages **19** and **28**)

[157] M. Atala, M. Aidelsburger, M. Lohse, J. T. Barreiro, B. Paredes, and I. Bloch. *Observation of chiral currents with ultracold atoms in bosonic ladders*. Nat. Phys. **10**, 588–593 (2014). (Cited on page **19**)

[158] M. E. Tai, A. Lukin, M. Rispoli, R. Schittko, T. Menke, D. Borgnia, P. M. Preiss, F. Grusdt, A. M. Kaufman, and M. Greiner. *Microscopy of the interacting Harper–Hofstadter model in the two-body limit*. Nature **546**, 519–523 (2017). (Cited on pages **19** and **23**)

[159] R. Sachdeva, F. Metz, M. Singh, T. Mishra, and T. Busch. *Two-leg-ladder Bose-Hubbard models with staggered fluxes*. Phys. Rev. A **98** (2018). (Cited on page **19**)

[160] J. Klinovaja and D. Loss. *Fractional Fermions with Non-Abelian Statistics*. Phys. Rev. Lett. **110**, 126402 (2013). (Cited on page **19**)

[161] M. Kardar. *Josephson-junction ladders and quantum fluctuations*. Phys. Rev. B **33**, 3125 (1986). (Cited on page **19**)

[162] C. Denniston and C. Tang. *Phases of Josephson junction ladders*. Phys. Rev. Lett. **75**, 3930 (1995). (Cited on page **19**)

[163] E. Granato. *Phase transitions in Josephson-junction ladders in a magnetic field*. Phys. Rev. B **42**, 4797 (1990). (Cited on page **19**)

[164] E. Orignac and T. Giamarchi. *Meissner effect in a bosonic ladder*. Phys. Rev. B **64**, 144515 (2001). (Cited on page **19**)

[165] F. D. M. Haldane. *Continuum dynamics of the 1-D Heisenberg antiferromagnet: Identification with the O(3) nonlinear sigma model*. Phys. lett., A **93**, 464–468 (1983). (Cited on pages **21**, **24**, and **25**)

[166] T. F. A. Müller and T. M. Rice. *Phase diagram of coupled ladders*. Phys. Rev. B **58**, 3425–3437 (1998). (Cited on pages **21** and **22**)

[167] L. Balents and M. P. A. Fisher. *Weak-coupling phase diagram of the two-chain Hubbard model*. Phys. Rev. B **53**, 12133–12141 (1996). (Cited on page **21**)

[168] Z. Weihong, J. Oitmaa, C. J. Hamer, and R. J. Bursill. *Numerical studies of the two-leg Hubbard ladder*. J. Phys. Condens. Matter **13**, 433–448 (2000). (Cited on page **22**)

[169] Z. Zhu, Z.-Y. Weng, and T.-L. Ho. *Spin and charge modulations in a single-hole-doped Hubbard ladder: Verification with optical lattice experiments*. Phys. Rev. A **93** (2016). (Cited on page **22**)

[170] C. Jurecka and W. Brenig. *Two-Hole Dynamics in Spin Ladders*. J. Low Temp. Phys. **126**, 1165–1183 (2002). (Cited on page **22**)

[171] Z. Hiroi, M. Azuma, M. Takano, and Y. Bando. *A new homologous series Srn-1Cun+1O2n found in the SrO-CuO system treated under high pressure*. J. Solid State Chem. **95**, 230–238 (1991). (Cited on page **23**)

[172] M. Takano. *SrCuO2 and related high-pressure phases*. J. supercond. **7**, 49–54 (1994). (Cited on page **23**)

[173] M. Azuma, Z. Hiroi, M. Takano, K. Ishida, and Y. Kitaoka. *Observation of a Spin Gap in SrCu$_2$ O$_3$ Comprising Spin-1/2 Quasi-1D Two-Leg Ladders*. Phys. Rev. Lett. **73**, 3463–3466 (1994). (Cited on page **23**)

[174] H. Szymczak, R. Szymczak, M. Baran, L. Leonyuk, G. J. Babonas, and V. Maltsev. *Superconductivity and Magnetic Properties of Spin-Ladder Compounds*. In *New Developments in High Temperature Superconductivity*, pages 157–180, Berlin, Heidelberg (2000). Springer Berlin Heidelberg. (Cited on page **23**)

[175] M. Atala, M. Aidelsburger, J. T. Barreiro, D. Abanin, T. Kitagawa, E. Demler, and I. Bloch. *Direct measurement of the Zak phase in topological Bloch bands*. Nat. Phys. **9**, 795–800 (2013). (Cited on page **23**)

[176] W. Meissner and R. Ochsenfeld. *Ein neuer Effekt bei Eintritt der Supraleitfähigkeit*. Sci. Nat. **21**, 787–788 (1933). (Cited on page **23**)

[177] J. M. Kosterlitz and D. J. Thouless. *Long range order and metastability in two dimensional solids and superfluids. (Application of dislocation theory)*. J. Phys. C Solid State Phys. **5**, L124 (1972). (Cited on page **24**)

[178] M. Lohse, C. Schweizer, O. Zilberberg, M. Aidelsburger, and I. Bloch. *A Thouless quantum pump with ultracold bosonic atoms in an optical superlattice*. Nat. Phys. **12**, 350–354 (2016). (Cited on pages **24** and **41**)

[179] A. Stern. *Fractional Topological Insulators: A Pedagogical Review*. Annu. Rev. Condens. Matter Phys. **7**, 349–368 (2016). (Cited on page **24**)

[180] E. Dennis, A. Kitaev, A. Landahl, and J. Preskill. *Topological quantum memory*. J. Math. Phys. **43**, 4452–4505 (2002). (Cited on page **24**)

[181] C. Nayak, S. H. Simon, A. Stern, M. Freedman, and S. Das Sarma. *Non-Abelian anyons and topological quantum computation*. Rev. Mod. Phys. **80**, 1083–1159 (2008). (Cited on page **24**)

[182] A. Kitaev. *Fault-tolerant quantum computation by anyons*. Ann. Phys. (N. Y.) **303**, 2–30 (2003). (Cited on page **24**)

[183] X.-G. Wen. *Symmetry-protected topological invariants of symmetry-protected topological phases of interacting bosons and fermions*. Phys. Rev. B **89** (2014). (Cited on page **24**)

[184] K. v. Klitzing, G. Dorda, and M. Pepper. *New Method for High-Accuracy Determination of the Fine-Structure Constant Based on Quantized Hall Resistance*. Phys. Rev. Lett. **45**, 494–497 (1980). (Cited on page **24**)

[185] C. L. Kane and E. J. Mele. *Quantum Spin Hall Effect in Graphene*. Phys. Rev. Lett. **95**, 226801 (2005). (Cited on page **24**)

[186] N. Schuch, D. Pérez-García, and I. Cirac. *Classifying Quantum Phases Using Matrix Product States and Projected Entangled Pair States*. Phys. Rev. B **84**, 165139 (2011). (Cited on page **24**)

[187] F. Pollmann, A. M. Turner, E. Berg, and M. Oshikawa. *Entanglement spectrum of a topological phase in one dimension*. Phys. Rev. B **81**, 064439 (2010). (Cited on pages **24** and **25**)

[188] M. Ogata and H. Shiba. *Bethe-ansatz wave function, momentum distribution, and spin correlation in the one-dimensional strongly correlated Hubbard model*. Phys. Rev. B **41**, 2326 (1990). (Cited on page **25**)

[189] I. Affleck, T. Kennedy, E. H. Lieb, and H. Tasaki. *Rigorous results on valence-bond ground states in antiferromagnets*. Phys. Rev. Lett. **59**, 799–802 (1987). (Cited on page **25**)

[190] T. Kennedy and H. Tasaki. *Hidden Z2xZ2 Symmetry Breaking in Haldane-Gap Antiferromagnets*. Phys. Rev. B **45**, 304 (1992). (Cited on page **25**)

[191] F. Anfuso and A. Rosch. *Fragility of string orders*. Phys. Rev. B **76**, 085124 (2007). (Cited on page **28**)

[192] R. Verresen, R. Moessner, and F. Pollmann. *One-dimensional symmetry protected topological phases and their transitions*. Phys. Rev. B **96**, 165124 (2017). (Cited on page **28**)

[193] R. Verresen, J. Bibo, and F. Pollmann. *Quotient symmetry protected topological phenomena*. arXiv:2102.08967 (2021). (Cited on page **28**)

[194] M. den Nijs and K. Rommelse. *Preroughening Transitions in Crystal Surfaces and Valence-Bond Phases in Quantum Spin Chains*. Phys. Rev. B **40**, 4709 (1989). (Cited on page **30**)

[195] F. Pollmann and A. M. Turner. *Detection of symmetry-protected topological phases in one dimension*. Phys. Rev. B **86**, 125441 (2012). (Cited on pages **30**, **31**, and **87**)

[196] A. Omran. *A microscope for Fermi gases*. PhD thesis, Ludwig-Maximilians-Universität München (2016). (Cited on pages **33** and **35**)

[197] M. Boll. *Spin and density resolved microscopy of Hubbard chains*. PhD thesis, Ludwig-Maximilians-Universität München (2016). (Cited on pages **33** and **37**)

[198] F. Serwane, G. Zürn, T. Lompe, T. B. Ottenstein, A. N. Wenz, and S. Jochim. *Deterministic Preparation of a Tunable Few-Fermion System*. Science **332**, 336–338 (2011). (Cited on page **33**)

[199] W. Weimer, K. Morgener, V. P. Singh, J. Siegl, K. Hueck, N. Luick, L. Mathey, and H. Moritz. *Critical Velocity in the BEC-BCS Crossover*. Phys. Rev. Lett. **114**, 095301 (2015). (Cited on page **33**)

[200] T. Bourdel, L. Khaykovich, J. Cubizolles, J. Zhang, F. Chevy, M. Teichmann, L. Tarruell, S. J. J. M. F. Kokkelmans, and C. Salomon. *Experimental Study of the BEC-BCS Crossover Region in Lithium 6*. Phys. Rev. Lett. **93**, 050401 (2004). (Cited on page **33**)

[201] A. G. Truscott, K. E. Strecker, W. I. McAlexander, G. B. Partridge, and R. G. Hulet. *Observation of Fermi Pressure in a Gas of Trapped Atoms*. Science **291**, 2570–2572 (2001). (Cited on page **33**)

[202] W. Ketterle and M. W. Zwierlein. *Making, probing and understanding ultracold Fermi gases*. arXiv:0801.2500 (2008). (Cited on pages **33** and **34**)

[203] M. E. Gehm. *Properties of ^6Li*. (2003). (Cited on page **33**)

[204] P. M. Duarte, R. A. Hart, J. M. Hitchcock, T. A. Corcovilos, T.-L. Yang, A. Reed, and R. G. Hulet. *All-optical production of a lithium quantum gas using narrow-line laser cooling*. Phys. Rev. A **84**, 061406 (2011). (Cited on page **33**)

[205] C. Chin, R. Grimm, P. Julienne, and E. Tiesinga. *Feshbach resonances in ultracold gases*. Rev. Mod. Phys. **82**, 1225–1286 (2010). (Cited on page **34**)

[206] M. S. Safronova, U. I. Safronova, and C. W. Clark. *Magic wavelengths for optical cooling and trapping of lithium*. Phys. Rev. A **86**, 042505 (2012). (Cited on page **35**)

[207] D. Bourgund. *High-Stability, Tunable, Bichromatic Superlattice*. Master's thesis, LMU München (2019). (Cited on pages **36** and **104**)

[208] W. Ketterle and N. J. Van Druten. *Evaporative cooling of trapped atoms*. Adv. At. Mol. Opt. Phys. **37**, 181–236 (1996). (Cited on page **36**)

[209] S. Hild. *Microscopy of quantum many-body systems out of equilibrium*. PhD thesis, Ludwig-Maximilians-Universität München (2016). (Cited on page **37**)

[210] D. Wei. *Development of a Spatially Incoherent Laser Source*. Theses, Fakultat für Physik der Technischen Universität München (2019). (Cited on page **38**)

[211] R. W. Floyd and L. Steinberg. *An Adaptive Algorithm for Spatial Greyscale*. Proceedings of the Society for Information Display **17**, 75–77 (1976). (Cited on page **39**)

[212] A. Mazurenko. *Probing Long Range Antiferromagnetism and Dynamics in the Fermi-Hubbard Model*. PhD thesis (2017). (Cited on pages **39** and **105**)

[213] M. F. Parsons. *Probing the Hubbard Model With Single-Site Resolution*. PhD thesis, Harvard University (2016). (Cited on page **39**)

[214] D. J. Thouless. *Quantization of particle transport*. Phys. Rev. B **27**, 6083–6087 (1983). (Cited on page **41**)

[215] O. Romero-Isart and J. J. García-Ripoll. *Quantum ratchets for quantum communication with optical superlattices*. Phys. Rev. A **76**, 052304 (2007). (Cited on page **41**)

[216] J. Koepsell, D. Bourgund, P. Sompet, S. Hirthe, A. Bohrdt, Y. Wang, F. Grusdt, E. Demler, G. Salomon, C. Gross, and I. Bloch. *Microscopic evolution of doped Mott insulators from polaronic metal to Fermi liquid*. Science **374**, 82–86 (2021). (Cited on page **42**)

[217] Grafana Labs 2021 Grafana: the open observability platform https://grafana.com. (Cited on page **45**)

[218] C. Varma. *Mind the pseudogap*. Nature **468**, 184–185 (2010). (Cited on page **48**)

[219] A. Fischer, Z. A. H. Goodwin, A. A. Mostofi, J. Lischner, D. M. Kennes, and L. Klebl. *Unconventional superconductivity in magic-angle twisted trilayer graphene*. npj Quantum Mater. **7**, 5 (2022). (Cited on page **48**)

[220] G. Knebel, D. Aoki, and J. Flouquet. *Antiferromagnetism and superconductivity in cerium based heavy-fermion compounds*. C. R. Phys. **12**, 542–566 (2011). (Cited on page **48**)

[221] A. Bohrdt, L. Homeier, I. Bloch, E. Demler, and F. Grusdt. *Strong pairing in mixed-dimensional bilayer antiferromagnetic Mott insulators*. Nature Physics **18**, 651–656 (2022). (Cited on pages **48**, **50**, **52**, **68**, **74**, **76**, **77**, and **104**)

[222] F. Grusdt, Z. Zhu, T. Shi, and E. Demler. *Meson formation in mixed-dimensional t-J models*. SciPost Phys. **5**, 057 (2018). (Cited on page **50**)

[223] L.-M. Duan, E. Demler, and M. D. Lukin. *Controlling Spin Exchange Interactions of Ultracold Atoms in Optical Lattices*. Phys. Rev. Lett. **91**, 090402 (2003). (Cited on page **51**)

[224] S. Trotzky, P. Cheinet, S. Fölling, M. Feld, U. Schnorrberger, A. M. Rey, A. Polkovnikov, E. A. Demler, M. D. Lukin, and I. Bloch. *Time-Resolved Observation and Control of Superexchange Interactions with Ultracold Atoms in Optical Lattices*. Science **319**, 295–299 (2008). (Cited on page **51**)

[225] D. J. Griffiths and D. F. Schroeter. *Introduction to Quantum Mechanics*. Cambridge University Press, 3 edition (2018). (Cited on page **51**)

[226] S. R. White and D. J. Scalapino. *Hole and pair structures in the t-J model*. Phys. Rev. B **55**, 6504–6517 (1997). (Cited on page **68**)

[227] G. Karakonstantakis, E. Berg, S. R. White, and S. A. Kivelson. *Enhanced pairing in the checkerboard Hubbard ladder*. Phys. Rev. B **83**, 054508 (2011). (Cited on page **68**)

[228] J. Friedel. *XIV. The Distribution of Electrons Round Impurities in Monovalent Metals*. Lond. Edinb. Dublin philos. mag. j. sci. **43**, 153–189 (1952). (Cited on page **74**)

[229] S. R. White, I. Affleck, and D. J. Scalapino. *Friedel oscillations and charge density waves in chains and ladders*. Phys. Rev. B **65**, 165122 (2002). (Cited on page **74**)

[230] H. Schlömer, A. Bohrdt, L. Pollet, U. Schollwöck, and F. Grusdt. *Robust stripes in the mixed-dimensional $t - J$ model*. arXiv:2208.07366 (2022). (Cited on page 76)

[231] S.-S. Zhang, W. Zhu, and C. D. Batista. *Pairing from strong repulsion in triangular lattice Hubbard model*. Phys. Rev. B **97** (2018). (Cited on page 77)

[232] Z.-D. Song and B. A. Bernevig. *MATBG as Topological Heavy Fermion: I. Exact Mapping and Correlated Insulators* (2021). (Cited on page 77)

[233] G. Blumberg, P. Littlewood, A. Gozar, B. S. Dennis, N. Motoyama, H. Eisaki, and S. Uchida. *Sliding Density Wave in $Sr_{14}Cu_{24}O_{41}$ Ladder Compounds*. Science **297**, 584–587 (2002). (Cited on page 77)

[234] M. S. Golden, C. Dürr, A. Koitzsch, S. Legner, Z. Hu, S. Borisenko, M. Knupfer, and J. Fink. *The electronic structure of cuprates from high energy spectroscopy*. J. Electron Spectrosc. Relat. Phenom. **117-118**, 203–222 (2001). (Cited on page 77)

[235] S. Chaudhary, D. Hsieh, and G. Refael. *Orbital Floquet engineering of exchange interactions in magnetic materials*. Phys. Rev. B **100** (2019). (Cited on page 77)

[236] Scientifc Background on the Nobel Prize in Physics 2016. *Topological Phase Transitions and Topological Phases of Matter*. Class for Physics of the Royal Swedish Academy of Sciences (2016). (Cited on page 79)

[237] W. J. L. Buyers, R. M. Morra, R. L. Armstrong, M. J. Hogan, P. Gerlach, and K. Hirakawa. *Experimental evidence for the Haldane gap in a spin-1 nearly isotropic, antiferromagnetic chain*. Phys. Rev. Lett. **56**, 371–374 (1986). (Cited on page 79)

[238] M. Hagiwara, K. Katsumata, I. Affleck, B. I. Halperin, and J. P. Renard. *Observation of S=1/2 Degrees of Freedom in an S=1 Linear-Chain Heisenberg Antiferromagnet*. Phys. Rev. Lett. **65**, 3181 (1990). (Cited on page 79)

[239] S. H. Glarum, S. Geschwind, K. M. Lee, M. L. Kaplan, and J. Michel. *Observation of fractional spin S=1/2 on open ends of S=1 linear antiferromagnetic chains: Nonmagnetic doping*. Phys. Rev. Lett. **67**, 1614 (1991). (Cited on page 79)

[240] S. d. Léséleuc, V. Lienhard, P. Scholl, D. Barredo, S. Weber, N. Lang, H. P. Büchler, T. Lahaye, and A. Browaeys. *Observation of a symmetry-protected topological phase of interacting bosons with Rydberg atoms*. Science **365**, eaav9105 (2019). (Cited on page 80)

[241] S. Miyashita and S. Yamamoto. *Effects of edges in S=1 Heisenberg antiferromagnetic chains*. Phys. Rev. B **48**, 913–919 (1993). (Cited on page 92)

[242] H. J. Schulz. *Phase diagrams and correlation exponents for quantum spin chains of arbitrary spin quantum number*. Phys. Rev. B **34**, 6372 (1986). (Cited on page 101)

[243] H. L. Nourse, I. P. McCulloch, C. Janani, and B. J. Powell. *Haldane insulator protected by reflection symmetry in the doped Hubbard model on the three-legged ladder*. Phys. Rev. B **94**, 214418 (2016). (Cited on page 101)

[244] A. Szasz, J. Motruk, M. P. Zaletel, and J. E. Moore. *Chiral Spin Liquid Phase of the Triangular Lattice Hubbard Model : A Density Matrix Renormalization Group Study*. Phys. Rev. X **10**, 21042 (2020). (Cited on page **101**)

[245] I. Pogorelov, T. Feldker, C. D. Marciniak, L. Postler, G. Jacob, O. Krieglsteiner, V. Podlesnic, M. Meth, V. Negnevitsky, M. Stadler, B. Höfer, C. Wächter, K. Lakhmanskiy, R. Blatt, P. Schindler, and T. Monz. *Compact Ion-Trap Quantum Computing Demonstrator*. PRX Quantum **2**, 020343 (2021). (Cited on page **104**)

[246] N. Lorenz. *A Rydberg tweezer platform with potassium atoms*. PhD thesis, Ludwig-Maximilians-Universität München (2021). (Cited on page **104**)

[247] A. Kantian, S. Langer, and A. Daley. *Dynamical Disentangling and Cooling of Atoms in Bilayer Optical Lattices*. Phys. Rev. Lett. **120**, 060401 (2018). (Cited on page **105**)

[248] B. Yang, H. Sun, C.-J. Huang, H.-Y. Wang, Y. Deng, H.-N. Dai, Z.-S. Yuan, and J.-W. Pan. *Cooling and entangling ultracold atoms in optical lattices*. Science **369**, 550–553 (2020). (Cited on page **105**)

[249] D. Wei, A. Rubio-Abadal, B. Ye, F. Machado, J. Kemp, K. Srakaew, S. Hollerith, J. Rui, S. Gopalakrishnan, N. Y. Yao, I. Bloch, and J. Zeiher. *Quantum gas microscopy of Kardar-Parisi-Zhang superdiffusion*. Science **376**, 716–720 (2022). (Cited on page **105**)

[250] L. Asteria, H. P. Zahn, M. N. Kosch, K. Sengstock, and C. Weitenberg. *Quantum gas magnifier for sub-lattice-resolved imaging of 3D quantum systems*. Nature **599**, 571–575 (2021). (Cited on page **105**)

[251] M. Gall, N. Wurz, J. Samland, C. F. Chan, and M. Köhl. *Competing magnetic orders in a bilayer Hubbard model with ultracold atoms*. Nature **589**, 40–43 (2021). (Cited on page **105**)

[252] S. Okamoto and T. A. Maier. *Enhanced Superconductivity in Superlattices of High-T_c Cuprates*. Phys. Rev. Lett. **101**, 156401 (2008). (Cited on page **105**)

[253] T. A. Maier and D. J. Scalapino. *Pair structure and the pairing interaction in a bilayer Hubbard model for unconventional superconductivity*. Phys. Rev. B **84**, 180513 (2011). (Cited on page **105**)

[254] T.-S. Huang, C. L. Baldwin, M. Hafezi, and V. Galitski. *Spin-Mediated Mott Excitons*. arXiv:2004.10825 (2020). (Cited on page **105**)

[255] T. Calarco, E. A. Hinds, D. Jaksch, J. Schmiedmayer, J. I. Cirac, and P. Zoller. *Quantum gates with neutral atoms: Controlling collisional interactions in time-dependent traps*. Phys. Rev. A **61** (2000). (Cited on page **105**)

[256] W.-Y. Zhang, M.-G. He, H. Sun, Y.-G. Zheng, Y. Liu, A. Luo, H.-Y. Wang, Z.-H. Zhu, P.-Y. Qiu, Y.-C. Shen, X.-K. Wang, W. Lin, S.-T. Yu, B.-C. Li, B. Xiao, M.-D.

Li, Y.-M. Yang, X. Jiang, H.-N. Dai, Y. Zhou, X. Ma, Z.-S. Yuan, and J.-W. Pan. *Functional building blocks for scalable multipartite entanglement in optical lattices.* arXiv:2210.02936 (2022). (Cited on page **105**)

[257] Z. Z. Yan, B. M. Spar, M. L. Prichard, S. Chi, H.-T. Wei, E. Ibarra-García-Padilla, K. R. Hazzard, and W. S. Bakr. *Two-Dimensional Programmable Tweezer Arrays of Fermions.* Phys. Rev. Lett. **129** (2022). (Cited on page **106**)

[258] I. Arrazola, J. S. Pedernales, L. Lamata, and E. Solano. *Digital-Analog Quantum Simulation of Spin Models in Trapped Ions.* Scientific Reports **6**, 30534 (2016). (Cited on page **106**)

[259] D. V. Babukhin, A. A. Zhukov, and W. V. Pogosov. *Hybrid digital-analog simulation of many-body dynamics with superconducting qubits.* Phys. Rev. A **101**, 052337 (2020). (Cited on page **106**)

[260] The Fermion Quantum Processor is currently constructed under a grant from the German Federal Ministry of Education and Research (BMBF grant agreement 13N15890, FermiQP). (Cited on page **106**)

[261] A. Bohrdt, L. Homeier, C. Reinmoser, E. Demler, and F. Grusdt. *Exploration of doped quantum magnets with ultracold atoms.* Ann. Phys. **435**, 168651 (2021). (Cited on page **107**)

[262] R. K. Pathria. *Statistical mechanics.* Elsevier (2016). (Cited on page **107**)

[263] J. Hauschild, R. Mong, F. Pollmann, M. Schulz, L. Schoonderwoert, J. Unfried, Y. Tzeng, and M. Zaletel. *Tensor Network Python.* The code is available online at https://github.com/tenpy/tenpy/, the documentation can be found at https://tenpy.github.com/. (2018). (Cited on pages **109** and **110**)

[264] J. Hauschild and F. Pollmann. *Efficient numerical simulations with Tensor Networks: Tensor Network Python (TeNPy).* SciPost Phys. Lect. Notes page 5 (2018). (Cited on page **109**)

[265] F. Verstraete, J. J. García-Ripoll, and J. I. Cirac. *Matrix Product Density Operators: Simulation of Finite-Temperature and Dissipative Systems.* Phys. Rev. Lett. **93**, 207204 (2004). (Cited on page **109**)

[266] U. Schollwöck. *The density-matrix renormalization group in the age of matrix product states.* Ann. Phys. **326**, 96–192 (2011). (Cited on page **109**)

[267] A. Nocera and G. Alvarez. *Symmetry-conserving purification of quantum states within the density matrix renormalization group.* Phys. Rev. B **93**, 045137 (2016). (Cited on page **109**)

[268] M. P. Zaletel, R. S. K. Mong, C. Karrasch, J. E. Moore, and F. Pollmann. *Time-evolving a matrix product state with long-ranged interactions.* Phys. Rev. B **91**, 165112 (2015). (Cited on page **109**)

[269] A. J. Ferris and G. Vidal. *Perfect sampling with unitary tensor networks*. Phys. Rev. B **85**, 165146 (2012). (Cited on page **109**)

Acknowledgements

In the last $1 + 4$ years I've spent most of my time in MPQ. I've learned a hell of a lot, met great people, had good times and hard times. Doing a PhD in the lithium lab can be tough sometimes, but I would do it again. And there are so many people I want to thank for sharing this time with me.

- Immanuel Bloch, for giving me the opportunity to do a PhD in his team. For sharing his knowledge, and also his excitement for physics with us. But also for treating us fairly, and for always making time when we come with a personal issue. He might send messages around the clock, but he never lets you wait long for an answer.

- Timon Hilker, our lab leader, who we've seen grow into this position in the last two and a half years. His excitement for the physics is really great. I also highly appreciate that the cares about his team members and spends time with us, for example for extended discussions over a coffee, despite a very busy schedule.

- Christian Gross, for sparking my passion for experimental physics during my Master's project in his potassium lab, and for initiating my transfer to the lithium lab, which he was leading at the beginning of my PhD. I admire his problem solving skills and he shaped my way of working in the lab.

- Dominik Bourgund, for sharing basically the full time of my PhD with me. I think over the years we became a great team. I also want to thank him for our weekly gym workout, which I enjoyed a lot and which helped to release some stress. He is the person I probably shared most time, most pain and most dreams with and I will miss working with him.

- Thomas Chalopin, for bringing his skill, brain, and kindness to our team when he joined us as a postdoc. I want to thank him for so many late-evening beers in the group room, both with and without alcohol. For great discussions, some about physics but mostly about the rest of the world.

- Petar Bojović, for joining the lab as a PhD student after Dominik and me, and for coping with us being stressed and having our own heads. He is a good friend who is always there to help, in and outside of the lab, when I needed help fixing the car, access to overleaf, or just craved for some delicious ajvar.

- Joannis Koepsell, the senior PhD student in my first 1-2 years, for teaching me everything about our machine and the Fermi-Hubbard model. I was always impressed by his knowledge and his dedication.

- Jayadev Vijayan, the other senior PhD student in my first year, who I thank for making me feel welcome and appreciated in the beginning. He is a clever guy and a very good person.

- Pimonpan (Mim) Sompet, the postdoc of my first two years. She always solved every problem, no matter how much patience and persistence it took.

- The 'single atoms', my second favorite lab after the lithium. Thank you for all the Honghong dinners our labs shared, for the running group, and for some of the activities outside of MPQ. Thanks a lot especially to Simon Hollerith and Pascal Weckesser, but also to David Wei, Kritsana (Cake) Srakaev, and Daniel Adler. You make a great team and I will miss you.

- Annabelle Bohrdt, for being a great collaborator who fulfilled all my wishes for theory simulations, no matter how many parameters I asked for. She also patiently answered all my physics questions and helped me understand so many aspects of hole pairing.

- Marcel, Denise, and Livi Duda, for being great friends who were there to cheer me up whenever I had a bad day. They are a lot of fun and a very cute family. I wish them all the best for their future.

- Kristina Schuldt for being an irreplaceable part of our group who always manages to solve problems in no time. She was also a great gender equality officer and very helpful to us new GEOs.

- Eileen Welz, Flore Kunst and Charlotte Huber for the most enjoyable meetings and for being great gender equality officers. I really appreciated having them around at MPQ.

- So many other people who made and make MPQ a great place like the potassium lab with Nikolaus Lorenz, Lorenzo Festa and Philip Osterholz. Also to Annie Park and Janet Qesja who share my Stockholm syndrome for MPQ. And so many others, I will not even attempt to name all of them.

- Julian Wienand and Alexander Impertro, for (hopefully) picking up this very thesis from the copy shop and handing it in for me.

- Sabrina Kupka, with whom I share the longest continuous friendship. Thank you for all the coffees and beers we shared in the last 15+ years, and especially for introducing me to Munich.

- My best friends Tobias Sick and Alina Mailach, for not forgetting our friendship even though we barely see each other. We are three experts in three different fields, but we are still the same idiots we used to be when we were teenagers.

- My parents, for giving me the freedom to do whatever I wanted to do, for supporting me both financially and morally, and for being very patient and understanding when I don't come to visit and barely have time for a phone call once in a while.

- Toni Rubio Abadal, for the years we've spent together, for the great life we have, and for the future to come. For always being there for me, supporting me even if he disagrees with my decisions. I admire his broad knowledge, his fascination, and his interest in physics, in new results and cool experiments. But I value even more our way to live, to enjoy good food, travel to places and have a vermut on the terrace.